CHAPTER 13

A Primer on Global Internal Tide and Internal Gravity Wave Continuum Modeling in HYCOM and MITgcm

Brian K. Arbic[1,2], Matthew H. Alford[3], Joseph K. Ansong[1,4], Maarten C. Buijsman[5], Robert B. Ciotti[6], J. Thomas Farrar[7], Robert W. Hallberg[8], Christopher E. Henze[6], Christopher N. Hill[9], Conrad A. Luecke[1,3], Dimitris Menemenlis[10], E. Joseph Metzger[11], Malte Müller[12], Arin D. Nelson[1], Bron C. Nelson[6], Hans E. Ngodock[11], Rui M. Ponte[13], James G. Richman[14], Anna C. Savage[1,3], Robert B. Scott[15], Jay F. Shriver[11], Harper L. Simmons[16], Innocent Souopgui[5], Patrick G. Timko[1,+], Alan J. Wallcraft[14], Luis Zamudio[14], and Zhongxiang Zhao[17]

[1]University of Michigan, Ann Arbor, Michigan, USA; [2]Currently on sabbatical at Institut des Géosciences de L'Environnement (IGE), Grenoble, France, and Laboratoire des Etudes en Géophysique et Océanographie Spatiale (LEGOS), Toulouse, France; [3]University of California San Diego, La Jolla, California, USA; [4]University of Ghana, Accra, Ghana; [5]University of Southern Mississippi, Stennis Space Center, Mississippi, USA; [6]NASA Ames Research Center, Mountain View, California, USA; [7]Woods Hole Oceanographic Institution, Woods Hole, Massachusetts, USA; [8]Geophysical Fluid Dynamics Laboratory/NOAA, Princeton, New Jersey, USA; [9]Massachusetts Institute of Technology, Cambridge, Massachusetts, USA; [10]Jet Propulsion Laboratory, California Institute of Technology, Pasadena, California, USA; [11]Naval Research Laboratory, Stennis Space Center, Mississippi,USA; [12]Norwegian Meteorological Institute, Oslo, Norway; [13]Atmospheric and Environmental Research, Lexington, Massachusetts, USA; [14]Florida State University, Tallahassee, Florida, USA; [15]Université de Bretagne Occidentale, Brest, France; [16]University of Alaska-Fairbanks, Fairbanks, Alaska, USA; [17]University of Washington, Seattle, Washington, USA; +Now at: Welsh Local Centre, Royal Meteorological Society, UK

In recent years, high-resolution ("eddying") global three-dimensional ocean general circulation models have begun to include astronomical tidal forcing alongside atmospheric forcing. Such models can carry an internal tide field with a realistic amount of nonstationarity, and an internal gravity wave continuum spectrum that compares more closely with observations as model resolution increases. Global internal tide and gravity wave models are important for understanding the three-dimensional geography of ocean mixing, for operational oceanography, and for simulating and interpreting satellite altimeter observations. Here we describe the most important technical details behind such models, including atmospheric forcing, bathymetry, astronomical tidal forcing, self-attraction and loading, quadratic bottom boundary layer drag, parameterized topographic internal wave drag, shallow-water tidal equations, and a brief summary of the theory of linear internal gravity waves. We focus on simulations run with two models, the HYbrid Coordinate Ocean Model (HYCOM) and the Massachusetts Institute of Technology general circulation model (MITgcm). We compare the modeled internal tides and internal gravity wave continuum to satellite altimeter observations, moored observational records, and the predictions of the Garrett-Munk (1975) internal gravity wave continuum spectrum. We briefly examine specific topics of interest, such as tidal energetics, internal tide nonstationarity, and the role of nonlinearities in generating the modeled internal gravity wave continuum. We also describe our first attempts at using a Kalman filter to improve the accuracy of tides embedded within a general circulation model. We discuss the challenges and opportunities of modeling stationary internal tides, non-stationary internal tides, and the internal gravity wave continuum spectrum for satellite altimetry and other applications.

Arbic, B.K., et al., 2018: A primer on global internal tide and internal gravity wave continuum modeling in HYCOM and MITgcm. In "*New Frontiers in Operational Oceanography*", E. Chassignet, A. Pascual, J. Tintoré, and J. Verron, Eds., GODAE OceanView, 307-392, doi:10.17125/gov2018.ch13.

Introduction

This book chapter is about global modeling of oceanic internal tides and the oceanic internal gravity wave continuum. The chapter focuses on hydrodynamical modeling, rather than empirical modeling, of such motions. Due to the operational oceanography theme of the book in which this chapter resides, we focus on high-spatial-resolution numerical models run over relatively short time scales—i.e., simulations that could form the dynamical backbone of operational models—rather than on lower-resolution models run over decades or centuries for climate forecasting purposes. In this introductory section, after defining internal gravity waves and internal tides, we discuss the motivation for, requirements for, and history of global modeling of internal tides and the internal gravity wave continuum. A subsequent section focuses on the technical details underlying such models, such as atmospheric forcing, bathymetry, astronomical tidal forcing, self-attraction and loading, quadratic bottom boundary layer drag, parameterized topographic internal wave drag, shallow-water tidal equations, and a brief synopsis of internal wave theory. We then show results from the first solutions, obtained with the HYbrid Coordinate Ocean Model (HYCOM; Bleck, 2002; Chassignet et al., 2009), of a high-resolution three-dimensional global ocean model with simultaneous atmospheric and tidal forcing fields. Following that, we compare results from newer simulations of HYCOM, and similar simulations of the Massachusetts Institute of Technology general circulation model (MITgcm; Marshall et al., 1997), with satellite altimeter observations, observations from moored records, and linear wave theory. We then investigate some science questions, including the impact of wave drag on the energetics and accuracy of tidal models, internal tide nonstationarity, and the role of nonlinearities in the development of the modeled internal gravity wave continuum. We describe applications of the HYCOM and MITgcm simulations to swath satellite altimetry, and ongoing attempts to improve the accuracy of tides embedded in the HYCOM simulations. After summarizing our completed work, ongoing work, and challenges for the future, we provide a dedication for the first author's contributions to the work presented here. We then describe author contributions, acknowledge our financial support and intellectual debts, and provide an appendix on the linear internal gravity wave dispersion relation.

Definition of internal gravity waves

Internal gravity waves (often abbreviated hereafter as IGWs) are "internal" to the ocean. That is, their largest vertical perturbation signals, such as the perturbations of temperature and density isolines, occur well below the ocean surface. This behavior contrasts with, for instance, the behavior of surface wind waves, for which the largest vertical perturbation signals are at the surface of the ocean[1]. Let us idealize the ocean as having n layers, where the density ρ_n of each layer increases with depth (Fig. 13.1). In this layered system, IGWs are waves that exist on the interfaces between

[1] We shall see later that the perturbation surface elevation signals of internal tides and IGWs, though small, are not zero. This is important for satellite altimetry.

layers, and for which the restoring force is gravity[2]. Because IGWs cause undulations of layer interfaces, they bring deeper (usually colder) water upwards, and shallower (usually warmer) water downwards. Therefore, IGWs bring about high-frequency fluctuations in time series of temperature taken at a fixed depth.

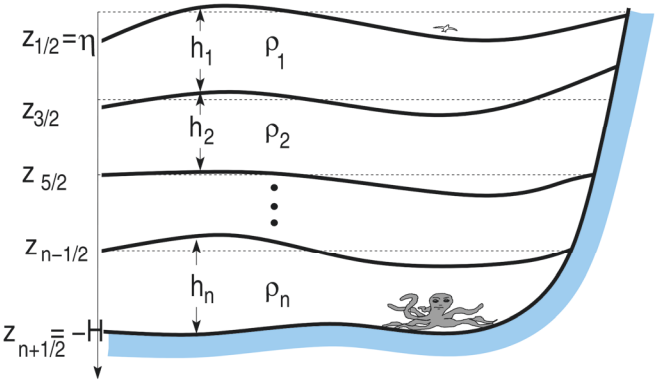

Figure 13.1. Schematic for a layered model of the ocean. There are n layers of density ρ_1, ρ_2,...ρ_n, with layer thicknesses h_1, h_2,...h_n. The sum of all layer thicknesses equals $H + \eta$, where H is the resting depth and η is the perturbation sea surface height. Internal gravity waves represent undulations of the layer interfaces from their resting positions, for which gravity is the restoring force. Reproduced from Figure 1 of Simmons et al. (2004b).

As demonstrated in the appendix, application of classical linear internal gravity wave theory shows that the frequency ω of a plane IGW obeys the inequality $|f| \leq \omega \leq N$, where f is the Coriolis frequency, also sometimes called the inertial frequency, and N is the buoyancy frequency[3]. Because IGWs are super-inertial (i.e., have frequencies exceeding the Coriolis frequency), they are not in geostrophic balance. IGWs with frequencies near the Coriolis frequency are called near-inertial waves. Near-inertial waves are primarily forced by fluctuations in surface winds (Pollard and Millard, 1970; D'Asaro, 1984; Silverthorne and Toole, 2009; Simmons and Alford, 2012). Because near-inertial waves are driven by fluctuating winds, they tend to be stronger in winter than in summer (D'Asaro, 1985). IGWs with tidal frequencies are known as internal tides, and they are generated by large-scale barotropic tidal flow over topographic features (Bell, 1975; Baines, 1982; among others). Topography will also be referred to as bathymetry throughout this chapter. The barotropic tidal flow over topographic features, including rough small-scale topography and topographic slopes along shelves, generates vertical motion, which, in a stratified fluid, implies that the interfaces between layers will oscillate vertically—i.e. that internal tides will be generated. Internal tides, also known as baroclinic tides, have smaller sea surface height signals and smaller horizontal scales than barotropic tides, large undulations at depth, and large baroclinic (vertically sheared) velocity fields. The vertical and horizontal structure of internal tides is intimately linked to the characteristics of the topographic features at which they are generated (St. Laurent and

[2] Note that there are other oceanic internal waves, for instance internal Rossby waves, for which the restoring force is not gravity.

[3] In the main text of this book chapter, we use ω to denote frequency, consistent with the notation used in our papers. In the appendix, we use σ for frequency, consistent with usage in the notes from Carl Wunsch that our appendix is based upon.

Garrett, 2002). High-vertical-mode internal tides, which have smaller horizontal scales, are generated by small-horizontal-scale topography characteristic of mid-ocean ridges, while low-vertical-mode internal tides, which have larger horizontal scales, are generated by larger horizontal-scale topographic features such as the Hawaiian Islands. High-mode IGWs are more likely to dissipate near their generation sites, while low-mode IGWs are more likely to propagate long distances, up to thousands of kilometers from their generation regions. The appendix outlines the Sturm-Liouville problem underlying the computation of vertical normal modes. At frequencies greater than tidal frequencies—hereafter often referred to as supertidal frequencies—there is a continuum of IGW energy, separate from the near-inertial and tidal peaks. This IGW continuum is described by the classical Garrett-Munk spectrum (Garrett and Munk, 1975). The Garrett-Munk spectrum is thought to arise from nonlinear interactions transferring energy out of the near-inertial and tidal frequencies and into the broadband continuum (e.g., Müller et al., 1986; Polzin, 2004).

Fig. 13.2 depicts internal wave generation mechanisms, including wind-generation of near-inertial flows, low-vertical-mode internal tide generation over larger-horizontal-scale topographic features, high-vertical-mode internal tide generation over smaller-scale rough topography, and generation of internal lee waves by low-frequency mesoscale eddy and current flows over topographic features. Fig. 13.2 also illustrates several important internal wave dissipation mechanisms, including scattering off of topographic features such as small-scale topography and continental shelf slopes, local dissipation of high-modes near their generation sites, and interactions amongst the waves themselves (wave-wave interactions) and between internal waves and mesoscale eddies and fronts. Understanding how internal tides and IGWs lose their energy is an important ongoing topic in physical oceanography. Global internal wave modeling both benefits from this conversation (in the form of improved parameterizations of internal wave damping) and contributes to it (by quantifying the long-range propagation of low-mode internal tides and hence providing some constraints on where they dissipate). As will be shown later, comparisons of global internal tide models with observations provide some clues about the locations and mechanisms of internal tide damping.

Several of the concepts described above manifest themselves in Fig. 13.3, which displays example frequency spectra[4] of temperature variance. Spectra from in-situ mooring data and three different global simulations of the MITgcm, with horizontal grid spacings of 1/12°, 1/24°, and 1/48°, are given. Diurnal and semidiurnal tidal peaks near one and two cycles per day, respectively, can be seen in the mooring and model spectra. The internal gravity wave continuum (Garrett-Munk spectrum) seen at supertidal frequencies is better resolved as the model horizontal resolution increases, a theme we will return to later in this chapter. At frequencies below tidal frequencies (subtidal frequencies), the spectra also display a broadband continuum, with no visible peaks. The low-frequency broadband spectrum is dominated by mesoscale eddies and currents. Near-inertial peaks are not prominent in temperature variance spectra, but will be seen later in spectra of kinetic energy.

[4] Technically, what is shown in this figure, and in many other figures in this chapter, is spectral density. Like many authors, we will use the shorthand terms “spectra” or “spectrum” in place of “spectral density”.

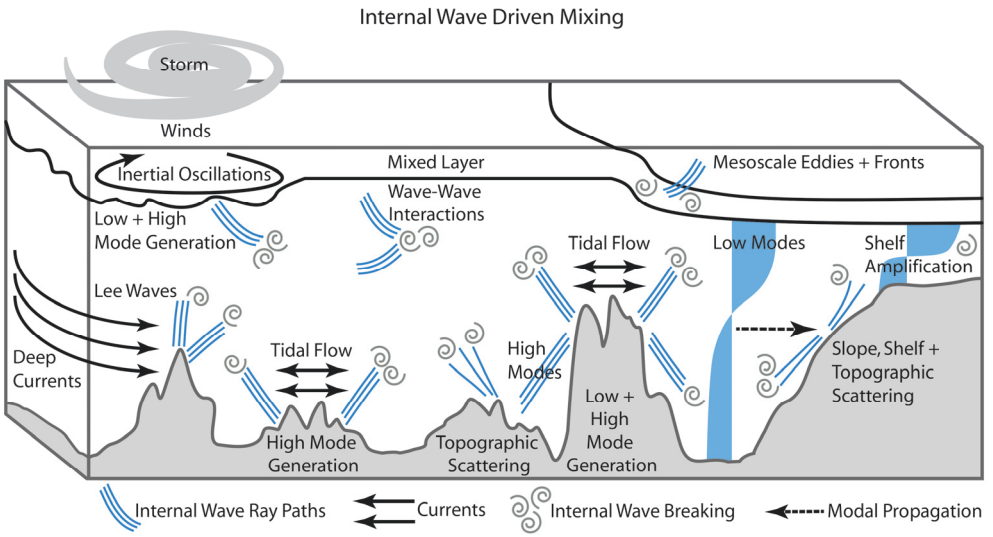

Figure 13.2. Schematic of open-ocean internal wave generation and dissipation processes that were considered as part of a Climate Process Team led by Jennifer MacKinnon of the University of California San Diego. Batroropic tidal flow interacts with topographic features to generate high-mode internal waves (e.g., at mid-ocean ridges) and low-mode internal waves (e.g., at tall steep ridges such as the Hawaiian Ridge). Deep low-frequency flows, including mesoscale eddies and currents, over topographic features can generate lee waves (e.g., in the Southern Ocean). Storms cause near-inertial oscillations in the mixed layer, which can generate both low- and high-mode internal waves (e.g., beneath storm tracks). In the open ocean these internal waves can scatter off of topographic features and potentially interact with mesoscale fronts and eddies, until they ultimately dissipate through wave-wave interactions that generate a nonlinear cascade to small-scale turbulence. Internal waves that reach the shelf and slope can scatter, dissipate via bottom boundary layer drag, or amplify as they propagate towards shallower water. Reproduced from Figure 1 of MacKinnon et al. (2017), ©American Meteorological Society, used with permission.

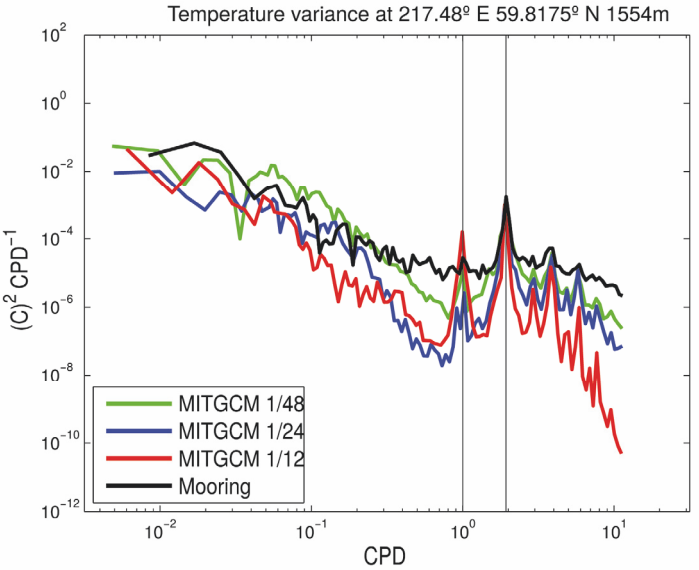

Figure 13.3. Frequency spectra of temperature variance at depth and geographical location given in plot title. Spectra are computed from observations in a historical archive (Scott et al. 2010), and from three different global simulations, with horizontal grid spacings of 1/12°, 1/24°, and 1/48°, of the MITgcm. "CPD" denotes "cycles per day." Extra vertical lines are drawn at the frequencies of M_2, the largest semidiurnal tidal line, and K_1, the largest diurnal tide.

Motivation

Why should the oceanographic community run global models of internal tides and the internal gravity wave continuum? The authors posit four important reasons.

First, global internal tide and IGW models provide important information on ocean mixing. In the ocean interior—e.g., in the open ocean, away from upper and lower boundaries—most of the diapycnal mixing[5] is due to breaking IGWs. A variety of theoretical and observational studies, including reports on observations of directly breaking IGWs (Moum et al., 2003, Klymak et al., 2008), provide support for this statement. However, the strongest evidence for the primacy of breaking IGWs in ocean interior diapycnal mixing comes from the remarkable agreement between observed dissipation rates and predictions based on IGW energy levels that assume a cascade to smaller (breaking) scales (Gregg, 1989; Polzin et al., 1995; Whalen et al., 2015; Kunze, 2017a). The breaking of IGWs is shown schematically in Fig. 13.2. It has been argued that mixing exerts an important control on the oceanic meridional overturning circulation (e.g., Munk and Wunsch, 1998; St. Laurent and Simmons, 2006; Kunze, 2017b). Indeed, the large-scale flow in ocean general circulation models is sensitive to parameterizations of tidal mixing (Simmons et al., 2004a). Global internal tide and IGW models cannot, of course, resolve IGW breaking. Nonetheless, by modeling the transport of energy by internal waves over long distances (Simmons et al., 2004b; Simmons and Alford, 2012), global internal tide and IGW models contribute importantly to the ongoing discussion of the space-time geography of internal wave breaking, a topic of great current interest in the oceanographic community, and one that is not fully settled; the fate of internal tide and IGW energy is not entirely known at present.

Second, internal tides and gravity waves are important components of any operational ocean model. IGW signals can be seen in oceanic measurements of temperature, density, and velocity. Because IGWs bring about vertical motions of water masses, they affect the speed of sound, which is a sensitive function of temperature and salinity. Modeling IGWs is therefore important for ocean acoustics. This is one reason for the enduring interest of the United States Navy in IGWs.

Third, internal tide and gravity wave modeling is of particular importance for the upcoming Surface Water Ocean Topography (SWOT) swath altimetry mission (Fu et al., 2012). Satellite altimetry has revolutionized operational oceanography, and other branches of physical oceanography, by providing accurate measurements of sea surface height (SSH) on a global scale, over decades, on repeated tracks (Fu and Cazenave, 2001). Current-generation nadir altimeters, such as the TOPEX/JASON series, provide SSH measurements along one-dimensional tracks. Examination of non-tidal phenomena—for instance El Niño, western boundary currents, and mesoscale eddies, among others—with altimeter data can only take place after the barotropic tides, which have large (of order 1000 km) horizontal scales in the open ocean, have been accurately removed. For this reason, it was recognized early on that highly accurate models of the large-scale barotropic tides were needed for successful altimeter missions.

[5] Diapyncal mixing is mixing across iospycnals, or density surfaces.

Barotropic tide models have improved greatly over the years. Cartwright and Ray (1990) proved that accurate barotropic tide models could be derived empirically from altimeter data—in their case, from GEOSAT data. The accuracy of the elevations due to the principal lunar semidiurnal tide M_2 in the Cartwright and Ray (1990) model was slightly better than the accuracy of M_2 elevations in the Schwiderski (1980) hydrodynamical one-layer (barotropic) shallow-water[6] tide model, which assimilated tide-gauge data and which served as the "go-to" tide model for more than a decade.[7] Shortly after the launch of TOPEX/POSEIDON, a number of accurate tide models were developed, including hydrodynamical barotropic shallow-water models that assimilated either altimeter or tide gauge data [e.g., the TPXO (Topex Poseidon Cross-Overs) model of Egbert et al. (1994) and Egbert and Erofeeva (2002), and the FES (Finite Element Solution) models of Le Provost et al. (1994) and Lyard et al. (2006)], and empirical models that estimated tides directly from altimeter data (e.g., Schrama and Ray, 1994; Ray, 1999). The accuracy of both empirical barotropic tide models based upon altimetry, and hydrodynamical barotropic tide models that assimilate altimeter data, was proven via comparison with independent tide-gauge data as well as other observations (Shum et al., 1997). Because many of these tide gauges were located at small islands, they were assumed to represent conditions in the open ocean, where altimetry-based tide models are more accurate. Barotropic tide models continue to improve. Stammer et al. (2014) provides a comprehensive recent overview of several state-of-the-art empirical and hydrodynamical barotropic tide models, including the new Taguchi et al. (2014) hydrodynamical model, and updated versions of the TPXO and FES models. Stammer et al. (2014) describes ongoing challenges for, and improvements in, barotropic tide models, including the need for more accurate tides in coastal and high-latitude regions, and the usage of new datasets, including tide data extracted from networks of bottom pressure sensors deployed after the 2004 Indian Ocean tsunami (Ray, 2013), to test tide models.

SWOT, which is due to launch in 2021, will measure SSH along high-resolution two-dimensional swaths, with pixel sizes of about 1 km^2. The instrument noise in SWOT is expected to be relatively low at smaller scales (wavelengths less than about 50 km). SWOT is therefore expected to allow examination of smaller-scale features than can be seen in present-generation nadir altimeter data. Because of SWOT's emphasis on smaller-scale features, internal tides and IGWs will be an important signal in SWOT, and will need to be accurately removed before smaller-scale features in low-frequency motions, such as mesoscale and submesoscale eddies, can be effectively examined. Stationary internal tides–that is, internal tides that can be described by amplitude and phase maps, as in equation (12)–have a high degree of predictability in theory, but in practice can be difficult to extract from altimeter data because of temporal sampling problems and "noise" from mesoscale eddy motions (e.g., Ray and Byrne, 2010; Shriver et al., 2012). Thus the stationary internal tides represent a significant challenge for SWOT. Some of the internal tide signal is non-stationary–that is, if one examines internal waves in the tidal band, a non-negligible fraction of the variance still remains after the stationary part has been predicted and removed. Non-stationary internal tides are

[6] The shallow-water equations will be introduced in a subsequent section.

[7] Parke and Hendershott (1980) also demonstrated that a hydrodynamical tide model could successfully assimilate tide-gauge data, but their model assimilated less data than Schwiderski's model did.

caused by internal tide interactions with the chaotic mesoscale eddy field, which has similar length and time scales as internal tides, and by temporal changes in stratification (e.g., Buijsman et al., 2017; among others). The non-stationary internal tides, and the IGW continuum, are inherently less predictable than stationary internal tides, and will therefore represent an even greater challenge for the SWOT mission. Global models of internal tides and IGWs are being used to predict the internal tide and IGW continuum SSH signals, and the impacts of internal tide and gravity wave motions on the SSH wavenumber spectrum, a critical characteristic of SWOT measurements. In some of our papers, and in other papers in the literature, the terms coherent/incoherent are used interchangeably with stationary/non-stationary. In this chapter, we will use the terms stationary/non-stationary, which many would argue are more precise, except when duplicating figures from past papers which used the coherent/incoherent terminology.

The fourth motivation for global internal tide and IGW modeling is that it is an interesting topic in and of itself. It is a new frontier in ocean modeling. Global IGW models have only existed since 2004, and evidence that global models can partially resolve the supertidal IGW continuum was only recently presented in 2015. Just as models with vigorous mesoscale eddy fields (e.g., Maltrud and McClean, 2005) have provided a new tool for understanding mesoscale eddies, global internal tide and IGW models provide a new tool for understanding higher-frequency motions. Global eddying models have developed to the point that they are used in operational forecast systems (e.g., Chassignet et al., 2009)[8]. Global internal tide and IGW models have not yet evolved to the point where they are used in forecasting systems, but that time is coming soon. It is worth noting that, just as the community has described models having resolutions of about 1/4° or better as "eddy-permitting" rather than "eddying" or "eddy-resolving", a similar distinction could be made for global internal tide and gravity wave modeling. Because the horizontal length scales of low-mode internal tides and mesoscale eddies are comparable, at least in midlatitudes, one might call, for instance, a 1/4° model with internal tides an "internal tide-permitting" model. It has been our experience that, as with mesoscale eddies, a horizontal resolution of at least 1/10° is needed for a fully vigorous low-mode internal tide field. A horizontal resolution of about 1/24° or finer is necessary for simulating a vigorous IGW continuum.

Requirements for global modeling of the internal gravity wave continuum

The classical paradigm for the generation of the IGW continuum spectrum is that winds produce near-inertial waves, barotropic tidal flow over topographic features creates internal tides, and nonlinear interactions fill out the IGW continuum. (The role of internal lee waves, generated by low-frequency flows over topography, in the IGW continuum is an interesting question). Based upon the classical paradigm, we might expect that the requirements for a resolved IGW spectrum in a model would be simultaneous atmospheric forcing and astronomical tidal forcing, together with horizontal and vertical resolution sufficiently high to allow nonlinear interactions to take place. The atmospheric forcing should contain both the low-frequency components that set up the background

[8] Following Hecht and Hasumi (2008), we will refer to models with horizontal resolutions of 1/10° or finer as "eddying," meaning that a vigorous mesoscale eddy field develops in such models.

large-scale circulation and stratification (Pedlosky, 1996), and the high-frequency components that drive near-inertial waves. Once a stratified flow is set up, the addition of astronomical tidal forcing will produce internal tides via barotropic tidal flow over topography. Because internal tide characteristics are linked to topographic scales, the resolution of small-scale bathymetric features in available global bathymetric datasets is an important topic, that we return to later.

History of global modeling of internal tides and the internal gravity wave continuum

This section is about the history of global internal tide and IGW continuum models. Some history of observations that have motivated such models is also presented. Prior to the work outlined in this chapter, global modeling of atmospherically-forced three-dimensional oceanic motions and global modeling of tides constituted separate fields of research. As computer power has increased, the frontiers of global operational modeling of the atmospherically-forced oceanic general circulation have moved toward ever higher horizontal and vertical resolution, meaning that the mesoscale eddy field has become better resolved in global and basin-scale models. Basin-scale models started to become eddying at the turn of the century (e.g., Paiva et al., 1999; Smith et al., 2000). Basin-scale models have now been run at resolutions of 1/50°-1/60° (e.g., Chassignet and Xu, 2017; Ducousso et al., 2017). Regional models are now run with grid spacings of order hundreds of meters, and have begun to resolve submesoscale eddies (e.g., Capet et al., 2008). The horizontal resolution of global tide models has also increased as a result of increasing computer power. One of the earliest global tide models, Hendershott (1972), employed a horizontal resolution of order 6° (Myrl Hendershott, personal communication, 2004). By the time of the TOPEX/POSEIDON launch, barotropic tide models were run on horizontal resolution grids of about 1° or less. As this book chapter was being written, global barotropic (one-layer) tide models are being run at horizontal resolutions of order 1/75° (Buijsman et al., paper in preparation); unstructured grids such as those used in finite-element models (Lyard et al., 2006) can go to much higher resolutions in selected areas, usually along shelves and coastlines. Along the way, larger computers were also used to run baroclinic tide models. The first baroclinic tide models run in realistic domains—e.g., not in idealized domains set up for process studies—were done on regional scales. Early regional internal tide models include Holloway (1996), who examined the Northwest Australian Shelf; Cummins and Oey (1997), who simulated the tides off of northern British Columbia; and several studies of the internal tides generated by the Hawaiian islands, for instance Kang et al. (2000) and Merrifield et al. (2001). See Carter et al. (2012) for a review of regional internal tide models, which continue to refine their resolutions with increasing computer power, and Nugroho et al. (2017), for an example of a recent regional internal tide modeling study. Nugroho et al. (2017) showed that inclusion of tides in a regional three-dimensional model of the Indonesian Seas yielded realistic levels of tidal dissipation, which in turn exerted important controls on water mass properties.

Both regional and global internal tide models have been motivated by evidence for stationary low-mode internal tides radiating over long distances in acoustic tomography data (Dushaw et al., 1995) and in altimeter data (Ray and Mitchum, 1996, 1997). Fig. 13.4, taken from Ray and Mitchum

(1996), displays M_2 tidal amplitudes estimated along a TOPEX/POSEIDON track (ragged curve), on top of M_2 amplitudes estimated from a barotropic tidal model along the same track (solid curve). As shown in the figure, the SSH signature of barotropic tides has much larger horizontal scales than the SSH signature of internal tides. Associated with the different length scales, the phase speeds also differ. The phase speed of barotropic tides in the open ocean is about 200 m s^{-1} while the open-ocean phase speed of vertical mode-1 internal tides is typically about 2 m s^{-1}. The higher-wavenumber "wiggles" in the ragged curve represent the M_2 internal tide signal. This altimeter evidence of stationary internal tides propagating over long distances, along with the tomography evidence, implies that tidal energy can be transported over long distances before dissipating, with profound implications for the three-dimensional geography of oceanic mixing.

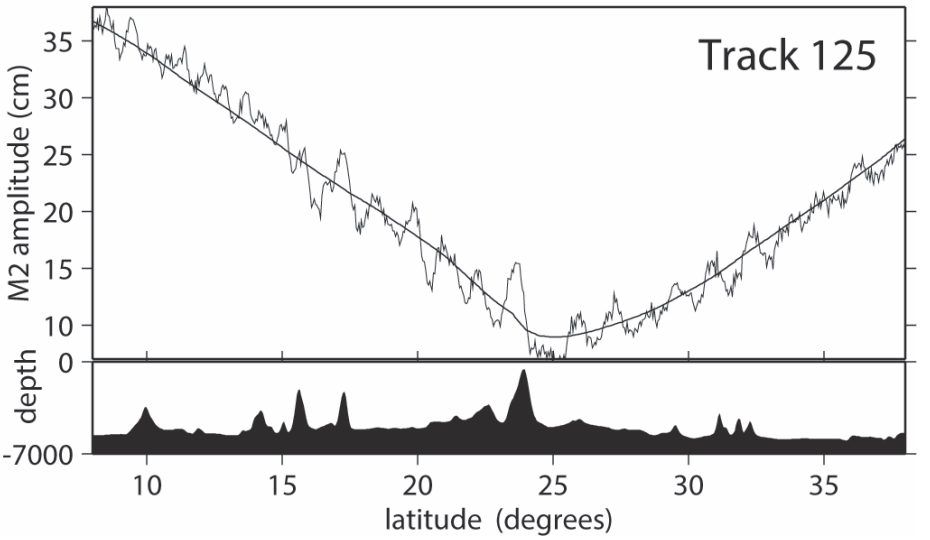

Figure 13.4. Ragged curve: M_2 tidal amplitudes along Topex/Poseidon track number 125. Smooth curve: M_2 tidal amplitudes estimated from a barotropic tide model. Bathymetry is shown in black. Reproduced from Figure 1 of Ray and Mitchum (1996), ©American Geophysical Union, Wiley Online Library, used with permission.

Further motivation for internal tide models arises from evidence that internal tide production over open-ocean topographic features accounts for about 25-30% of the energy lost in the global barotropic tidal energy budget. Egbert and Ray (2000, 2001, 2003) showed that about 1 TW of the total 3.5 TW barotropic tidal dissipation takes place in the open ocean, through generation of internal tides by barotropic flow over topography. Egbert and Ray's results implicate internal tide dissipation as an important contributor to the mixing that underpins the large-scale circulation (Munk and Wunsch, 1998; St. Laurent and Simmons, 2006; Kunze, 2017b). Fig. 13.5a displays energy lost from the barotropic tide, as inferred from an updated version of the TPXO model. The TPXO results display substantial energy dissipation over topographic features, such as the mid-Atlantic Ridge and the Hawaiian islands. The increased internal wave activity over open-ocean topographic features can also be seen in Fig. 13.5b, which displays the conversion of energy from barotropic tides to internal tides in simulations of the HYbrid Coordinate Ocean Model (HYCOM) computed by Buijsman et al. (2016). Further, enhanced dissipation of oceanic flows over

topographic features has been seen in field campaigns, such as the Brazil Basin Tracer Release Experiment (BBTRE; e.g., Polzin et al., 1997; Fig. 13.6), the Diapycnal and Isopycnal Mixing Experiment in the Southern Ocean (DIMES; e.g., Gille et al., 2007; St. Laurent et al., 2012), and others, that include microstructure dissipation measurements. See MacKinnon et al. (2017), Waterhouse et al. (2014), and Whalen et al. (2012, 2015) for comprehensive discussions of observations indicating enhanced oceanic energy dissipation over rough topographic features. Along the shelves, considerable barotropic tidal dissipation takes place in regions with large coastal tides, such as the Hudson Strait, the Northwest European Shelf, the Bay of Fundy, and others. Collectively, the shelves dissipate about 70-75% of the tidal energy. For much of the 20th century, the shelves were thought to account for almost all of the tidal dissipation. The Egbert and Ray (2000, 2001, 2003) sequence of papers, and related work done by others, have brought about a paradigm shift in this important topic.

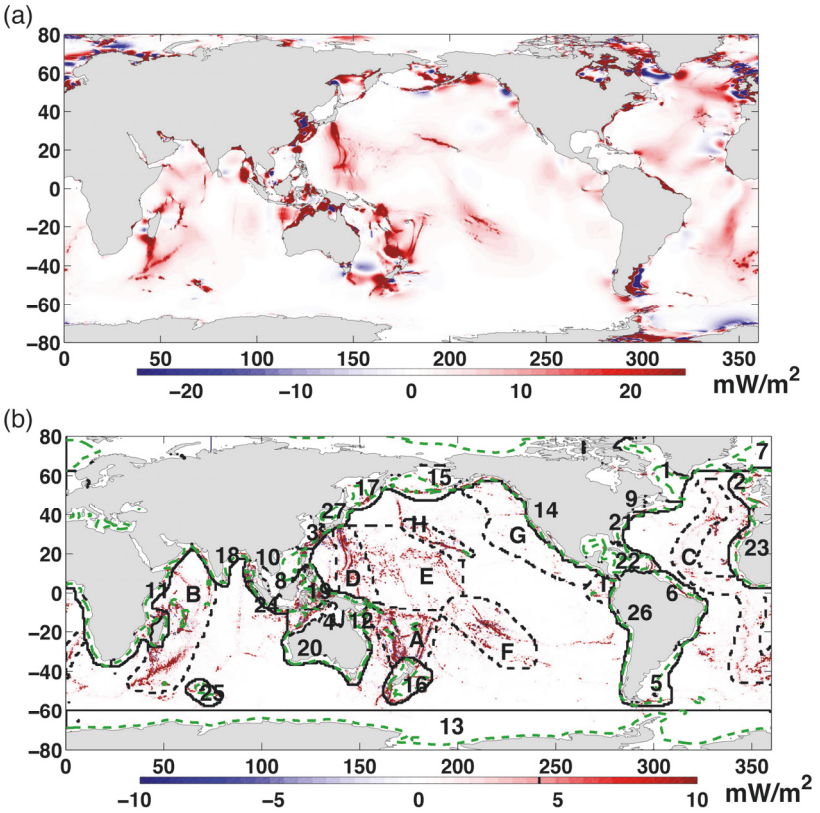

Figure 13.5. (a) Rate of energy lost from the M_2 barotropic tide (mW/m^2), estimated from TPXO8 global assimilation solution. (b) Baroclinic conversion rate (mW/m^2) for all semidiurnal constituents, computed from the HYCOM 18.5 solution (nominal resolution 1/12.5°; Buijsman et al., 2016). The conversion rate shown in (b) has been smoothed, and the plotting range has been reduced relative to that in panel [a], in order to enhance visibility of global scale patterns. Shallow and deep ocean areas used for localized dissipation and conversion calculations are defined by solid lines for shallow areas (numbered 1–27) and dashed lines for deep ocean areas (labeled A–I). The green dashed line is the more formally defined boundary between deep and shallow areas, as discussed in Ray and Egbert (2001). Reproduced from Figure 13.8 of Ray and Egbert (2017), which can be consulted for further details. Republished with permission of Taylor and Francis Group, conveyed through the Copyright Clearance Center.

The first basin-scale simulation of internal tides was performed by Niwa and Hibiya (2001). The first global internal tide simulations were performed in the companion papers Arbic et al. (2004) and Simmons et al. (2004b). These early global internal tide simulations were idealized in several respects. Atmospheric forcing was not included—the only forcing present was the astronomical tidal potential. Because the atmospheric forcing, which sets up the oceanic stratification, was lacking, the stratification profile was set to be horizontally uniform. The stratification profile was taken from observations in the subtropics, and was therefore not representative of equatorial or polar conditions. Figs. 13.7-13.9 display the interfacial height perturbations at three different times during the spin-up phase of the main two-layer simulation analyzed in Simmons et al. (2004b). The simplicity of this simulation allows for a nice illustration of the spin-up, but the exact values of the interfacial heights should not be taken too literally due to the unrealistic horizontally constant stratification. Internal wave generation at mid-ocean topographic features such as the Hawaiian and French Polynesian Islands is readily apparent. Tidal forcing is not required for global modeling of near-inertial waves, which are forced by rapid fluctuations in the wind fields. Examination of near-inertial waves in global models has been done by Furiuchi et al. (2008) and Simmons and Alford (2012). As with low-mode internal tides, low-mode near-inertial waves can carry energy over thousands of kilometers as they propagate (Alford, 2003).

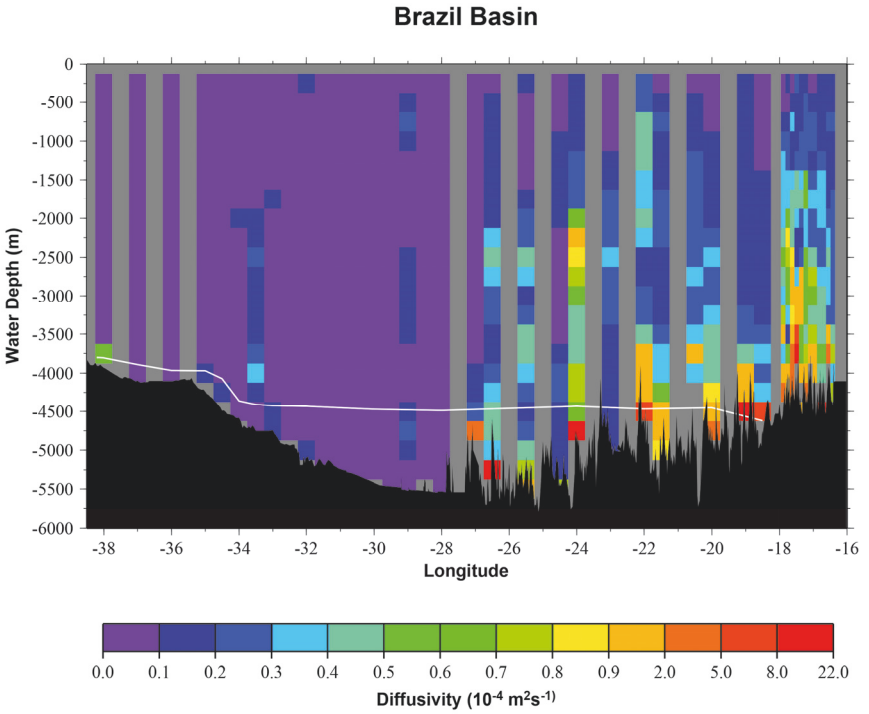

Figure 13.6. Depth-longitude section of cross-isopycnal (diapycnal) diffusivity in the Brazil Basin inferred from velocity micostructure observations. Note the nonuniform color scale. Microstructure data from two quasi-zonal transects have been combined without regard to latitude. Underway bathymetric data to 32°W is from an eastward track, and the balance comes from a westward track. The white line marks the depth of the 0.8°C interface. Reproduced from Figure 2 of Polzin et al. (1997). Reprinted with permission from AAAS. Except as provided by law, this material may not be further reproduced, distributed, transmitted, modified, adapted, performed, displayed, published, or sold in whole or in part, without prior written permission from the publisher.

In coastal modeling, and in global barotropic modeling, it has long been common to simultaneously resolve tides and atmospherically-driven motions. The earliest attempts to simultaneously include atmospheric and tidal forcing in three-dimensional global models (Thomas et al., 2001; Schiller and Fiedler, 2007; Müller et al., 2010) were done in simulations with horizontal resolutions of order 1°, in which neither mesoscale eddies nor internal tides are resolved; nonetheless, some interesting impacts of barotropic tides on the oceanic general circulation were found. The first global, three-dimensional, high-resolution simulation done with simultaneous atmospheric and tidal forcing was done using HYCOM and is described in Arbic et al. (2010). For a shorter and less technical overview of these HYCOM simulations, see Arbic et al. (2012a). Because of the high resolution, these HYCOM simulations resolved mesoscale eddies, western boundary currents, and internal tides, as well as the larger-scale barotropic tides. We will report on this HYCOM simulation as well as updated HYCOM simulations later. For now, we note that a small but growing number of "wind plus tides" simulations have been done in global three-dimensional high-resolution (1/10° or finer) models, for instance the German STORMTIDE model (e.g., Müller et al., 2012), the GFDL Generalized Ocean Layered Model (GOLD; e.g., Waterhouse et al., 2014), and the Massachusetts Institute of Technology general circulation model (MITgcm; e.g., Rocha et al., 2016a, 2016b). The lead author is collaborating with two modeling groups in France that are preparing to perform basin-scale and global high-resolution ("eddying") simulations with simultaneous atmospheric and tidal forcing. It is clear that concurrent atmospheric and tidal forcing will become increasingly common in global eddying ocean model runs of the future.

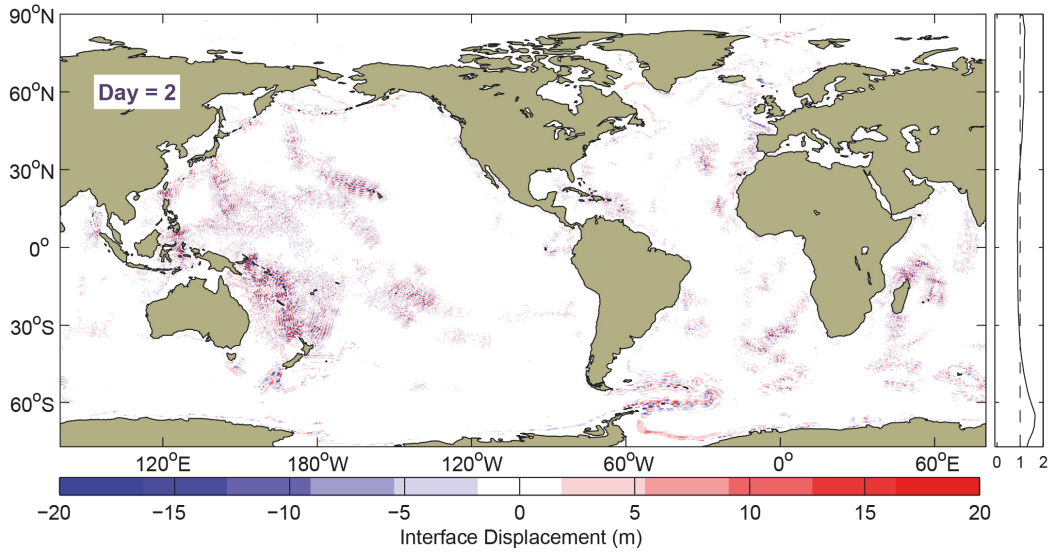

Figure 13.7. Interface displacement normalized according to Eq. (15) of Simmons et al. (2004b), on day 2 of spin-up of a two-layer M_2 simulation with simplified, horizontally uniform stratification. The resting depth of the interface is at 1100 m. The zonal mean of the normalization factor is shown on the right side of the plot. Reproduced from Figure 6 of Simmons et al. (2004b).

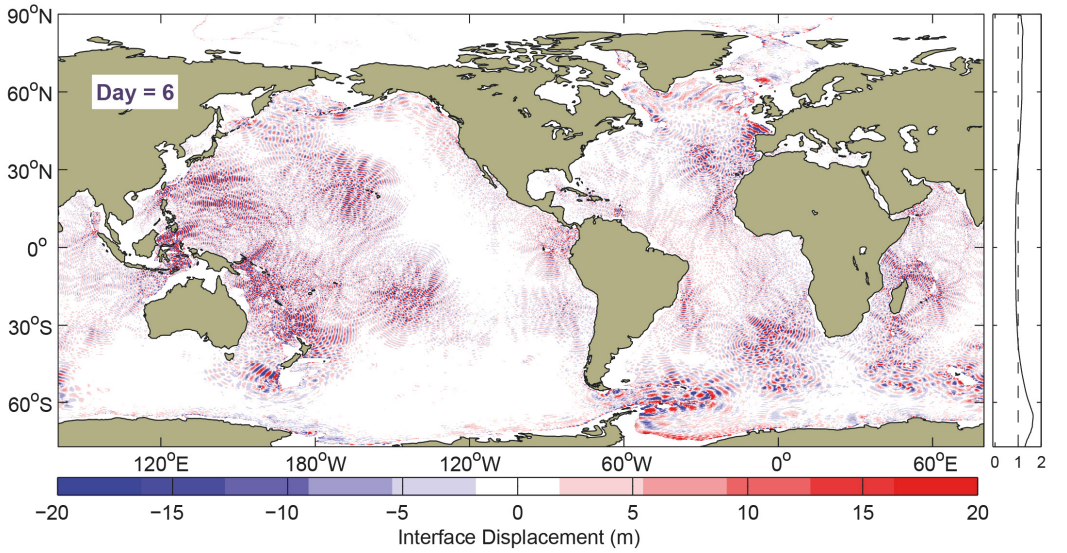

Figure 13.8. As in Fig. 13.7 but for day 6 of spin-up. Reproduced from Figure 7 of Simmons et al. (2004b).

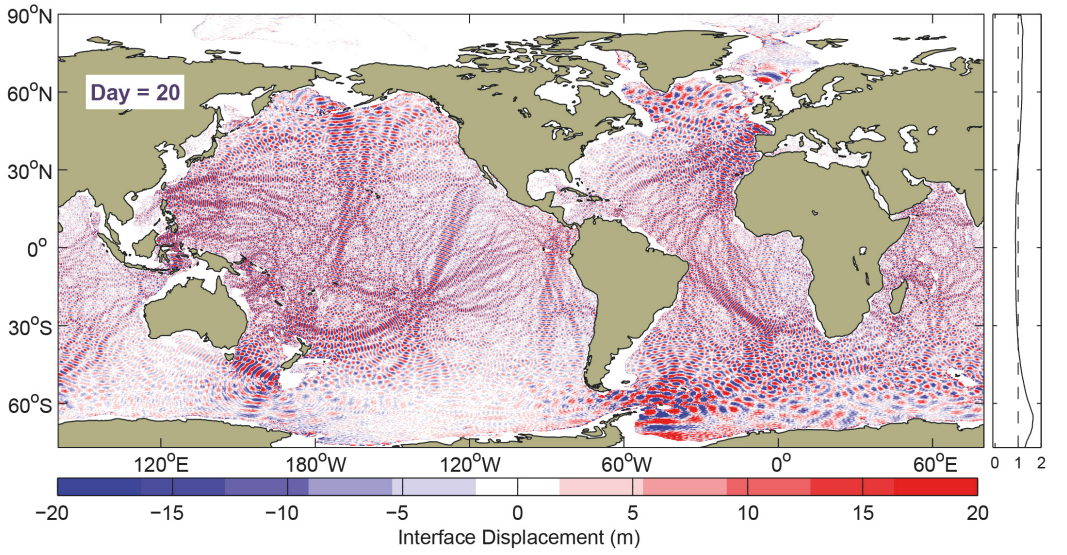

Figure 13.9. As in Fig. 13.7 but for day 20 of spin-up. Reproduced from Figure 8 of Simmons et al. (2004b).

It took some time to recognize the existence of a quasi-realistic IGW continuum spectrum in high-resolution models with concurrent tidal and atmospheric forcing. The first demonstration of a partial IGW continuum in global models, using HYCOM, was done in Müller et al. (2015). The realism of the HYCOM IGW kinetic energy spectra analyzed in Müller et al. (2015) increased as the horizontal grid spacing decreased from 1/12.5° to 1/25°. Rocha et al. (2016a, 2016b) subsequently showed that MITgcm simulations also carry a partial IGW continuum. Savage et al. (2017a, 2017b) examined the IGW SSH fields and spectra in 1/12.5° and 1/25° simulations of HYCOM and in 1/12°, 1/24°, and 1/48° simulations of the MITgcm. The HYCOM and MITgcm simulations are being used extensively in preparation for the SWOT mission.

This book chapter focuses on global internal tide and wave modeling done with HYCOM and the MITgcm. HYCOM and MITgcm are full ocean general circulation models, with multiple layers, that include parameterizations for mixed-layer physics and other processes. They have been used as ocean general circulation models in many applications. Here we focus on high-resolution, three-dimensional simulations of these two models with simultaneous atmospheric and tidal forcing. The HYCOM "wind plus tides" simulations have existed longer than the MITgcm "wind plus tides" simulations, are associated with a longer publication list, have been compared with observations more frequently, and include a parameterized topographic internal wave drag, which is not included in the MITgcm simulations, or in the "wind plus tides" simulations performed thus far by other modeling groups. The parameterized wave drag (e.g., Garner, 2005) is meant to account for the breaking of internal waves throughout the water column, and for low-level turbulence, that are left unresolved in today's global models, even models run at the highest resolutions possible on current-generation supercomputers.

Because of the long history of the HYCOM simulations, they have gone through several iterations. The first HYCOM "wind plus tides" simulations used in Arbic et al. (2010) had some numerical problems (see the large spurious signals in bottom kinetic energy in the Gulf of Mexico, for example, in Figure 2b of that paper). These numerical problems were greatly reduced in the runs used in subsequent papers. Up until Ansong et al. (2015), the HYCOM simulations discussed in this chapter had 32 hybrid layers in the vertical direction; since Ansong et al. (2015) they have had 41. Ngodock et al. (2016) introduced a Kalman filter method to improve the accuracy of the modeled barotropic tides. All of the HYCOM simulations since then have employed the Kalman filter, which will be discussed in a subsequent section. The topographic drag scheme, and the scheme for self-attraction and loading, have also changed over time. Finally, we note that none of the HYCOM "wind plus tides" simulations used in our publications to date employ data assimilation acting on the mesoscale eddy field, although such runs are already being performed and will become more prevalent in the near future. The MITgcm "wind plus tides" simulations have not been around as long as the HYCOM "wind plus tides" simulations, and have not been vetted as extensively. One very significant advantage of the MITgcm simulations, however, is that they have been run with higher horizontal resolution, up to 1/48°, and with higher vertical resolution (90 z-levels, as opposed to 41 hybrid layers in HYCOM)[9]. The HYCOM simulations are run with horizontal grid spacings of 1/12.5° and 1/25° and are often referred to as HYCOM12 and HYCOM25 throughout this chapter. The MITgcm simulations are run with horizontal grid spacings of 1/12°, 1/24°, and 1/48° and are often referred to as MITgcm12, MITgcm24, and MITgcm48, respectively, throughout this chapter. The fact that a qualitatively similar IGW spectrum emerges in two different models, which

[9] Different modeling systems make use of different vertical coordinates. Some of the most common choices are z-level coordinates, which are employed in MITgcm, terrain-following coordinates, isopycnal (density-based) coordinates, and hybrid vertical coordinates. Hybrid coordinates, which can smoothly transition between the choices above, are used in HYCOM. Griffies et al. (2000) and Griffies (2005) can be consulted for detailed discussions of vertical coordinate choices in ocean models. Bleck (2002) describes the hybrid vertical coordinate approach used in HYCOM.

differ from each other in various respects including in their vertical coordinate systems, gives us more confidence in the results presented here.

Technical Details

This section describes some of the technical details involved in global internal gravity wave modeling, including atmospheric forcing, bathymetry, astronomical tidal forcing, self-attraction and loading, quadratic bottom boundary layer drag and parameterized topographic internal wave drag, and the shallow-water tidal equations. The section concludes with a brief synopsis of the Garrett and Munk (1975) description of the IGW continuum spectrum, and of linear dispersion relations for IGWs, both of which will be used to interpret our model results.

Atmospheric forcing

Atmospheric forcing of the ocean includes wind stress, evaporation minus precipitation (which impacts salinity at the ocean surface), and air-sea heat fluxes (which impact, and feed off of, sea surface temperature)—see Csanady (2001), Josey et al. (2013), and references therein for an overview. To obtain a realistically energetic near-inertial wave field, a model should be forced by winds that update frequently (e.g., about three hours or less). A component of atmospheric forcing that is often neglected in oceanic general circulation models is atmospheric pressure loading. There is a rich literature on oceanic motions forced by pressure loading (e.g., Ponte, 1994; Tierney et al., 2000a; Stammer et al., 2000; Carrère and Lyard, 2003). Because atmospheric pressure is broadband, it elicits a broadband response in the ocean. A special case, worth a brief mention here, is the atmospheric tide, which is thermally driven (Chapman and Lindzen, 1970). The predominant periods of the atmospheric thermal tide are 24 and 12 hours. The pressure loading of the 24-hour S_1 atmospheric tide is the predominant driver of the small S_1 tide in the ocean (Ray and Egbert, 2004). The pressure loading of the 12-hour S_2 atmospheric tide is an order 15% correction (e.g., Arbic, 2005) to the oceanic S_2 tide, which is primarily forced by the Sun's gravity and is the second largest tide in the ocean.

The atmospheric forcing for the HYCOM simulations presented here has evolved over time. The most recent HYCOM simulations include pressure loading as well as atmospheric buoyancy and wind forcing. The most recent HYCOM simulations are forced by the United States Navy atmospheric model, NAVGEM (Hogan et al., 2014), which recently replaced the NOGAPS model (Rosmond et al., 2002). The frequency of NAVGEM output has varied over time. Some of our recent HYCOM simulations have been forced by atmospheric fields updated every three hours, and some by atmospheric fields updated every hour. As noted, high-frequency atmospheric forcing is needed to represent the S_2 atmospheric tide (e.g., Ray and Ponte, 2003), to simulate the associated oceanic response (e.g., Arbic, 2005), and to simulate oceanic near-inertial waves. Our papers on the HYCOM tidal simulations, for instance Arbic et al. (2010), Shriver et al. (2012), and Savage et al. (2017b), can be consulted for more details on the atmospheric forcing fields, and their evolution over time.

The MITgcm simulations described here were forced by six-hourly atmospheric fields from the 0.14° European Center for Medium Range Weather Forecasts (ECMWF) operational atmospheric reanalysis. The ECMWF fields are converted to surface fluxes using the Large and Yeager (2004) versions of the bulk formulae. The MITgcm simulations are also forced by pressure loading in addition to atmospheric wind and buoyancy forcing.

Bathymetry

Bathymetry is a crucial consideration in global internal tide and IGW continuum models, because internal tides are generated by barotropic tidal flow over topographic features. Most global models use a version of the Smith and Sandwell (1997) bathymetry, which has been continually updated over time. The bathymetric database uses high-quality acoustic soundings where they are available. However, because of the military significance of acoustic sounding data in coastal waters, local governments often do not release them. In the open ocean, sounding data is rare; perhaps 10% of the ocean floor has been mapped acoustically (Wessel and Chandler, 2011), and most of the regions so mapped are in coastal shelf regions (Charette and Smith, 2010). Thus, in the open-ocean, Smith and Sandwell (1997) employ satellite altimetry data. The sea surface height signal is sensitive to local mass anomalies. The technique can resolve features down to about π times the ocean depth, in other words, about 10-20 km in the open-ocean. The altimeter inversion technique works poorly in shelf areas. In order to prevent numerical problems in ocean models, bathymetry must be smoothed to remove features with length scales less than the grid spacings employed in the models.

Bathymetry is, of course, a crucial control for other oceanic motions as well as for internal tides and IGWs. For example, deep-water masses often enter the ocean through bathymetric sills (Price and Baringer, 1994), and the paths of mesoscale eddies are steered by topography (LaCasce, 2000; Scott et al., 2008; Stewart et al., 2015). Bathymetry is also of primary importance for accurate barotropic tide modeling (Florent Lyard, personal communications over many years).

Astronomical tidal forcing

Tidal research has a long history, and it includes some of the greatest names in physics and geophysics, such as Isaac Newton, Pierre-Simon Laplace, George Biddell Airy, Lord Kelvin, and George Darwin. Cartwright (1999) and Pugh (1987) can be consulted for some of this fascinating history. Here we outline some of the fundamentals underlying astronomical tidal forcing, for those readers who might not have encountered them before.

The astronomical tidal potential is due to the differential gravitational forcing of a distant object across a body of finite size. Thus, for instance, the gravitational pull of the Moon is greater at points on the Earth facing the Moon than it is at the center of the Earth, and greater at the Earth's center than at points facing away from the Moon (Fig. 13.10). Due to the mutual gravitational attraction between the Earth and Moon, all points on Earth trace circles with a radius equal to the distance between the Earth's center and the center of mass of the Earth-Moon system. Therefore, all points on Earth experience a centripetal force equal to

$$F_{centripetal} = \frac{GM_{moon}}{r^2}, \tag{1}$$

where G is Newton's gravitational constant, M_{moon} is the mass of the Moon, and r is the distance between the center of the Moon and the center of the Earth. On the side of the Earth closest to the Moon, the gravitational pull of the Moon is given by

$$F_{gravitational} = \frac{GM_{moon}}{(r-a)^2}, \tag{2}$$

where a is the radius of the Earth. The tidal force is given by the difference of these forces,

$$F_{tidal} = F_{gravitational} - F_{centripetal} = GM_{moon}\left[\frac{1}{(r-a)^2} - \frac{1}{r^2}\right] \approx \frac{GM_{moon}}{r^2}\left[\frac{1}{1-\frac{2a}{r}} - 1\right] \approx \frac{2aGM_{moon}}{r^3}, \tag{3}$$

where we have used the fact that $a \ll r$. On the side of the Earth farthest from the Moon, we have

$$F_{tidal} = F_{gravitational} - F_{centripetal} = GM_{moon}\left[\frac{1}{(r+a)^2} - \frac{1}{r^2}\right] \approx \frac{GM_{moon}}{r^2}\left[\frac{1}{1+\frac{2a}{r}} - 1\right] \approx -\frac{2aGM_{moon}}{r^3}. \tag{4}$$

Thus to first order the tidal forces on the side of the Earth facing the Moon and the side farthest from the Moon are equal but opposite, yielding tidal bulges pointing outwards from the Earth in both cases. Note that the tidal force is proportional to Earth's radius a; hence, as anticipated, the finite size of Earth is a critical factor in tidal forcing. Because the gravitational force is proportional to $\frac{1}{r^2}$, the tidal force, being a difference and hence involving a derivative, is proportional to $\frac{1}{r^3}$.

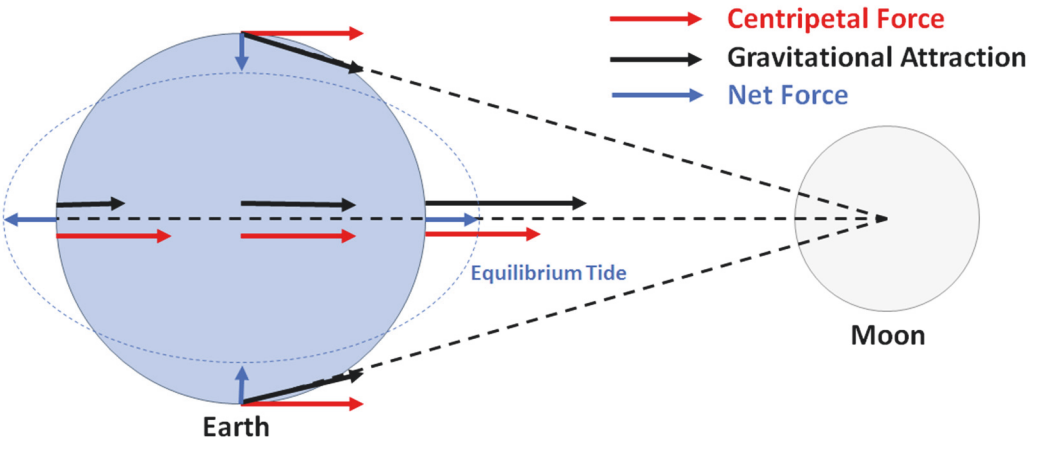

Figure 13.10. Tide-producing forces.

The same reasoning applies to the Sun's gravity. The Sun is 27,000,000 times more massive than the Moon, but it is 390 times farther away. This equates to the solar tidal force being 46% of the lunar tidal force; an important but smaller contribution.

Because the tidal forcing consists of two bulges, under which the Earth rotates, the period of the principal lunar semidiurnal tide is equal to half of a lunar day—the latter representing the time it takes for an observer on Earth to see the same point on the Moon two consecutive times as the Earth orbits. A lunar day is 24.84 hours, and the period of the principal lunar semidiurnal tide (M_2) is therefore 12.42 hours. Because a solar day—a day measured against the Sun—is 24 hours, the period of the principal solar semidiurnal tide (S_2) is 12 hours. The close but unequal frequencies of M_2 and S_2 yield a classic "beat" pattern in the tides. The tidal range, or difference between high and low tide, is especially large during spring tide, when the Earth, Moon, and Sun are aligned, and is especially small during neap tide, when the line between the Earth and Moon is at right angles to the line between the Earth and Sun. The tidal forcing is often referred to as the "equilibrium tide", a concept that is credited to Newton (Newton, 1687; Cartwright, 1999). Another commonly used term for tidal forcing is "astronomical tidal potential".

Tidal forcing is not just at semidiurnal frequencies. Because the Moon's orbit around the Earth is not in the Earth's equatorial plane, an observer on Earth sees two high tidal forcing peaks that are unequal during the course of a day (Fig. 13.11). As shown in the figure, a northern hemisphere observer sees a higher high tidal forcing at time B and a lower high tidal forcing at time A. At the same longitude, a southern hemisphere observer sees a lower high tide when the northern hemisphere observer sees a higher high tide and vice versa. This diurnal inequality yields an effective tidal forcing at periods close to once per day; in other words, diurnal tides. There are also diurnal tides that are caused by the Sun's gravity field.

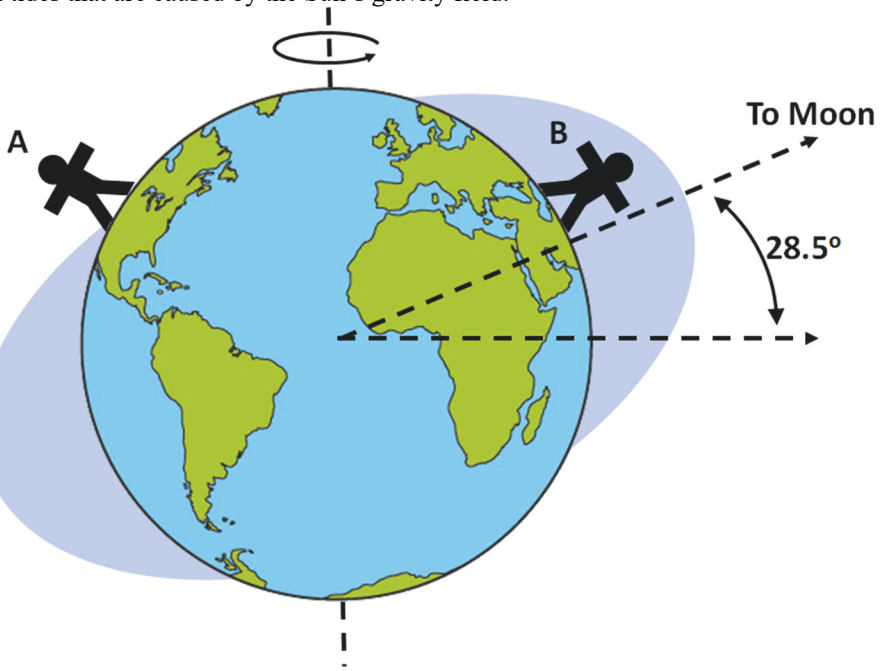

Figure 13.11. Declination and diurnal tides.

While the discussion of the astronomical tidal forcing given above is intuitive, a more complete treatment of the tidal forcing is done in terms of spherical harmonic expansions of the gravitational potential, where the potential is computed from a highly accurate trigonometric series expansion for the orbital positions of the Sun and Moon (Doodson, 1921; Cartwright and Tayler, 1971). This fuller treatment yields a multitude of terms having varying frequencies and amplitudes. The frequencies represent multiples, sums, and differences of the fundamental frequencies in the Earth-Moon-Sun system. The frequencies cluster around semidiurnal, diurnal, and longer periods, and the three types of tides correspond to the degree-two spherical harmonics.[10] These clusters are often referred to as "tidal species", a concept credited to Laplace (Cartwright, 1999). Cartwright and Tayler (1971)'s analysis netted approximately 400 terms. More recent treatments, e.g., Roosbeek (1996), have many thousands of terms. Most ocean tide studies include only some of these terms. See Williams and Boggs (2017) for a comprehensive treatment of the relationship between the dissipations of tidal constituents[11] and the secular changes in Earth's rotation, the semimajor axis of the Earth-Moon orbit, and other characteristics of the Earth-Moon system.

For a semidiurnal tidal constituent, the equilibrium tide, denoted by η_{EQ} below, is given by

$$\eta_{EQ} = Af(t_{ref})(1 + k_2 - h_2)\cos^2(\phi)\cos[\omega(t - t_{ref}) + \chi(t_{ref}) + \nu(t_{ref}) + 2\lambda], \quad (5)$$

where A and ω are constituent-dependent forcing amplitudes and frequencies, φ is latitude, λ is longitude, t is time, t_{ref} is a reference time (which could represent, for instance, the starting time of a particular model run), and $\chi(t_{ref})$ is the constituent-dependent astronomical argument referenced to t_{ref} (e.g., Schwiderski, 1980; Pugh, 1987). The Love numbers h_2 and k_2, which are frequency-dependent especially in the diurnal band (Wahr and Sasao, 1981), respectively account for the deformation of the solid earth resulting from the astronomical forcing, and the resulting alteration in the gravitational potential due to the redistributed mass within the solid Earth. The solid-earth deformations arising in response to the astronomical forcing are known as the "body tide". Solid-earth body-tide oscillations can reach several cm in amplitude, but they are not noticeable in common experience because of their long (planetary-scale) wavelengths. The nodal factors $f(t_{ref})$ and $\upsilon(t_{ref})$ respectively account for the slow modulation of amplitude and phase of a tidal constituent due to low-frequency changes in the Earth-Moon-Sun system (especially the 18.6 year nodal cycle—see Pugh, 1987). The inclusion of nodal factors depends on the application. Many tidal studies do not need to use them. On the other hand, accurate tidal prediction, and accurate analysis of ocean observations, requires either the use of nodal factors or the use of a large number of tidal lines over a record duration long enough (~ 19 years) to resolve the multitude of lines present in the actual tidal potential. For a diurnal tidal constituent, the equilibrium tide is given by

$$\eta_{EQ} = Af(t_{ref})(1 + k_2 - h_2)\sin(2\phi)\cos[\omega(t - t_{ref}) + \chi(t_{ref}) + \nu(t_{ref}) + \lambda], \quad (6)$$

[10] The astronomical tidal potential also includes degree-three and higher spherical harmonics. The higher-order harmonics are small and are neglected in many ocean tide models. See Cartwright (1975) for a demonstration that degree-three tides can be detected in observational records.

[11] As is explained in Egbert and Ray (2017), a "constituent" is a cluster of spectral lines, not a single isolated line. This point is often discussed loosely in the literature, including in some of our previous papers.

and for a long-period constituent, the equilibrium tide is given by

$$\eta_{EQ} = Af(t_{ref})(1 + k_2 - h_2)\left[\frac{1}{2} - \frac{3}{2}\sin^2(\phi)\right]\cos[\omega(t - t_{ref}) + \chi(t_{ref}) + \nu(t_{ref})]. \quad (7)$$

The diurnal tidal forcing is antisymmetric around the equator, consistent with the intuition developed from Fig. 13.11. The long-period constituents have relatively small amplitudes and will not be much discussed in this book chapter. To model many constituents, one must simply add the appropriate extra term to η_{EQ} each time a constituent is included.

Constituent	ω (10^{-4} s^{-1})	A (cm)	$1 + k_2 - h_2$	Period (solar days)
M_m	0.026392	2.2191	0.693	27.5546
M_f	0.053234	4.2041	0.693	13.6608
Q_1	0.6495854	1.9273	0.695	1.1195
O_1	0.6759774	10.0661	0.695	1.0758
P_1	0.7252295	4.6848	0.706	1.0027
K_1	0.7292117	14.1565	0.736	0.9973
N_2	1.378797	4.6397	0.693	0.5274
M_2	1.405189	24.2334	0.693	0.5175
S_2	1.454441	11.2743	0.693	0.5000
K_2	1.458423	3.0684	0.693	0.4986

Table 13.1. Constituent-dependent frequencies ω, astronomical forcing amplitudes A, and Love number combinations $1 + k_2 - h_2$ used to compute equilibrium tide η_{EQ}. The periods $2\pi/\omega$ are also given. Reproduced from Table 1 of Arbic et al. (2004).

Table 13.1 provides the frequencies, periods, amplitudes, and Love number combination $1 + k_2 - h_2$ for the four largest semidiurnal constituents, four largest diurnal constituents, and two largest long-period constituents. Note that the Love number combination is about 0.7, meaning that the body tide acts to reduce the amplitude of the equilibrium ocean tide forcing by 30%—a significant impact for an effect that sounds quite exotic when one first learns of it! Pugh (1987) and other sources can be consulted for computation of the astronomical arguments x and nodal factors. As an alternative to modeling multiple tidal constituents using sums of the appropriate η_{EQ} terms, one could instead employ the full luni-solar tidal potential, as in Weis et al. (2008). In this approach,

one would not include nodal factors, because one would instead be effectively modeling all tidal forcing frequencies. Employing the full luni-solar potential in its purest form would not allow for the frequency dependence of the body-tide Love numbers. To create such an accounting would require a harmonic analysis of the full potential, which would effectively mean writing the potential as a sum of many η_{EQ} terms, as in the more traditional approach outlined above.

Early HYCOM tides simulations (Arbic et al., 2010, 2012a; Shriver et al., 2012) included the four largest diurnal tidal constituents (K_1, O_1, P_1, and Q_1) and the four largest semidiurnal tidal constituents (M_2, S_2, N_2, and K_2). However, later simulations of HYCOM have included only the five largest tidal constituents— M_2, S_2, N_2, K_1, and O_1—due to the difficulties in separating the nearby $S_2 - K_2$ and $K_1 - P_1$ frequency pairs in relatively short model outputs. Savage et al. (2017b) can be consulted for a detailed description of the MITgcm simulations. Due to a misunderstanding amongst several co-authors, Savage et al. (2017b) incorrectly stated that the MITgcm tidal forcing included sixteen tidal constituents–eight long period tides, the four largest diurnal constituents, and the four largest semidiurnal constituents. In fact, the MITgcm simulations employed the full luni-solar tidal potential.

Self-attraction and loading

This section describes self-attraction and loading, an effect that those who are new to tidal research often find even more surprising than solid-earth body tides. In addition to its direct body-tide response to the astronomical tidal potential, the solid earth also compresses and expands due to the load of the ocean tide. Furthermore, the self-gravitation of both the ocean tide itself, and the load-deformed solid earth, alters the gravitational potential. Collectively, these effects are known as the self-attraction and loading (SAL) term (Hendershott, 1972; Ray, 1998). The η_{SAL} term is often computed in terms of a spherical harmonic expansion,

$$\eta_{SAL} = \sum_n \frac{3\rho_0}{\rho_{earth}(2n+1)}(1 + k'_n - h'_n)\eta_n, \tag{8}$$

where $\rho_0 \approx 1035$ kg m^{-3} is the average density of seawater, $\rho_{earth} \approx 5518$ kg m^{-3} is the average density of the solid earth, n is an index of the spherical harmonics, and the η_n's are the nth spherical harmonics of the tidal elevation η. The load numbers h'_n and k'_n, introduced in Munk and MacDonald (1960), respectively account for solid-earth yielding and the resulting perturbation potential. We see from equation (8) that the SAL term η_{SAL} depends on the tidal elevations η themselves. The η_{SAL} term is more spatially complex than the η_{EQ} term because, as we will see shortly in Fig. 13.12, the ocean tide has a richer spatial structure than the degree-two spherical harmonic equilibrium tide. The ocean tide contains many spherical harmonic degrees, and the loading and self-gravitation responses are functions of these degrees via (8). The SAL term must therefore be evaluated either by decomposing the tides into spherical harmonics, or by using Green's functions, both of which are computationally expensive. Hendershott (1972) and Gordeev et al. (1977) demonstrated that the SAL effects are of first-order importance to tide modeling. It is not possible to model the global barotropic tides accurately without properly accounting for the SAL term.

Because spherical harmonics are computationally expensive, η_{SAL} is usually not computed inline in ocean models, with some notable exceptions such as Stepanov and Hughes (2004), Kuhlmann et al. (2011), and Vinogradova et al. (2015). To save computational expense, the SAL term is sometimes calculated with a "scalar approximation" (Accad and Pekeris, 1978; Ray, 1998) for which

$$\eta_{SAL} \approx \beta\eta, \tag{9}$$

where β is a constant, usually taken to be about 0.09. As Ray (1998) and others have shown, the scalar approximation is not accurate enough for the most exacting tidal applications. A more accurate iterative method can be employed where resources allow. In the iterative method, one first estimates η_{SAL} with (9), runs the model out, and then uses the full spherical harmonic treatment given by (8) in a less expensive offline calculation. Finally, one takes advantage of the periodicity of tides to construct amplitude and phase maps, which are then used in the next iteration, and so on, until the results converge. Numerical devices are often employed to achieve convergence with a smaller number of iterations—see Arbic et al. (2004) and Egbert et al. (2004) for more discussion.

The early HYCOM "wind plus tides" simulations use a scalar approximation for the SAL term. More recent HYCOM simulations, beginning with the simulations described in Ngodock et al. (2016), have used the SAL maps from the Egbert et al. (1994) TPXO model.[12] The latter approach is generally the most accurate, but the iterative method is more self-consistent. The scalar approximation is the least accurate of the three approaches to SAL described above.

Quadratic bottom boundary layer drag and parameterized topographic internal wave drag

This section is about quadratic bottom boundary layer drag and parameterized topographic internal wave drag, the two main damping mechanisms that have been used thus far in global barotropic tide models and global internal tide and IGW continuum models. Taylor (1919), through examination of tidal dissipation in the Irish Sea, argued that bottom boundary layer drag should be modeled as quadratic in the velocity, with a drag coefficient of about 0.002. His formulation for quadratic bottom drag is commonly used today in ocean models, of both tidal and non-tidal motions. Because the energy budget equation for a model is derived through multiplication of the momentum equation by velocity, the quadratic bottom boundary layer drag yields a dissipation that is cubic in the velocity. Tidal velocities on shelves can be as large as 1 m s^{-1}, much larger than open-ocean tidal velocities, which are typically about 1-2 cm s^{-1}. Therefore, in global tidal models, dissipation by the quadratic bottom boundary layer drag term takes place primarily in coastal areas.

Motivated by Egbert and Ray's demonstration of barotropic tidal energy loss over topographic features, many recent barotropic tide models, beginning with the work of Jayne and St. Laurent

[12] Ngodock et al. (2016) displayed some prior solutions for which the SAL term was computed either iteratively, or using a scalar approximation. The ASEnKF solutions in Ngodock et al. (2016) employed SAL fields taken from the TPXO model, but the text did not make that clear. This omission led to Savage et al. (2017b) mistakenly stating that the HYCOM solutions they analyzed, taken from Ngodock's work, employed an iterative SAL.

(2001), have included a parameterized topographic internal wave drag term in the momentum equation. In the Jayne and St. Laurent (2001) formulation, the wave drag varies in space, as a function of the stratification at the bottom of the ocean, the RMS heights of small-scale topographic features, and the flow velocity. The horizontal length scales of topographic features also enter into the formulation, as a spatially constant tuning parameter. More complex formulations of wave drag, often based upon spatially varying tensors, are used in Arbic et al. (2004), Egbert et al. (2004), Nycander (2005), Lyard et al. (2006), and other studies. Arbic et al. (2004) employed a version of the atmospheric wave drag scheme of Garner (2005). See Nycander (2005) for development of a similar tensor formulation. These drag tensors depend on the local spectrum of topographic heights and horizontal length scales, and on stratification.

Employing wave drag, or other IGW damping parameterizations, in baroclinic tide models is more complex. First of all, the question arises as to whether one should parameterize IGW damping in a model that resolves some of the internal wave spectrum. Arbic et al. (2004), Arbic et al. (2010), Ansong et al. (2015), and Buijsman et al. (2016) have argued that wave drag (or, at least, some parameterized sink of internal wave momentum) is necessary in global baroclinic tide models, because such models do not resolve the actual breaking of internal tides and therefore require a parameterized momentum sink—which they take to be topographic wave drag—to make up for this deficiency. Some internal tide and wave modelers have not employed wave drag, either because they disagree with the point of view described above, or because they do not want to add another term into their models. If one does assume that a topographic wave drag or other IGW damping is needed, this introduces some numerical complexities. For instance, the question arises as to whether the wave drag should be applied to the bottom flow, barotropic flow, or some other flow. Parameterizations of upper-ocean wave-wave interactions, which have not been implemented in global internal wave models to date, would have to act on flows throughout the water column. In Arbic et al. (2004) and in the HYCOM simulations described here, a parameterized topographic wave drag is applied to the bottom flow, based upon the consideration that the bottom flow is the flow that actually interacts with topographic features. This follows the practice of atmospheric modelers, but raises another point of frequent discussion and argument.

Finally, there is the question of what to do about wave drag or other IGW damping in simulations, such as the ones described in this book chapter, that resolve both tidal and non-tidal motions. Non-tidal motions, such as low-frequency mesoscale eddies and currents, also likely generate an internal wave field that acts as an important momentum and energy sink (e.g., Nikurashin and Ferrari, 2011; Scott et al., 2011; Trossman et al., 2013, 2016). Wave drag acts on both tidal and non-tidal motions, but is quantitatively different in the two limits (Bell, 1975). The Trossman et al. (2013, 2016) papers employed the first inline insertion of wave drag into high-resolution models of the eddying general circulation. Trossman et al. (2013, 2016) found that the wave drag was a significant energy sink for the general circulation, and that the statistics of mesoscale eddies are significantly impacted by wave drag. The Trossman et al. (2013, 2016) simulations were done with HYCOM, but in order to avoid the problem discussed above—that wave drag acts differently on tidal and non-tidal flows—the Trossman et al. HYCOM simulations

did not include tides. In the HYCOM simulations that include both tidal and non-tidal motions, such as the simulations that we focus on in this book chapter, the flow averaged over the bottom 500 meters is saved over a period of time of order 1-2 days (the exact number of hourly snapshots saved has been changed as the HYCOM tide simulations have evolved). Then a filter in time is employed to separate the tidal and non-tidal motions, and the wave drag is employed only on the tidal flow. The filter separates tidal and non-tidal motions imperfectly. See Arbic et al. (2010) for a description of the procedure, which produced some numerical artifacts in that first paper (see for instance the artificially large kinetic energy in the Gulf of Mexico and other regions in Figure 2b of that paper). In the subsequent HYCOM tides papers, beginning with Shriver et al. (2012), the artifacts have been greatly reduced. However, the question of how to emply wave drag in models containing both tidal and non-tidal motions is still a matter of active research.

As noted in Ansong et al. (2015) and MacKinnon et al. (2017), among others, in the actual ocean, internal tides likely lose their energy by a variety of mechanisms, including upper-ocean wave-wave interactions (e.g., McComas and Bretherton, 1977), interaction with mean flows and eddies (e.g., Dunphy and Lamb, 2014), and scattering into higher vertical modes and dissipation by bottom friction on continental shelves (e.g., Kelly et al., 2013). No parameterizations of these other internal tide damping processes have been incorporated into the HYCOM tides simulations, which for simplicity employ only a parameterized topographic wave drag meant to parameterize damping via breaking of high-mode motions. No parameterizations of wave drag or of any other internal wave damping mechanisms have been employed in the MITgcm tides simulations discussed here, or, to the best of our knowledge, in any of the other "wind plus tides" simulations performed thus far by modeling groups outside of the HYCOM modeling group. The wave drag scheme employed in earlier HYCOM papers was based on the Garner (2005) scheme. Buijsman et al. (2015) provides a detailed discussion of the performance of HYCOM barotropic tide simulations using various wave drag schemes. Buijsman et al. (2015) found that the simpler scheme of Jayne and St. Laurent (2001) produced errors with respect to TPXO that were comparable to the errors produced with more complex wave drag schemes. As a result, a decision was made to use the Jayne and St. Laurent (2001) scheme in our most recent HYCOM three-dimensional "wind plus tides" simulations.

Shallow-water tidal equations

We now describe the shallow-water tidal equations. Barotropic tides obey the shallow-water equations (Gill, 1982), which apply to motions having wavelengths that greatly exceed ocean depths. Shallow-water motions are hydrostatic, meaning that accelerations do not enter into the primary balance of forces in the vertical direction.

The barotropic tidal elevations do not equal the equilibrium tidal potential for a variety of reasons. First, for an ocean with an average depth of 4000 m, shallow-water waves travel about 200 m s^{-1}, which is not fast enough for the waves to stay under the Moon as it orbits the Earth.[13]

[13] Because waves in the solid earth travel rapidly, through both continental and oceanic crust, the solid-earth body tides do follow the equilibrium tidal forcing more closely. This is why the effects of solid-earth body tides represent a simple alteration of the astronomical tidal potential—multiplication by $1 + k_2 - h_2$.

Continents obstruct oceanic flows, another reason that the shallow-water waves cannot follow the equilibrium tidal forcing. Further complexities in the ocean tide response to equilibrium tidal forcing include the Coriolis force, frictional forces, and solid-earth body and load tides. The tides in the ocean represent a dynamical response, including all of the factors described above, to the equilibrium tidal forcing. Many authors have argued that the tidal response to astronomical forcing is in resonance (Wunsch, 1972; Garrett and Greenberg, 1977; Heath, 1981; Arbic et al., 2009), because the spatial structure and frequency of astronomical forcing is not dissimilar to the normal modes one obtains from the unforced shallow-water equations (Platzman et al., 1981; Platzman, 1991; Zahel and Müller, 2005; Müller, 2007). Numerous studies have argued that the large tides seen in some coastal regions around the globe (e.g., the Bay of Fundy, the Hudson Strait, the Northwest European Shelf, and other areas) are due to resonances in these regions (Garrett, 1972; Clarke, 1991; Arbic et al., 2007; Cummins et al., 2010; among others).

In the case of a one-layer (barotropic) shallow-water model, if we assume a tensor form of the wave drag, the governing momentum equation is

$$\frac{\partial \vec{u}}{\partial t} + \vec{u} \bullet \nabla \vec{u} + f\hat{k} \times \vec{u} = -g\nabla(\eta - \eta_{EQ} - \eta_{SAL}) + \frac{\nabla \cdot [K_H(H+\eta)\nabla \vec{u}]}{H+\eta} - \frac{c_d|\vec{u}|\vec{u}}{H+\eta} + \frac{\overline{T}\vec{u}}{\rho_0(H+\eta)}, \tag{10}$$

and the governing mass conservation equation is

$$\frac{\partial \eta}{\partial t} + \nabla \bullet [(H+\eta)\vec{u}] = 0, \tag{11}$$

where $\vec{u}$ is the two-dimensional horizontal velocity vector, f is the Coriolis parameter, $\hat{k}$ is a unit vector in the vertical direction, g is gravitational acceleration, K_H is the horizontal eddy viscosity, H is the resting water depth, η is the perturbation tidal elevation, c_d is the quadratic drag coefficient (usually set to a value close to 0.0025), and $\overline{T}$ is the topographic internal wave drag tensor. The form of the one-layer shallow-water equations given in Arbic et al. (2004) is equivalent to the above, though written in a slightly different (flux-divergent) form. The form of the governing equations for two- and multi-layer shallow water models with only tidal forcing present are given in, for instance, Arbic et al. (2004) and Simmons et al. (2004b), respectively. A simplified form of the modern shallow-water equations lacking, for instance, the nonlinear advective terms and the damping terms, was written down by Laplace (Laplace, 1775, 1776). Laplace's equations are known as the "Laplace tidal equations." The study of tides has indeed contributed much to the development of ocean models.

The greater complexity of the ocean tide response, relative to the simple structure of the astronomical forcing, is illustrated in Fig. 13.12, which is a global map of the amplitudes and phases of the M_2 surface tidal elevations from Egbert et al. (1994). Tidal results are often displayed in amplitude and phase maps. A tidal harmonic analysis, which employs a least-squares fitting procedure, is generally used to extract tidal amplitudes and phases from observations or from model outputs (Foreman, 1977, 2004; Pawlowicz et al., 2002; Foreman et al., 2009). Amplitude and phase

maps take advantage of the periodicity of the tides and assume that a scalar tidal variable V can be written as

$$V(\phi,\lambda) = Amplitude(\phi,\lambda) f(t_{ref}) cos[\omega(t - t_{ref}) + \chi(t_{ref}) + \nu(t_{ref}) - phase(\phi,\lambda)]. \quad (12)$$

The amplitudes and phases of tidal elevations can be used to compute the time-averaged discrepancy between two different estimates of the tides. The squared discrepancy D^2 between, for instance, modeled tidal elevations η_{MODEL} and observed elevations η_{OBS} at a point location is defined as

$$D^2 = < (\eta_{MODEL} - \eta_{OBS})^2 > \quad (13)$$

where < > denotes a time average, over an integer number of tidal periods. It is easily shown that D^2 can be written in terms of tidal amplitudes and phases, viz.

$$D^2 = \frac{1}{2}(A^2_{MODEL} + A^2_{OBS}) - A_{MODEL} A_{OBS} cos(\phi_{MODEL} - \phi_{OBS}), \quad (14)$$

where A_{MODEL} and A_{OBS} are amplitudes of the model and observations, respectively, and ϕ_{MODEL} and ϕ_{OBS} are phases. Alternatively, one can write, as in Shriver et al. (2012),

$$D^2 = \frac{1}{2}(A_{MODEL} - A_{OBS})^2 + A_{MODEL} A_{OBS}[1 - cos(\phi_{MODEL} - \phi_{OBS})], \quad (15)$$

where the first term on the right-hand side is an amplitude error and the second is an amplitude-weighted phase error. Often an area-weighted D^2 is calculated in the tide literature. In such cases an area-weighted RMS error is taken as the square root of the area-weighted D^2, viz.

$$D = \sqrt{\frac{\int\int < (\eta_{MODEL} - \eta_{OBS})^2 > dA}{\int\int dA}}. \quad (16)$$

Brief synopsis of internal wave theory

We briefly summarize two theoretical results that we will use later to interpret some of our modeled IGW results. First, as is shown in the appendix, the linear dispersion relation for plane IGWs can be written as

$$\omega^2 = f^2 + c_e^2 K^2, \quad (17)$$

where ω and K are the frequency and horizontal wavenumber, and c_e is the eigenspeed, of a particular vertical mode of interest.[14] Equation (17) implies that $|f| \leq \omega$. As can be seen from equation (59) in the appendix, the inequality $f \leq \omega \leq N$ holds in the special case of a constant N throughout the water column. Second, we note that the Garrett and Munk (1975) model for the IGW spectrum predicts that IGW spectra will fall off as ω^{-2} and as m^{-2}, where m is vertical wavenumber.

[14] Again, we remind the reader that frequency is denoted by σ in the appendix.

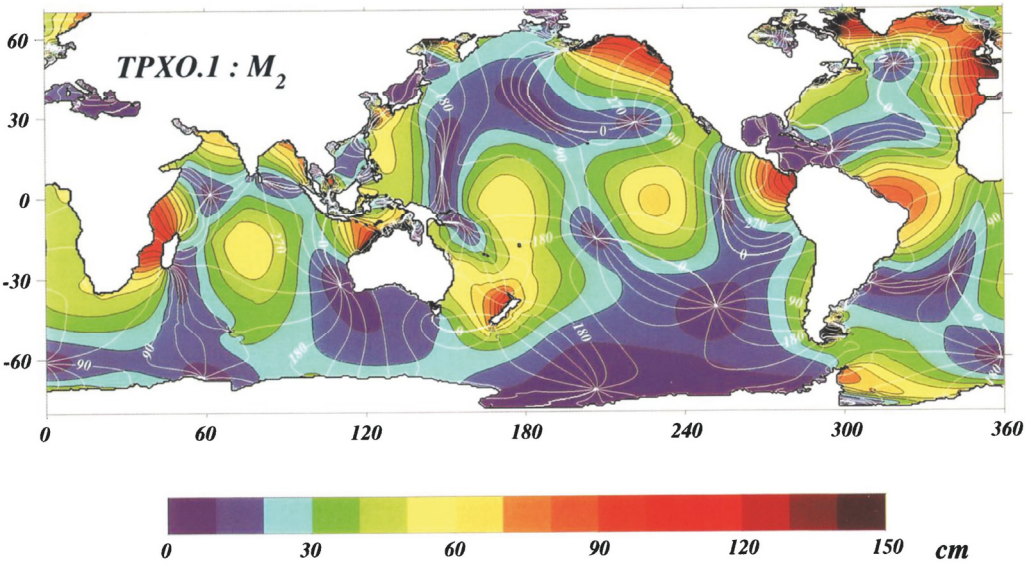

Figure 13.12. Global amplitude and phase maps of M_2 surface elevations, from TPXO model. Contour intervals are 10 cm for amplitude and 30° for Greenwich phase. Reproduced from Plate 3 of Egbert et al. (1994), ©American Geophysical Union, Wiley Online Library, used with permission.

Results from First HYCOM "Wind Plus Tides" Simulations

This section displays some results from the first HYCOM simulations forced concurrently by atmospheric fields and the astronomical tidal potential (Arbic et al., 2010); one result shown in this section is taken from the second round of HYCOM "wind plus tides" simulations (Arbic et al., 2012a; Shriver et al., 2012). Fig. 13.13a displays a global map of the amplitudes of the M_2 internal tide SSH signature (computed from steric SSH) in an experiment with two layers, a horizontally uniform stratification, and only M_2 tidal forcing present—in other words, in an experiment like those in Arbic et al. (2004) and Simmons et al. (2004b). Fig. 13.13b displays the M_2 internal tide SSH amplitude map in a simulation forced by both atmospheric fields and tides. There are some qualitative similarities between the two maps. For instance, internal tide generation regions such as Hawai'i, the French Polynesian Islands, and others, are clearly visible in both plots. There are quantitative differences throughout the globe, demonstrating (not surprisingly) that the internal tides are very different in a simulation that includes a realistic horizontally varying stratification. The differences are greatest in polar regions, where the oceanic stratification is weaker than the subtropical stratification employed globally in the simulation shown in Fig. 13.13a. Under the more realistic conditions in Fig. 13.13b, the internal tide signatures in polar regions are much weaker.

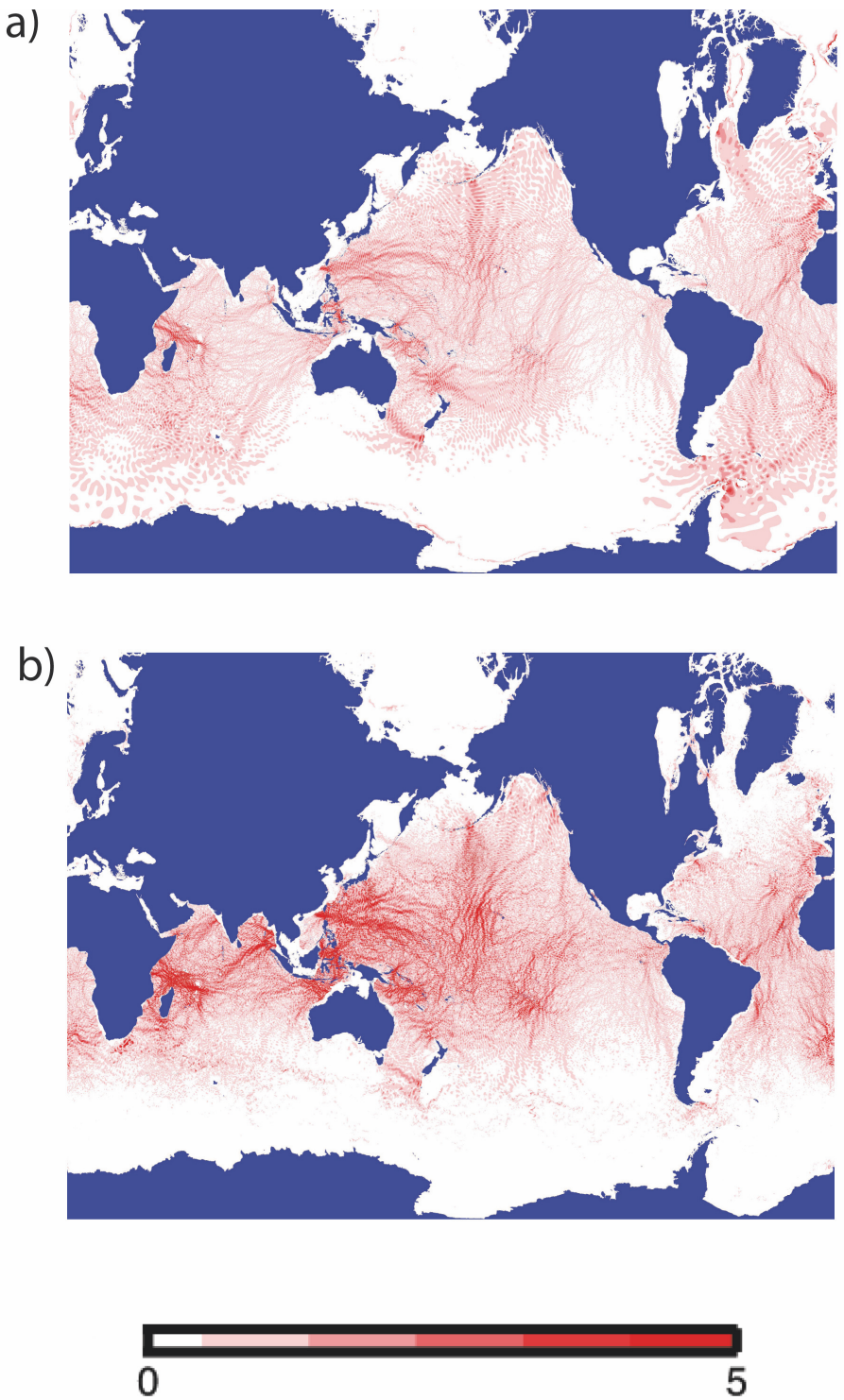

Figure 13.13. Amplitude (cm) of M_2 internal tide signature, computed from steric SSH, in (a) HYCOM simulation with two-layer, horizontally uniform stratification, and M_2 tidal forcing only, as in Arbic et al. (2004) and Simmons et al. (2004b), and (b) early HYCOM "wind plus tides" simulation, with a 32-layer, horizontally non-uniform stratification, forced by atmospheric fields as well as the M_2 astronomical tidal potential. Reproduced from Figure 4 of Arbic et al. (2010).

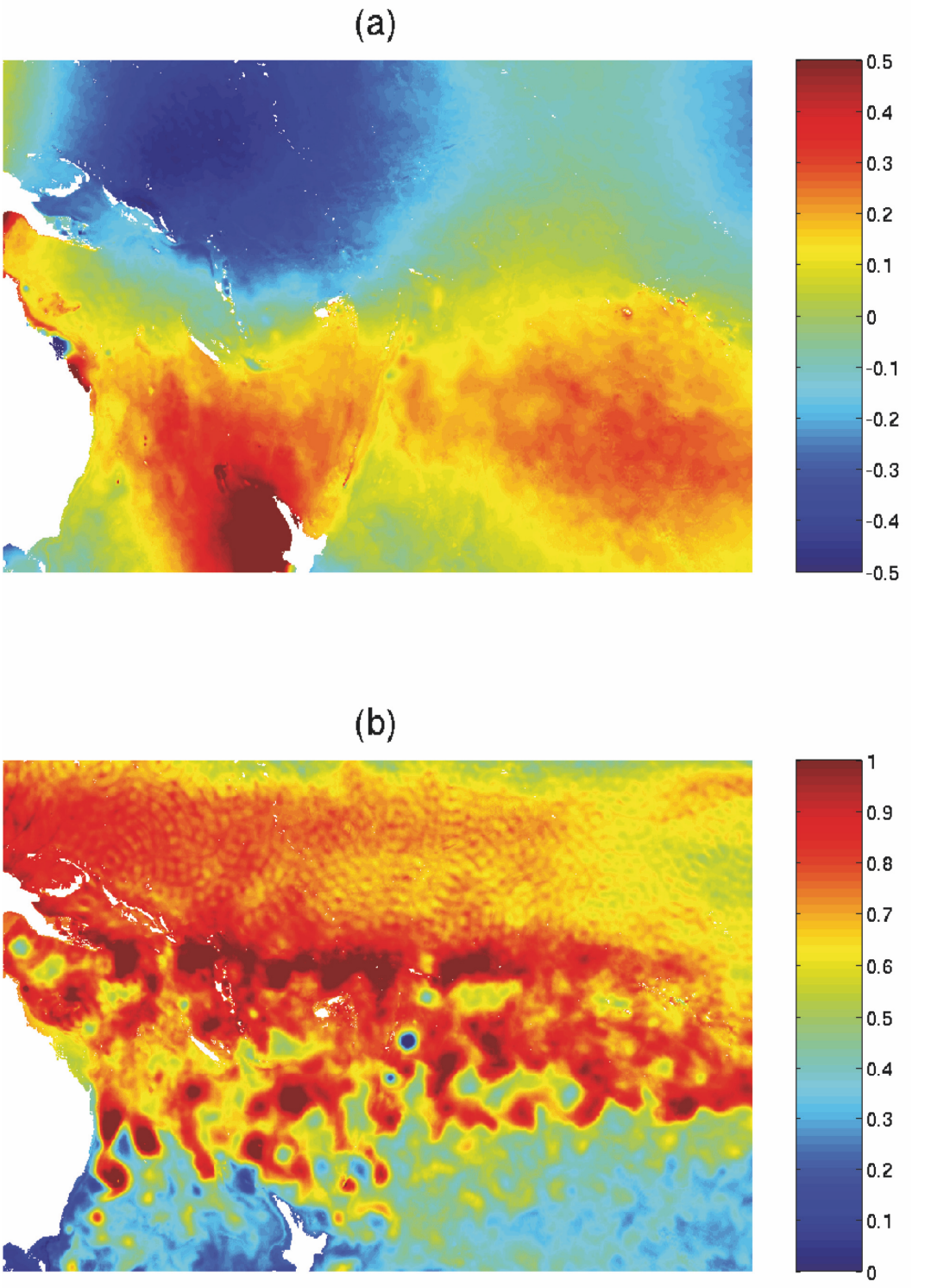

Figure 13.14. Snapshot of (a) non-steric and (b) steric sea surface heights (m) in the Southwest Pacific on June 30, 2006 at 00Z, from an early HYCOM simulation forced by both atmospheric fields and tides. Reproduced from Figure 8 of Arbic et al. (2010).

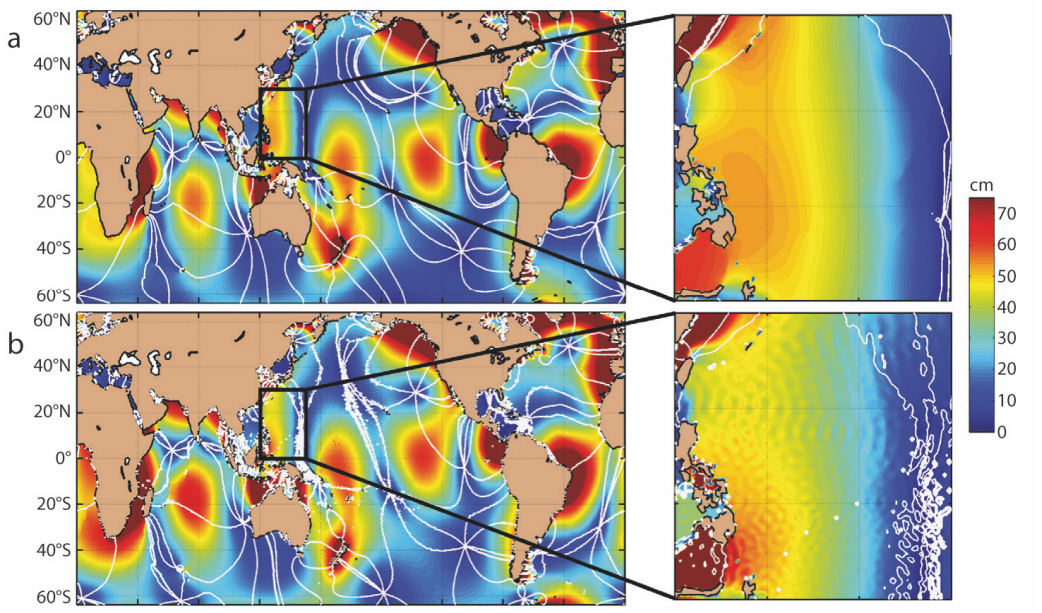

Figure 13.15. (a) Amplitude (cm) of M_2 surface tidal elevation in TPXO (Egbert et al., 1994), a highly accurate barotropic tide model constrained by satellite altimetry. (b) Amplitude (cm) of M_2 surface tidal elevation in early "wind plus tides" 32-layer HYCOM simulation with concurrent atmospheric and tidal forcing, which yields barotropic tides, internal tides, and mesoscale eddies. White curves in (a) and (b) are contours of constant phase. Insets to the right of (a) and (b) display amplitude and phase in the western Pacific region delineated by boxes in (a) and (b). Reproduced from Figure 1 of Arbic et al. (2012a).

The separation of HYCOM SSH fields into steric and non-steric components (see appendix of Savage et al., 2017a) has proven to be useful in visualizing different classes of motions simulated by the HYCOM "wind plus tides" simulations. Fig. 13.14 shows snapshots of non-steric and steric SSH in the South Pacific from the early simulations discussed in Arbic et al. (2010). The non-steric fields are dominated by the large-scale barotropic tides. The steric fields display both the internal tides—manifesting themselves in a small-scale "honeycomb" texture—and mesoscale eddies (which are more vortical). Animations of these fields reveal that the honeycomb patterns are high-frequency (because they are tidal) while the mesoscale eddies evolve more slowly.

Fig. 13.15 shows global maps of the amplitude and phase of M_2 surface elevations, in both HYCOM and in TPXO. The inset plots focus in on a region of the western Pacific where strong internal tides are present. The contrast between the inset of TPXO, which does not include internal tides, and the inset of HYCOM, illustrates the impact of internal tides upon the total (barotropic plus internal) surface tidal elevation. The internal tides, though of smaller amplitude, impart small-scale perturbations to both amplitude and phase contours, as in the altimeter data shown in Fig. 13.4. The amplitude perturbations have a "honeycomb" appearance, as in Fig. 13.14b.

Fig. 13.16 shows zonal velocities and isopycnal positions, in a section through Hawai'i, from the same HYCOM "wind plus tides" simulation. A snapshot is shown in (a), while a 25-hour mean is shown in (b). The snapshot reveals more structure in both the velocity and isopycnal position fields; this high-frequency structure is averaged out in the 25-hour mean.

Model Comparison with Observations and Theory

In this section, we compare the modeled internal tides and internal gravity wave continuum with observations. The observations used for comparison include satellite altimetry data, and observations from in-situ platforms such as moorings. For the purposes of this section, an altimeter-constrained model such as TPXO is considered to represent "observations". Because there have been many more model-observational comparisons with HYCOM than with MITgcm, we focus more on HYCOM than on MITgcm in this section. We compare the IGW spectra in both HYCOM and MITgcm with linear internal gravity wave theory.

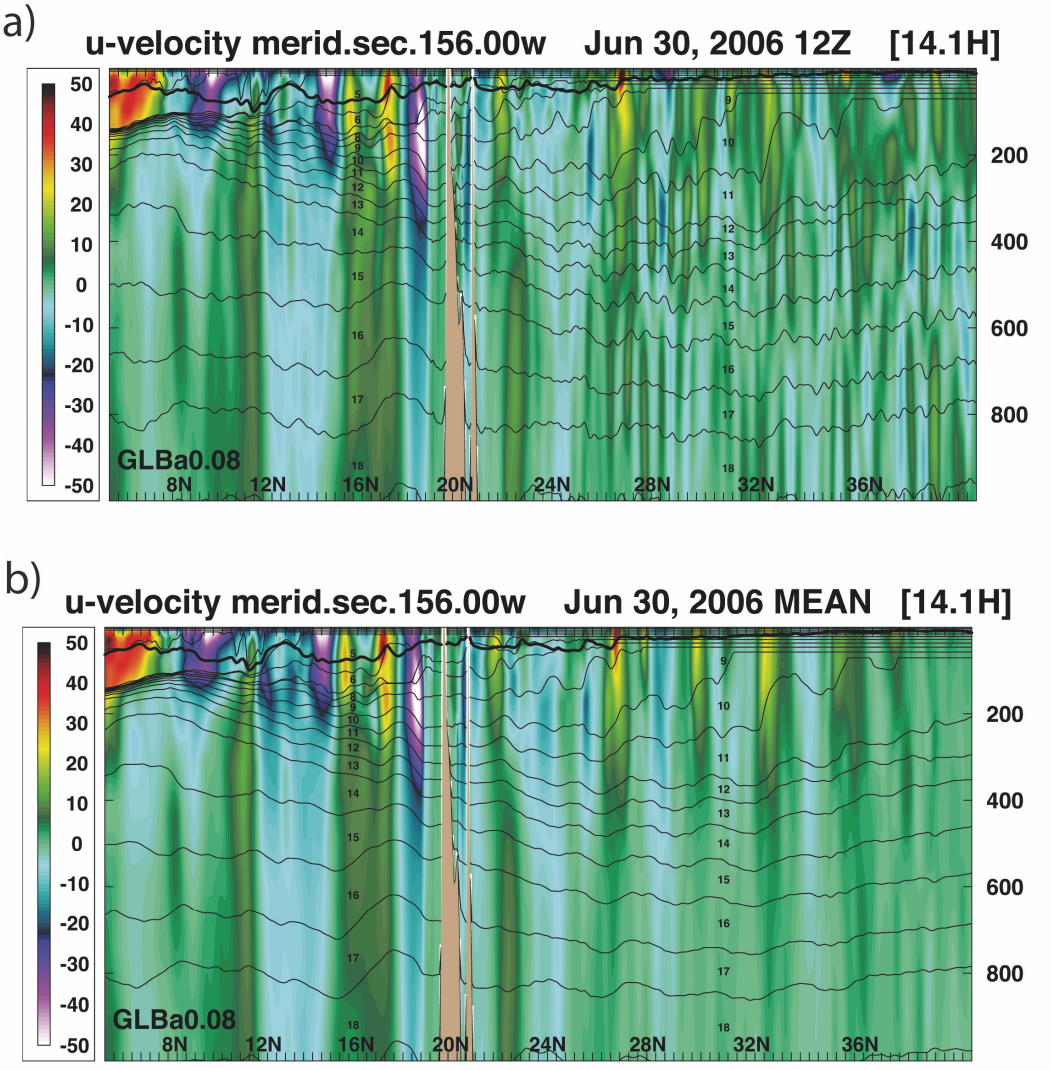

Figure 13.16. Zonal velocity (cm s^{-1}) in 156°W section through Hawai'i on June 30, 2006 from an early HYCOM simulation forced by both atmospheric fields and tides; (a) snapshot and (b) 25-hour mean. Isopycnal positions (black curves) shown versus depth in meters (right axes). Reproduced from Figure 10 of Arbic et al. (2010).

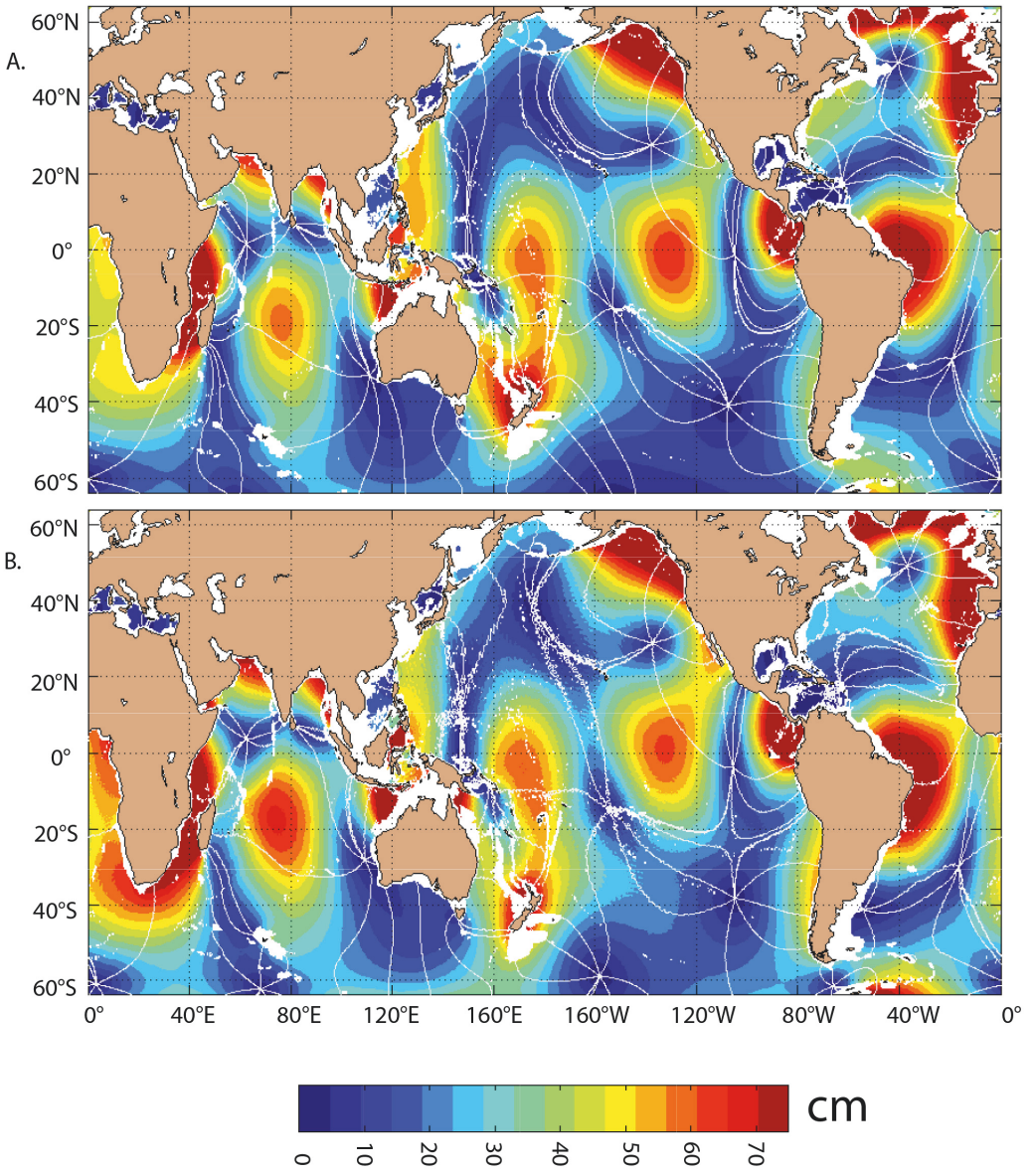

Figure 13.17. Amplitude (cm) of M_2 surface tidal elevation in (A) TPXO7.2 (an update to the model described by Egbert et al., 1994), a barotropic tide model constrained by satellite altimetry, and (B) 32-layer HYCOM simulations forced concurrently by atmospheric fields and the tidal gravitational potential. Lines of constant phase plotted every 45° are overlaid in white. Reproduced from Figure 2 of Shriver et al. (2012), ©American Geophysical Union, Wiley Online Library, used with permission.

Comparison with altimetry

Fig. 13.17 compares the M_2 surface tidal elevation amplitudes and phases in the altimeter-constrained model TPXO (A) and in HYCOM (B). Once again, small-scale structure, due to the presence of internal tides, is visible in HYCOM. The gross similarities between the TPXO and

HYCOM fields are clear, but there are also many differences in detail. For instance, the patterns in the eastern equatorial Pacific Ocean and equatorial Indian Ocean clearly differ. Later we will discuss methods that improve the accuracy of the HYCOM barotropic tides over what is seen in Fig. 13.17. Note that in Fig. 13.17 and in succeeding figures taken from Shriver et al. (2012), locations with water depths less than 1500 meters are whited out because the spatial high-pass filtering technique we used to separate barotropic and internal tides does not work well in shallow waters, where the horizontal length scales of barotropic tides are much smaller than in the open ocean.

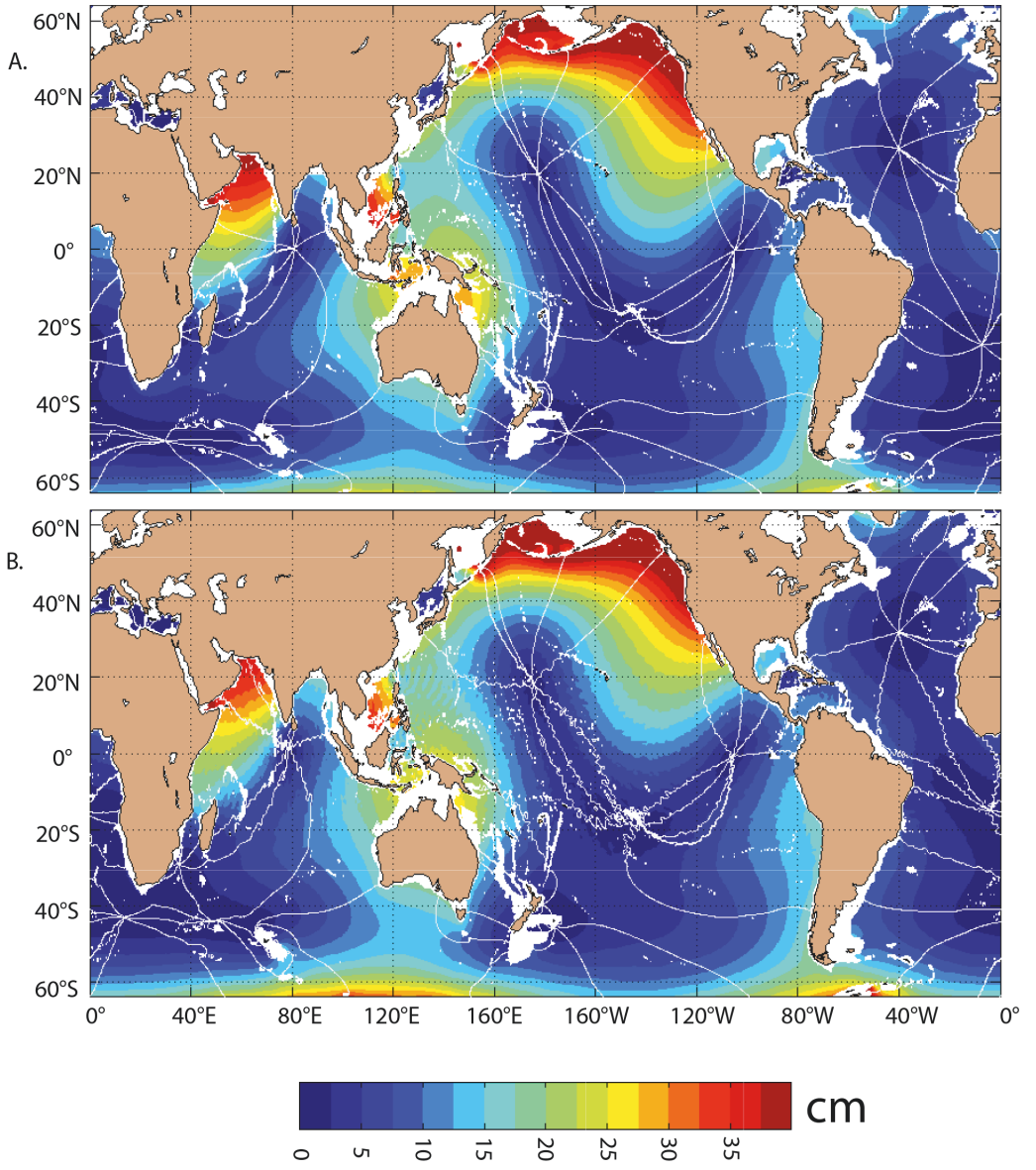

Figure 13.18. As in Fig. 13.17 but for the K_1 tidal constituent. Reproduced from Figure 3 of Shriver et al. (2012), ©American Geophysical Union, Wiley Online Library, used with permission.

Figure 13.18 compares the K_1 surface tidal elevation amplitudes and phases in TPXO (A) and HYCOM (B). We again note the small-scale structures in HYCOM, and the gross similarities and many quantitative differences between the HYCOM and TPXO fields.

Fig. 13.19 compares the stationary M_2 internal tide SSH elevation amplitudes in along-track altimeter data (A; from Ray and Byrne, 2010) and HYCOM (B). As noted in the discussion around Fig. 13.4, in the open ocean, the horizontal scales of internal tides are much less than the horizontal scales of barotropic tides. Therefore, we apply a spatial high-pass filter to the full sea surface height results shown in Fig. 13.17 to obtain the internal tides shown in Fig. 13.19. As with the barotropic tide comparisons above, the internal tide SSH comparison features gross similarities but also many differences in detail; differences are especially clear in the Atlantic Ocean. Both along-track altimetry and HYCOM reveal a small number of significant generation regions, or "hotspots", for instance, Hawai'i, the French Polynesian Islands, Northwest Australia, and others. Both subplots show a "dead zone" for stationary internal tides in the eastern equatorial Pacific. We will return to this "dead zone" in a subsequent section. Spatial averages of amplitudes computed from HYCOM over the hotspot regions outlined by black boxes in (B) agree with averages computed from along-track altimetry to within 15% for the four largest semidiurnal constituents (see Table 2 in Shriver et al., 2012). In later papers (e.g. Ansong et al., 2015), we realized that the duration of the model output impacts the average amplitude one attains, meaning that the Shriver et al. (2012) model values were slight overestimates.

Fig. 13.20 compares the stationary K_1 internal tide SSH elevation amplitudes in along-track altimeter data (A; from Ray and Byrne, 2010) and HYCOM (B). As with the M_2 internal tides, hotspot regions for the K_1 internal tides display gross agreement between HYCOM and along-track altimetry. Spatially-averaged amplitudes computed over the diurnal hotspot regions outlined by black boxes in (B) agree with averages computed from along-track altimetry to within 23% for the four largest diurnal constituents (see Table 3 in Shriver et al., 2012). The most obvious differences in the altimetric vs. HYCOM K_1 internal tides are seen in regions of strong mesoscale eddies and currents, such as the Gulf Stream, Kuroshio, Malvinas, Agulhas, and Antarctic Circumpolar Current regions (denoted by red ellipses in A). All of these regions are poleward of 30°, the latitude for which the K_1 frequency equals the Coriolis parameter *f*. By equation (17), we expect therefore that there should not be propagating diurnal IGWs poleward of 30°. The model results are consistent with this expectation, but the altimeter results are not. As discussed in Shriver et al. (2012) and in earlier references, the 10-day repeat times for the TOPEX/JASON series result in aliasing of tides into longer periods, that lie within the low-frequency broadband mesoscale eddy continuum. Thus, in regions of strong mesoscale eddies, it can be difficult to separate the eddies from internal tides, especially because the two types of motions have similar horizontal length scales. This leads to artificially high estimates of stationary internal tide amplitudes in altimeter data over regions of strong currents.

The global views displayed in the previous two figures do not allow for detailed comparison of individual features. Individual features can be seen in Fig. 13.21, which compares stationary M_2 internal tide amplitudes, in along-track altimetry vs. HYCOM, along ascending tracks in the North

Pacific. While the features in the model output and altimeter data are qualitatively similar, the individual peaks and troughs often do not line up closely. We are continuing to investigate the quality of internal tides in the HYCOM simulations, to see whether recent improvements to the HYCOM barotropic tides, to be discussed in a subsequent section, yield improvements in the model-observational comparison of internal tides.

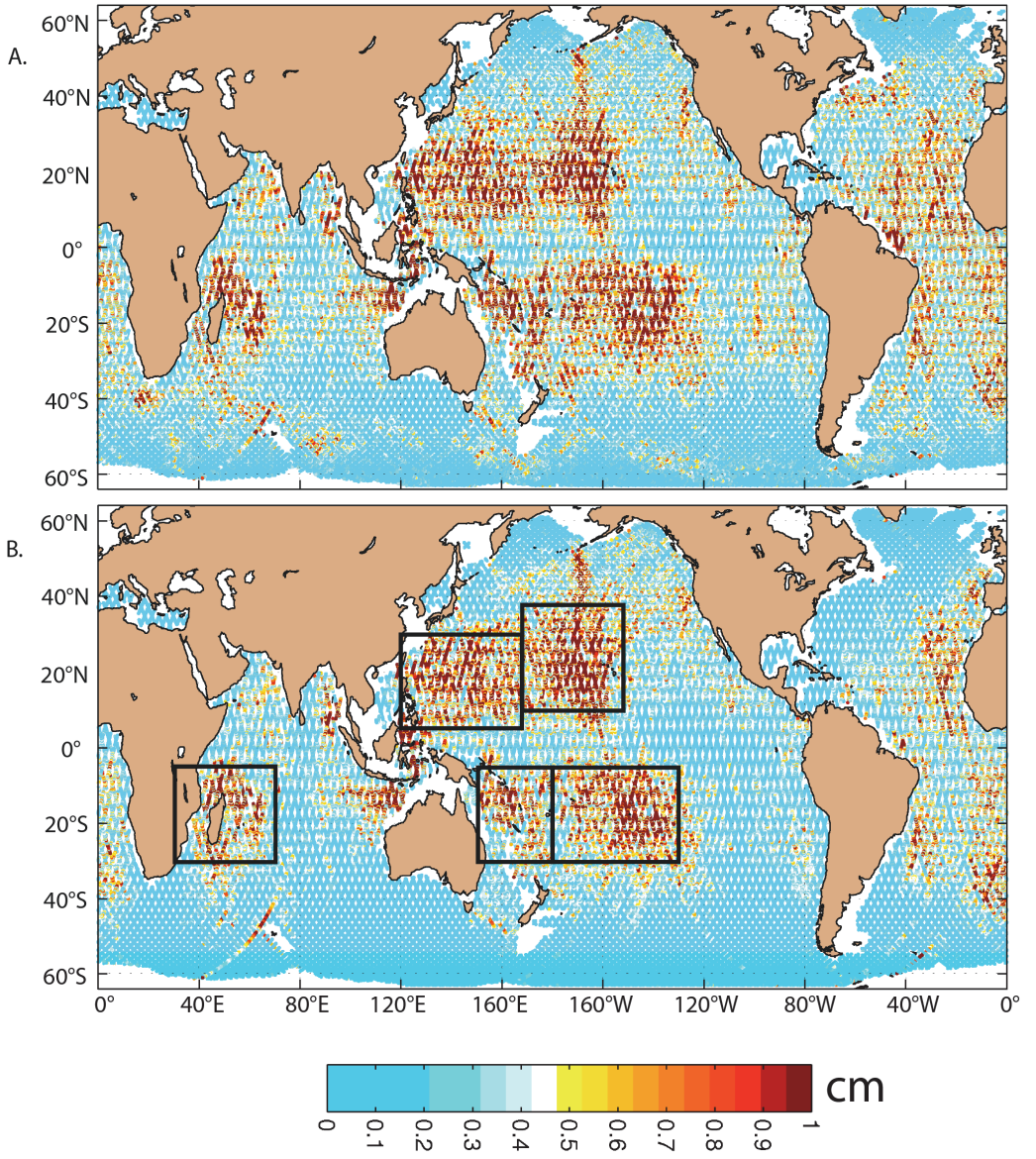

Figure 13.19. The stationary M_2 internal tide amplitude from the (A) along-track altimeter data as in Ray and Byrne (2010) and (B) analysis of HYCOM tidal model output. The five subregions denoted by black boxes in (B) are used to compute the area-averaged amplitudes in Table 2 of Shriver et al. (2012). Reproduced from Figure 7 of Shriver et al. (2012), ©American Geophysical Union, Wiley Online Library, used with permission.

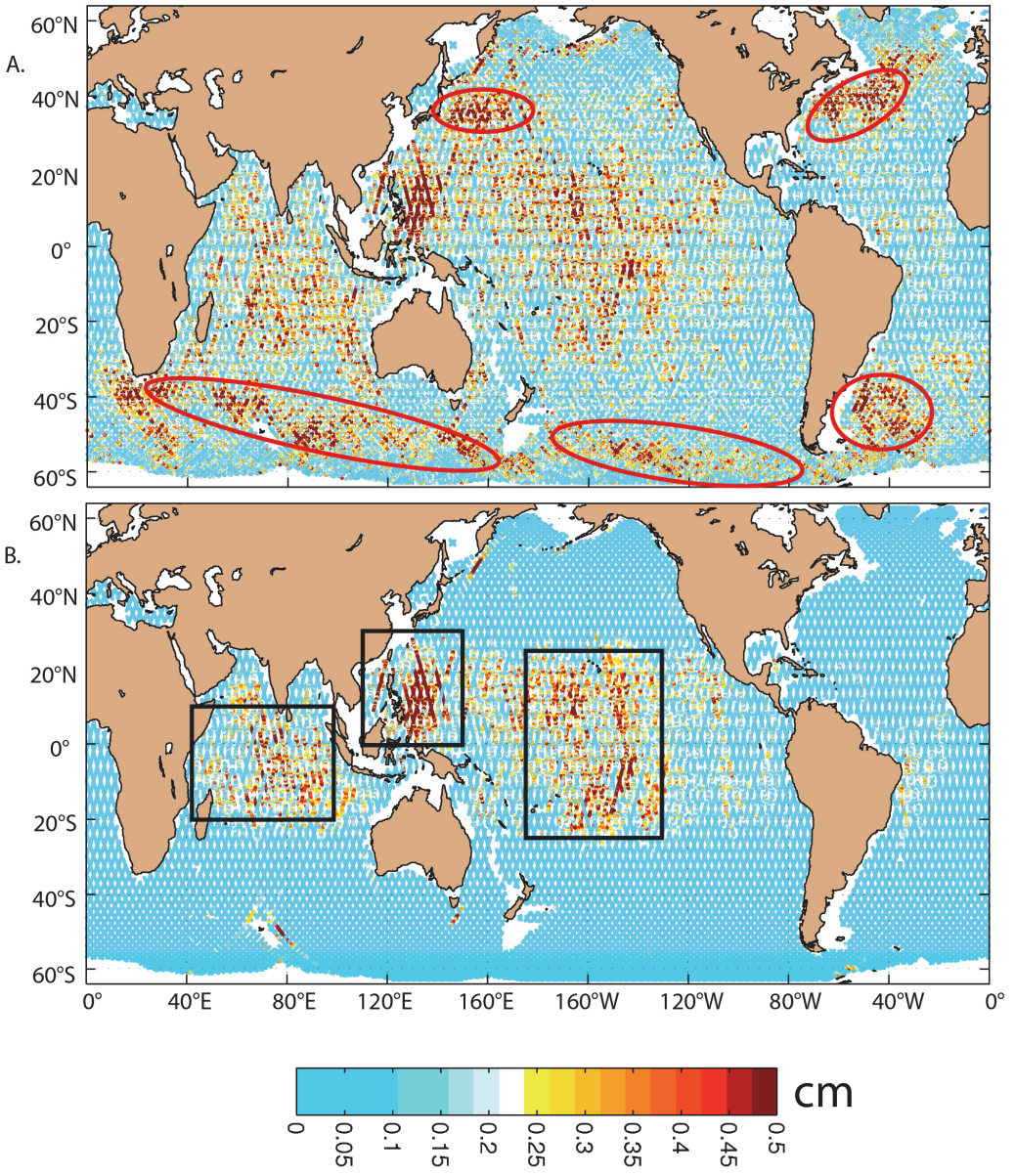

Figure 13.20. As in Fig. 13.19 but for the stationary K_1 internal tide. Reproduced from Figure 8 of Shriver et al. (2012), ©American Geophysical Union, Wiley Online Library, used with permission.

Comparison with moored observational records

We now display comparisons of results from global internal tide and IGW continuum models with results from an archive of historical moored instruments. Observations in the archive are in some ways the antithesis of altimeter records. Individual moored instruments in the archive provide high temporal resolution observations, often putting out measurement information at intervals of one hour or even less. This makes mooring data suitable for computing frequency spectra that encompass a range of oceanic motions, from low-frequency mesoscale eddies to high-frequency

internal tides and the IGW continuum, as in Fig. 13.3. Variables commonly captured in mooring time series include velocity, temperature, and, in newer instruments for which the drift problems in older instruments have been reduced, salinity. We have used a database of archived temperature and velocity records (Scott et al., 2010; Wright et al., 2014), in several model-data comparison studies. Scott et al. (2010) compared the kinetic energy of low-frequency motions, such as mesoscale eddies and currents, in four different "eddying" models, none of which contained tides, vs. the archived current meter data. See Penduff et al. (2006), and Thoppil et al. (2011), for related efforts. Luecke et al. (2017) used the Scott et al. (2010) database to compare low-frequency temperature variance in non-tidal HYCOM simulations vs. moored observations, and Luecke et al. (paper in preparation; Fig. 13.3) compares both low- and high-frequency temperature variance and kinetic energy in HYCOM and MITgcm "wind plus tide" simulations with the archived historical mooring observations.

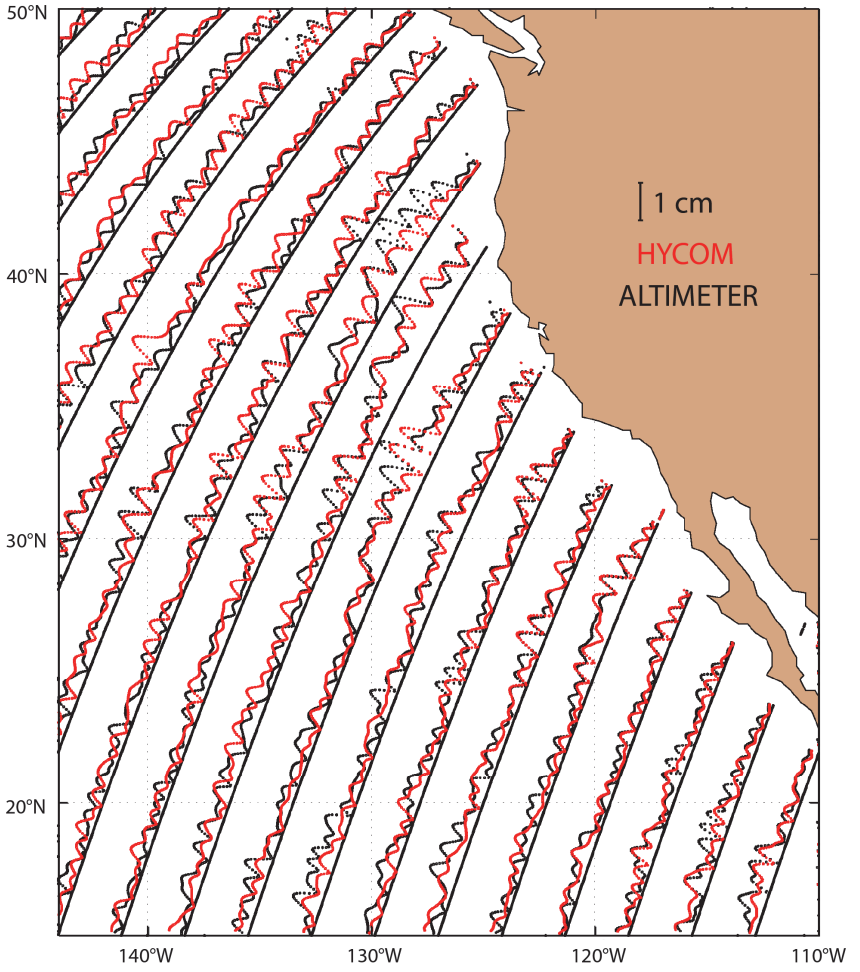

Figure 13.21. M_2 internal tide amplitude along ascending tracks from the HYCOM (red) and altimeter-based analysis (black). For each track, the line showing the coordinates of the track represents a zero amplitude for the tides on that track. The short-scale smoothness is due in part to the application of the band-pass filter and is not due to the response method used in the altimetric-based analysis. Reproduced from Figure 6 of Shriver et al. (2012), ©American Geophysical Union, Wiley Online Library, used with permission.

Timko et al. (2012, 2013) compared tidal currents in HYCOM with tidal currents inferred from the historical observations. Fig. 13.22 compares vertical profiles of the M_2 tidal current semi-major axis and phase at a particular location in the North Pacific, just south of the Aleutians. There is good general agreement throughout the water column, with the model tracking many of the changes seen with depth. However, not all locations show an agreement that is this close.

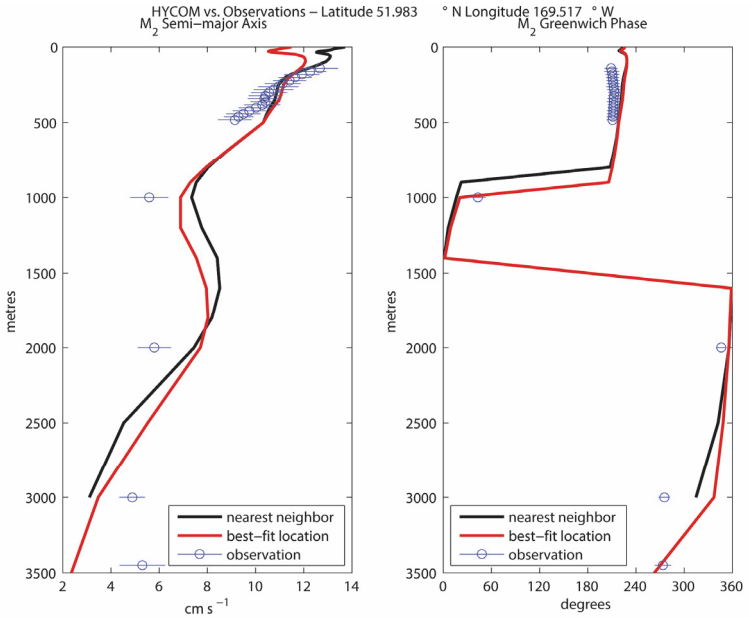

Figure 13.22. Comparison of M_2 semi-major axis and Greenwich phase in HYCOM and in a particular Acoustic Doppler Current Profiler (ADCP) record as a function of depth, at a location given in the plot title. The circles represent the value estimated from the observations and the line through the circle represents the 95% confidence intervals using harmonic tidal analysis. The black curve shows HYCOM values for the model grid point nearest the observation and the red curve shows the model values for the best-fit neighbor from a 9 point block of grid cells surrounding the observation. Reproduced from Figure 2 of Timko et al. (2013), ©American Geophysical Union, Wiley Online Library, used with permission.

Fig. 13.23 compares vertical profiles of M_2, S_2, K_1, and O_1 tidal kinetic energies, averaged over 5468 instrument records at 1618 geographical locations around the globe. As seen in the previous figure, Fig. 13.23 demonstrates that tidal currents vary significantly with depth, i.e. are quite baroclinic. Note that this vertical profile is not representative of a global average—rather it is the average profile over the particular geographical locations employed in the analysis. The model tracks the changes in kinetic energy with depth fairly well for M_2, but less well for S_2, K_1, and O_1. There are some plausible reasons for this. The simulation analyzed for Fig. 13.23 contained the four largest semidiurnal constituents and the four largest diurnal constituents. Storage limitations at the time this simulation was conducted prevented us from saving more than one month of three-dimensional model output. However, one month of output is not enough to separate S_2 from K_2, or to separate K_1 from P_1. In order to avoid this problem in more recent HYCOM simulations, we have employed two strategies. We save longer time series at locations where mooring data is available for comparison. We have also reduced the number of constituents employed, from 8 to 5. The five

constituents employed— M_2, S_2, N_2, K_1, and O_1—can, according to the traditional Rayleigh criterion, be separated with just one month of model output.

Aside from the problem of separating nearby frequencies, another problem with the model output in Fig. 13.23 is that the topographic wave drag was tuned for M_2, not for the diurnal tides. However, theory (e.g., Bell, 1975) informs us that the drag on tidal flows will be frequency-dependent. Skiba et al. (2013) implemented a topographic wave drag tuned specifically for diurnal tides. In the Skiba et al. (2013) simulations, only the K_1 diurnal tide was present. In the HYCOM "wind plus tides" simulations, because both semidiurnal and diurnal tides are present, it is not a simple matter to tune a wave drag separately for semidiurnal and diurnal tides, and at present we continue to tune for the largest constituent M_2.

The variations throughout the water column seen in Figs. 13.22 and 13.23 make clear the limitations of predicting tidal currents with barotropic tide models, as is commonly done. On the other hand, multi-layer "wind plus tides" models will need more vetting before they are commonly used for predicting tidal currents.

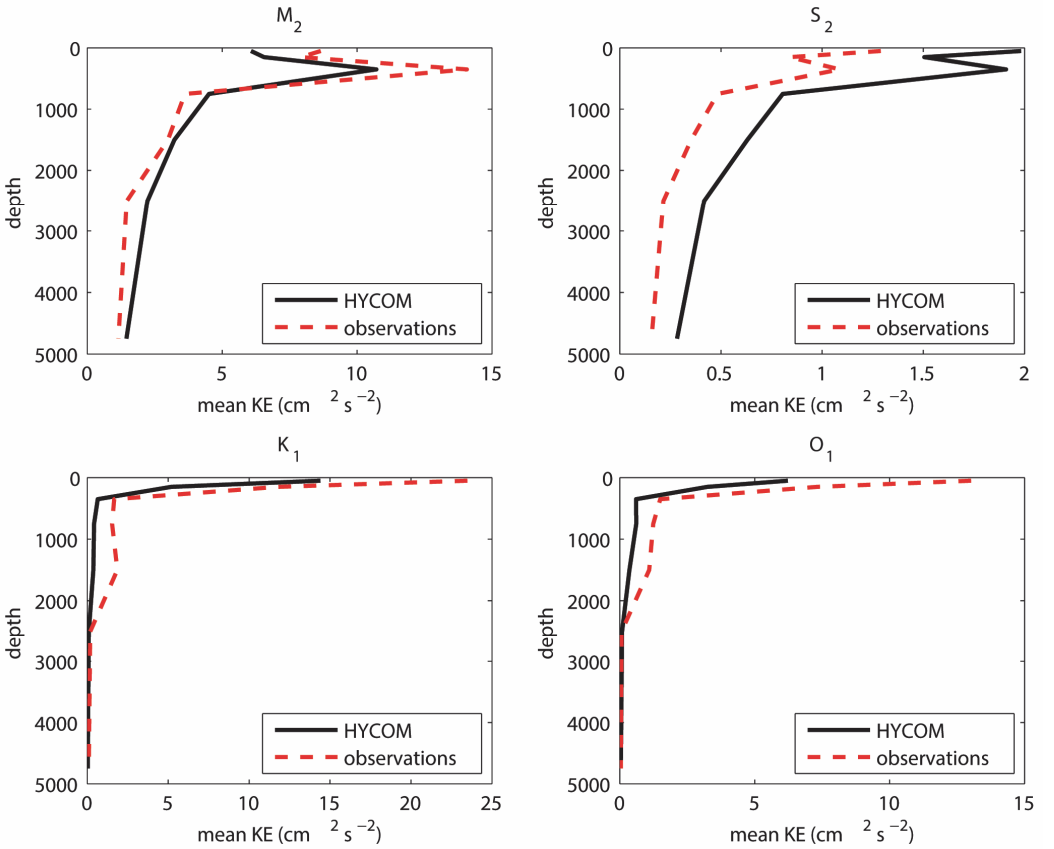

Figure 13.23. Vertical profiles of the HYCOM and observed tidal kinetic energy averaged over 5468 instrument records at 1618 geographic locations throughout the global ocean. The 5468 records, all in deep water (water column depth greater than 1000 m) are sorted into seven depth bins. Reproduced from Figure 5 of Timko et al. (2013), ©American Geophysical Union, Wiley Online Library, used with permission.

Internal tide energy fluxes can also be derived from moorings. Fig. 13.24 compares vertical mode-1 semidiurnal band energy fluxes in HYCOM vs. moorings from the Internal Waves Across the Pacific (IWAP) field campaign (Alford et al., 2007; Zhao et al., 2010; fluxes were taken from the latter paper). The agreement is visusally close at 5 out of the 6 moorings. The 6 moorings shown in Fig. 13.24 are McLane profilers (Doherty et al., 1999), which provide very-high-resolution vertical coverage, in contrast to the sparse vertical coverage of traditional moorings. As is shown in Ansong et al. (2017), the model-observational agreement is not as close as in Fig. 13.24 when we use historical moorings, because sparse vertical coverage does not allow full vertical resolution of baroclinic signals.

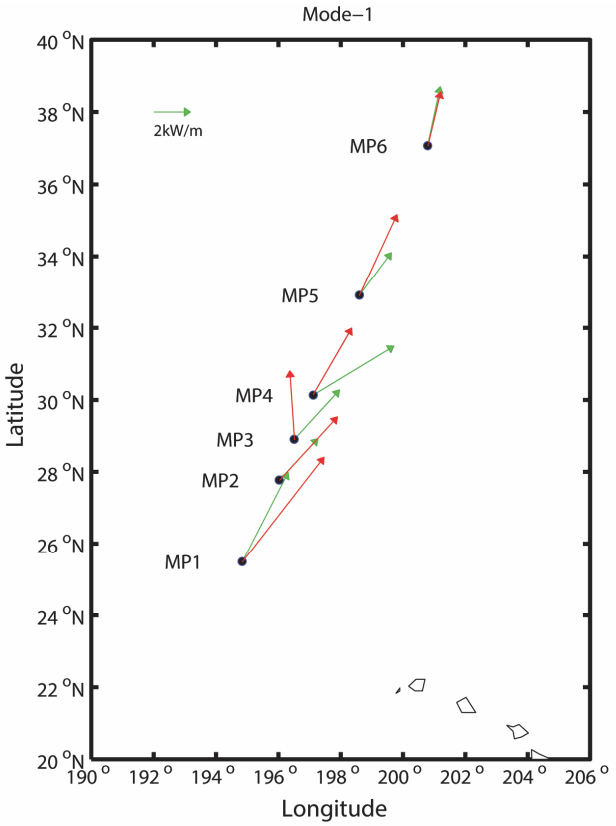

Figure 13.24. Map of depth-integrated vertical mode-1 semidiurnal energy fluxes computed for 1/25° HYCOM (red arrows) and observations (green arrows) from the IWAP experiment (Zhao et al., 2010). Arrow lengths are logarithmic and reference arrows are shown at the top left corner of the plot. Reproduced from Figure 11 of Ansong et al. (2017), ©American Geophysical Union, Wiley Online Library, used with permission.

Moorings provide information on the IGW continuum as well as on internal tides. Fig. 13.25 compares frequency spectra of surface kinetic energy in HYCOM vs. near-surface kinetic energy in historical North Pacific moorings (Schmitz, 1988). The low-frequency continuum, dominated by mesoscale flows, is seen alongside near-inertial peaks, semidiurnal tidal peaks, and the supertidal IGW continuum. The model IGW continuum approaches the observed continuum, and the Garrett and Munk (1975)/Cairns and Williams (1976) spectrum, more closely when horizontal resolution is increased from 1/12.5° to 1/25°.

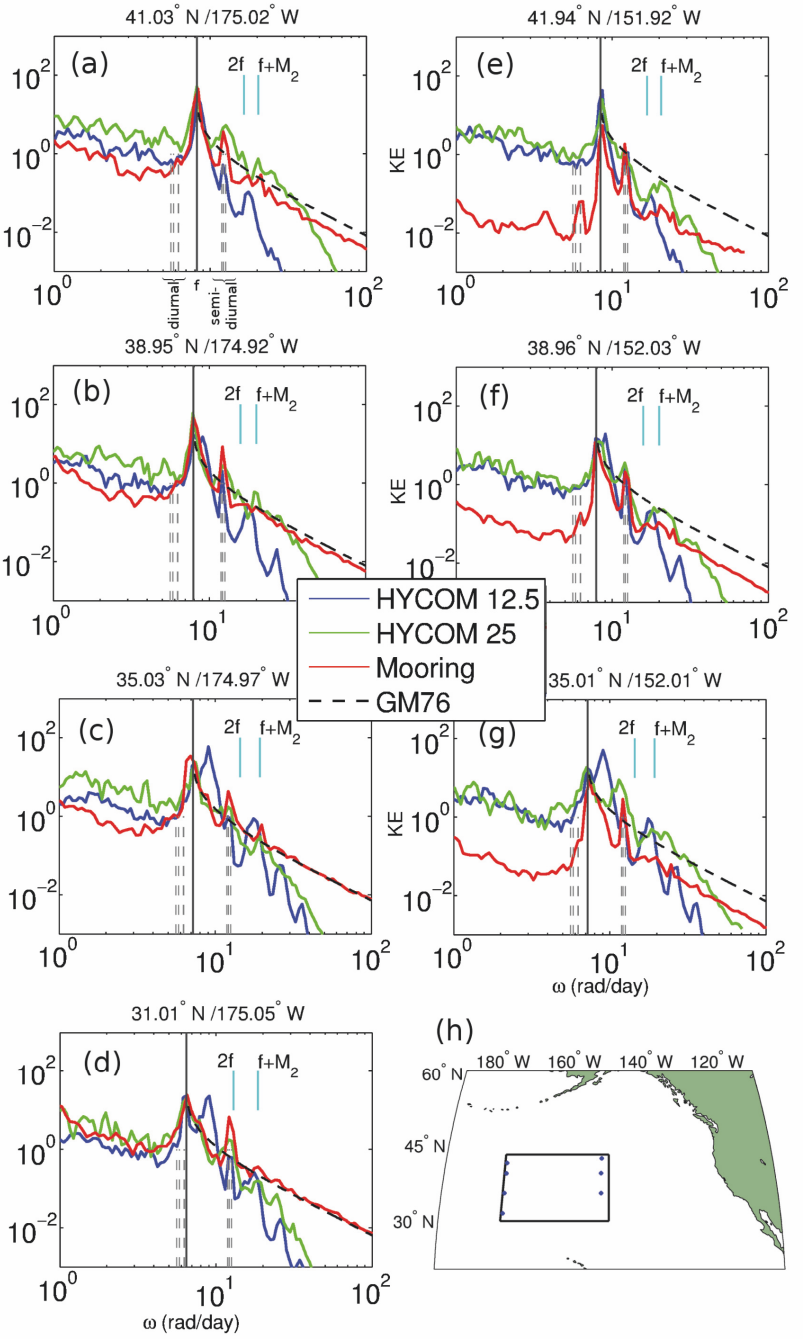

Figure 13.25. (a)-(g) Frequency spectra $E(\omega)$ of surface kinetic energy [(m/s)^2 / (rad/day)] from moored current meter observations (red), 1/12.5° HYCOM (HYCOM12; blue), and 1/25° HYCOM (HYCOM25; green) and the model spectrum of GM76 (dashed black; Cairns and Williams, 1976; built upon Garrett and Munk, 1975). Solid black and cyan vertical lines are drawn at the frequencies f, $2f$, and $f + M_2$, while dashed vertical lines are drawn at the frequencies of the four semidiurnal (M_2, S_2, N_2, and K_2) and four diurnal (K_1, O_1, P_1, and Q_1) tidal frequencies forced in the model. (h) The analysis region, showing the locations of the seven moorings in (a)-(g), in the northeast Pacific. The blue stars denote the locations of moored observations used in (a)-(g). Reproduced from Figure 1 of Müller et al. (2015),. ©American Geophysical Union, Wiley Online Library, used with permission.

Fig. 13.26 compares frequency spectra of dynamic height variance in global 1/25° HYCOM and 1/48° MITgcm vs. 9 McLane profilers. The broadband low-frequency continuum, semidiurnal peaks, and the IGW supertidal continuum are visible in all 9 subplots of Fig. 13.26. Diurnal peaks are visible in some of the subplots. The HYCOM and MITgcm spectra are similar in the subtidal and tidal bands. In the 0.2-1 cpd band, both HYCOM and MITgcm are generally deficient relative to observations, for reasons we do not understand. The supertidal IGW continuum is generally captured better by the MITgcm simulations, due to their higher horizontal and vertical resolution.

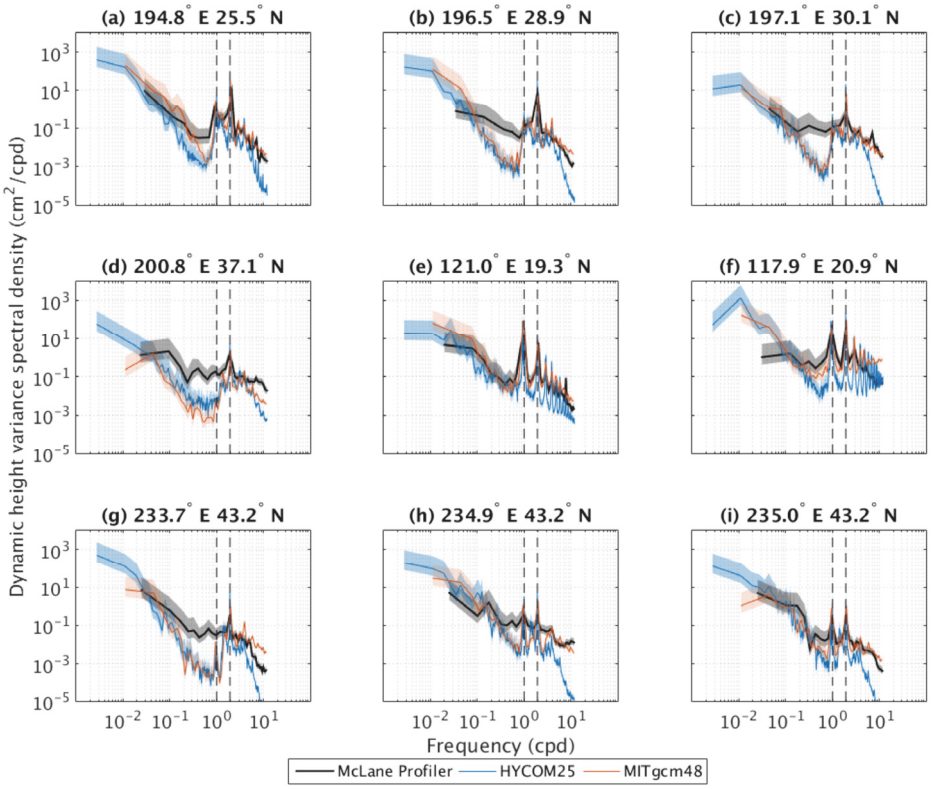

Figure 13.26. Dynamic height variance frequency spectra from McLane profilers and nearest neighbor gridpoints extracted from global simulations of 1/25° HYCOM (HYCOM25) and 1/48° MITgcm (MITgcm48). The dashed vertical lines denote K_1 diurnal and M_2 semidiurnal tidal frequencies. The shaded regions are the 95% confidence intervals that account only for random error in spectral density calculations. Reproduced from Figure 3 of Savage et al. (2017b), ©American Geophysical Union, Wiley Online Library, used with permission.

Comparison with linear internal gravity wave theory

In this section, we compute and display $K - \omega$ (horizontal wavenumber-frequency) spectra of surface kinetic energy and SSH variance, and examine whether the spectra follow the predicted linear IGW dispersion curves. Fig. 13.27 displays $K - \omega$ spectra of HYCOM surface kinetic energy computed over the North Pacific box shown in Fig. 13.25h. Dispersion relations for the first 3 vertical modes, computed from the Sturm-Liouville problem (see appendix) applied to model output, are drawn on the figure. Because both f and N change over the model gridpoints contained

in the box, we computed the eigenspeeds at all model gridpoints along the southern and northern boundaries of the box, and we used the extreme values along each boundary to draw the dispersion curves—thus explaining why each of the 3 vertical modes is associated with two curves rather than just one. Near-inertial and semidiurnal peaks are clearly visible in spectra computed from both the 1/12.5° and 1/25° solutions. The kinetic energy increases with increasing resolution, especially along the vertical mode-1 and mode-2 dispersion curves. The bottom inset plots in Fig. 13.27 display the frequency spectra computed over all wavenumbers. The inset frequency spectra reveal sharp semidiurnal tidal peaks and a near-inertial peak that is broadened due to the range of latitudes represented in the box. The right-hand-side inset plots display the wavenumber spectra integrated over frequencies larger than the inertial frequency f_{29N} at 29°N. The wavenumber spectra show a peak associated with the first mode semidiurnal tide.

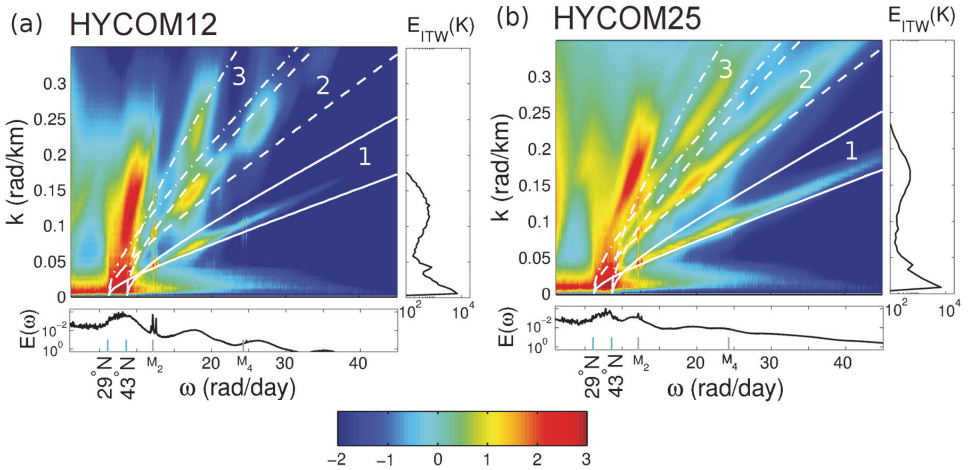

Figure 13.27. The $K-\omega$ spectra of kinetic energy $E(K, \omega)$, with units $(m/s)^2$ / [(rad/day) (rad/km)] on a log_{10} scale, for (a) HYCOM12 and (b) HYCOM25. The white curves represent bounding linear dispersion relations of the first three internal wave vertical modes (solid = mode 1; dashed = mode 2; and dash dotted = mode 3). The spectra $E(\omega)$ integrated over all horizontal wave numbers K, and $E_{ITW}(K)$ integrated over frequencies larger than the inertial frequency at 29°N ($\omega \geq f_{29N}$), are shown as bottom and right-hand-side insets, respectively. In the $E(\omega)$ spectra, cyan lines indicate the inertial frequencies at the bounding latitudes 29°N and 43°N, while M_2 and M_4 frequencies are also indicated. Reproduced from Figure 2 of Müller et al. (2015), ©American Geophysical Union, Wiley Online Library, used with permission.

The $K-\omega$ spectra of SSH variance in the North Pacific, in both HYCOM and MITgcm simulations, is displayed in Fig. 13.28. As with the IGW kinetic energy spectra, the SSH variance tends to lie along linear dispersion curves, and tends to increase with increasing horizontal resolution. Figure 5 in Savage et al. (2017b), and the supplementary figures in that paper, show that similar behaviors are seen over many different geographical regions; thus, the North Pacific region is not "special". In the higher-resolution simulations, the spectra fold back after reaching the Nyquist frequency of 12 cpd (associated with a 2 hour period). This folding in the spectra of the highest-resolution models is due to aliasing of energy in motions having sub-hourly periods. It is interesting that some global models now have so much high-frequency energy that aliasing problems arise with hourly snapshots.

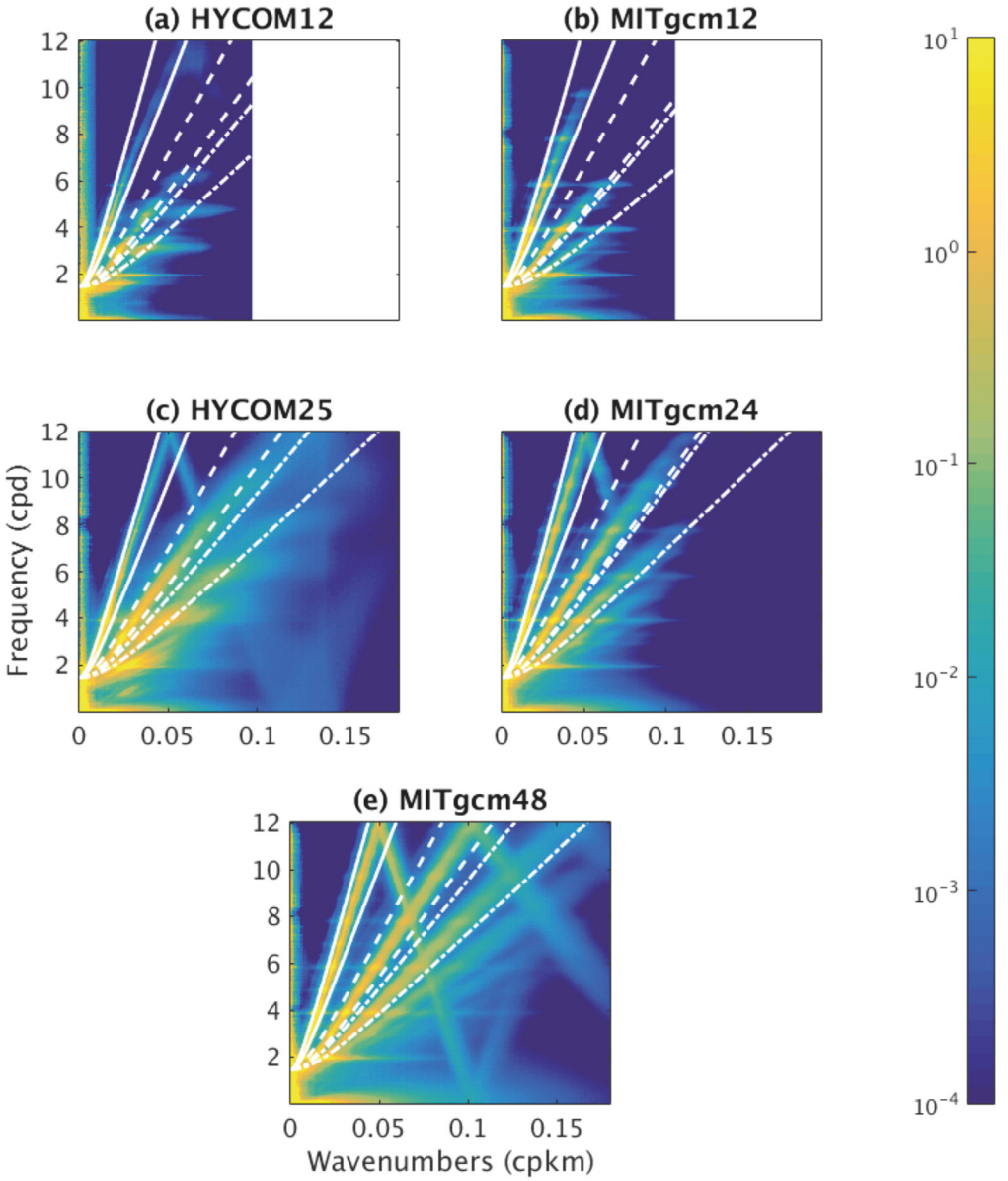

Figure 13.28. Sea surface height variance frequency-horizontal wave number spectra, in (cm^2/[(cpd cpkm)], computed in North Pacific region from HYCOM12, HYCOM25, MITgcm12, MITgcm24, and MITgcm48. Wave number axes are the same in each plot, and are set to the maximum wave number for the HYCOM25 calculation. White curves show theoretical IGW linear dispersion relations for first (solid), second (dashed), and third (dashed-dotted) vertical modes. Bounding curves for each vertical mode are computed from the maximal and minimal eigenspeeds along the northern and southern boundaries, as in Müller et al. (2015). Reproduced from Figure 6 of Savage et al. (2017b), ©American Geophysical Union, Wiley Online Library, used with permission.

Impact of Wave Drag on Tide Model Energetics and Accuracy

This section addresses the impact of parameterized topographic wave drag on tide model energetics and accuracy. Many studies have shown that inclusion of a parameterized topographic wave drag improves the accuracy of forward (unconstrained) barotropic tide models. Arbic et al. (2004) explored the reasons for this. Fig. 13.29A displays the globally integrated, temporally averaged M_2 barotropic kinetic and available potential energy, in a global barotropic tide model, as a function of wave drag strength, which is controlled with a multiplicative factor (see Arbic et al., 2004 for more explanation). Fig. 13.29B displays the globally averaged discrepancy D, defined in equation (13), of the model against the highly accurate altimeter-based barotropic tide model GOT99 (Schrama et al., 1994; Ray, 1999). When the available potential energy is either too large or too small relative to the value obtained from accurate altimeter-based values (extra horizontal line in Fig. 13.29a), the elevation error is relatively large. The minimum in the elevation error occurs when the modeled available potential energy is close to the observed value. Thus, because the wave drag strength controls tidal energy levels in models, it controls how close they lie to observations.

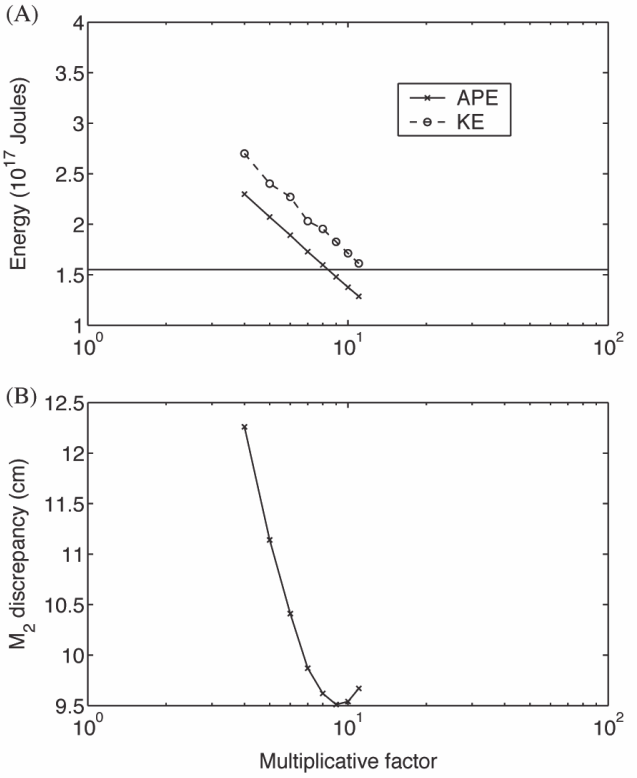

Figure 13.29. (A) Globally integrated, temporally averaged available potential energy (APE) and kinetic energy (KE) in 1/2° one-layer M_2-only simulations with a scalar approximation for the SAL term, run with a topographic wave drag scheme augmented by a variable multiplicative factor. The extra horizontal line represents the observed value of APE, taken from Tierney et al. (2000b). (B) Time- and area-averaged sea-level discrepancy D against GOT99.2, in waters deeper than 1000 m and equatorward of 66°. Reproduced from Figure 4 of Arbic et al. (2004).

The HYCOM tidal energy budget was thoroughly examined in Buijsman et al. (2016). Fig. 13.30 displays the energy dissipation of barotropic and baroclinic semidiurnal tidal flows by topographic wave drag and bottom drag. As expected, wave drag dissipates considerable energy over topographic features such as the mid-Atlantic ridge, while bottom drag dissipates considerable energy in coastal areas where tidal velocities are large. Buijsman et al. (2016) reported on a numerical instability in HYCOM, occurring in a region of the North Pacific. This instability is visible in high-frequency animations of HYCOM output, and can be seen in Fig. 13.30d (see anomalous patch just south of the Aleutians) as well as in other figures in Buijsman et al. (2016). Buijsman et al. (2016) noted that the instability is probably a thermobaric instability (Sun et al., 1999; Hallberg, 2005; Adcroft et al., 2008), a class of instability that manifests itself in weakly stratified regions of isopycnal models. Buijsman et al. (2016) found that the instability is confined to the North Pacific, and accounts for less than 2% of the globally integrated low-mode conversion. In the summary section we will briefly discuss ongoing efforts to eliminate this instability in HYCOM.

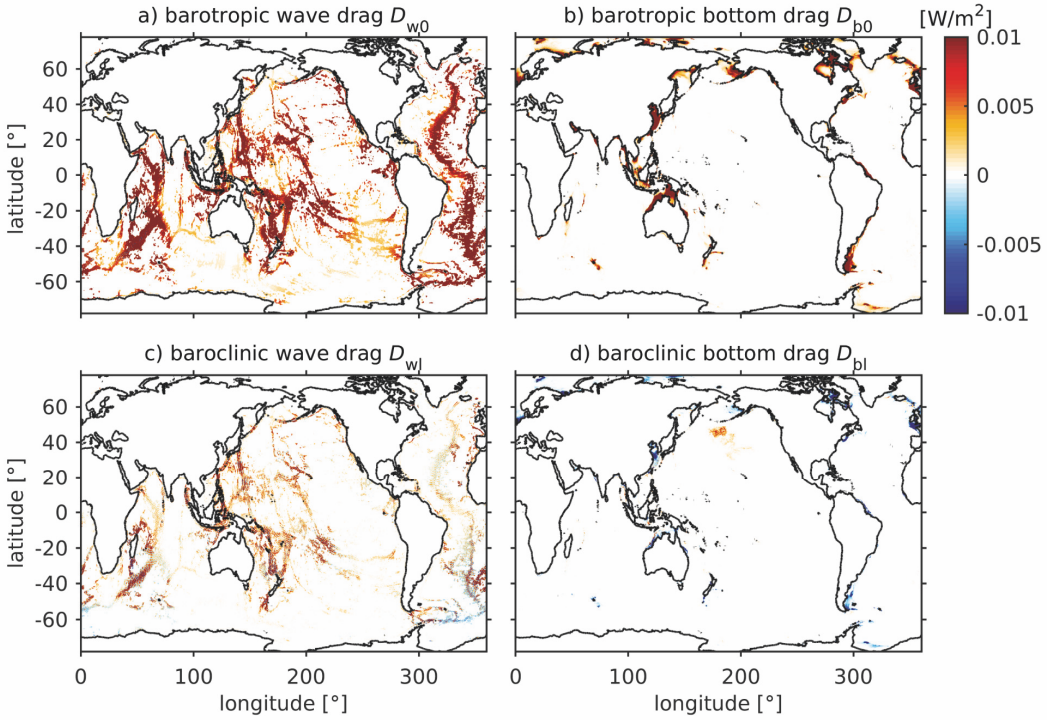

Figure 13.30. Semidiurnal barotropic dissipation due to (a) linear topographic wave drag and (b) bottom drag. Baroclinic dissipation due to (c) linear topographic wave drag and (d) bottom drag. Reproduced from Figure 2 of Buijsman et al. (2016), ©American Meteorological Society, used with permission.

The impact of the topographic wave drag on the HYCOM-altimetry internal tide comparison was comprehensively explored in Ansong et al. (2015). Fig. 13.31 displays maps of the M_2 internal tide in along-track altimetry (a), and in HYCOM simulations with varying strengths of wave drag (b-f). The HYCOM amplitudes are too large in simulations with wave drag applied only to the barotropic flow (d) and in simulations with no wave drag at all (e,f). In (f), we increased the

quadratic bottom drag coefficient by a factor of about 100 along the continental shelves, as a test of the hypothesis that internal tides are dissipated primarily along shelves. However, the differences between open-ocean internal tide amplitudes in (f) and those in (e) are small. The internal tide amplitudes in simulations with wave drag acting on bottom flows (hence, on both barotropic and baroclinic motions)—the default setup in our HYCOM "wind plus tides" simulations—lie closer to altimeter observations, especially when the wave drag is strong; compare (c; stronger drag) and (b; weaker drag) to (a; observations). It should be noted that because the model contains mesoscale eddies, the internal tides in the model are scattered and become non-stationary just as internal tides are in the ocean. Thus, the model-observational discrepancies in Fig. 13.31 are not due to the lack of scattering into nonstationarity by mesoscale eddy-tide interactions in the model. Ansong et al. (2015) thus provides indirect evidence for substantial damping of low-mode internal tides in the open ocean; the damping is needed to obtain agreement with altimetry. For our current HYCOM simulations, we assume that low-mode damping is primarily due to production of high-mode internal tides over topography. The high modes break and dissipate energy in the ocean, but are not resolved in our global models. We parameterize the production and breaking of high vertical modes with topographic wave drag acting on the bottom flow. In the actual ocean, as discussed in Ansong et al. (2015) and shown schematically in Fig. 13.2, there are likely to be other damping mechanisms, which need to be better parameterized in future models in order to see continued improvements in modeled internal tides.

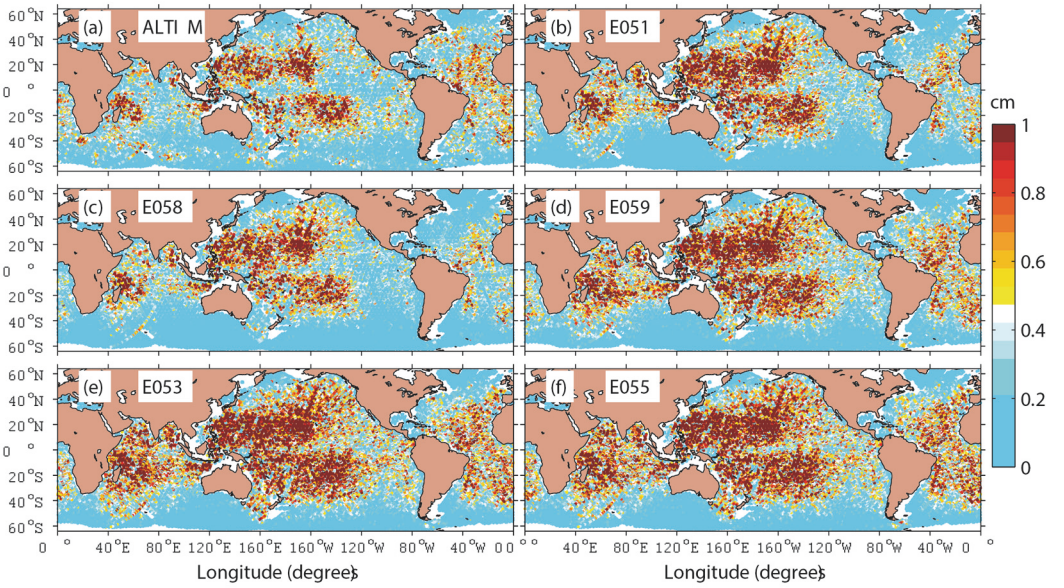

Figure 13.31. Amplitude (cm) of stationary M_2 internal tide in (a) along-track altimeter-based analyses, and in HYCOM simulations (b) E051; with wave drag (scale factor = 0.5) applied to the bottom flow, (c) E058; with wave drag (scale factor = 1.0) applied to the bottom flow, (d) E059; with wave drag (scale factor = 1.0) applied to only the barotropic flow, (e) E053; without wave drag, (f) E055; without wave drag but with the quadratic bottom drag coefficient increased by a factor of about 100 along the continental shelves. The amplitudes of the HYCOM simulations are computed from 3 months of SSH output. Reproduced from Figure 5 of Ansong et al. (2015), which can be consulted for more details of the E051-E059 simulations, ©American Geophysical Union, Wiley Online Library, used with permission.

Fig. 13.32 displays the globally averaged stationary M_2 internal tide amplitude in the HYCOM simulations with varying topographic wave drag, vs. altimetry. Again it is clear that model-altimetry agreement is better with some wave drag in the model. We point out again that HYCOM is currently the only "wave plus tides" model that employs a wave drag. Fig. 13.32 also makes clear that the record duration matters for the model-altimeter comparison. The amplitude of the modeled stationary internal tide decreases as the model record duration increases. (The altimeter analysis is based on a long—multi-year—record). The importance of record duration in the estimation of tidal quantities is seen in other studies. Nash et al. (2012), for example, finds that the amplitude of stationary tidal currents estimated from a current meter reduces as the analysis period is increased. This discussion of stationarity leads naturally into the next section, which is on non-stationary internal tides.

Internal Tide Nonstationarity

In this section, the focus turns to internal tide nonstationarity. Non-stationary internal tides are of particular interest for the SWOT mission, because it will be necessary to remove non-stationary internal tides from SWOT data in order to study other oceanic motions of interest such as mesoscale and submesoscale eddies. The HYCOM simulations discussed in this chapter have been used in a number of studies of internal tide nonstationarity. Shriver et al. (2014) computed the standard deviation of internal tide SSH signals obtained from 18 different 183-day windows, and from 60 different 30-day windows. A general finding of Shriver et al. (2014) is that the normalized internal tide variability—the standard deviation divided by the mean internal tide signal—is relatively small near internal tide generation sites and grows larger as the distance from the generation sites increases. Similar conclusions were drawn in Ansong et al. (2017)'s examination of the nonstationarity of semidiurnal internal tide energy fluxes in HYCOM vs. mooring observations. A basin-scale map, centered on the equatorial Pacific, of total and non-stationary[15] semidiurnal internal tide energy fluxes in HYCOM is shown in Fig. 13.33. While the stationary fluxes emanating from the French Polynesian Islands do not pass through the equator, the total fluxes do. Buijsman et al. (2017) shows that the internal tide nonstationarity in the equatorial Pacific is due to the scattering effects of the system of strong jets on the equator. This is consistent with the picture painted by Ponte and Klein (2015), who explored the scattering of a stationary internal tide by a strong jet in an idealized model of mid-latitude eddy-internal tide interactions. Buijsman's results suggest that the "dead zone" seen in altimeter estimates of the stationary internal tide in the equatorial Pacific may be due to internal tide nonstationarity rather than to dissipation.

The non-stationary internal tide SSH field in HYCOM has also been quantified through frequency spectra. Savage et al. (2017a) computed frequency spectra, from both steric and non-steric SSH fields, at subsampled grid points (taken every 1/4°) from one year of hourly 1/25° HYCOM output, and then computed band-integrated variance over subtidal, semidiurnal, diurnal,

[15] Note that Buijsman et al. (2017) primarily used the terms "incoherent" and "coherent" rather than "non-stationary" and "stationary".

and supertidal bands (Table 13.2). In the semidiurnal and diurnal bands, the steric SSH variance—dominated in these bands by internal tides—is computed both before and after removal of the stationary internal tides. The variance remaining after removal of the stationary internal tides is taken to be the non-stationary internal tide signal. Fig. 13.34 displays the global map of non-stationary semidiurnal internal tide SSH variance in HYCOM simulations, determined by Savage et al. (2017a) from the method described above. The largest non-stationary internal tide signals are seen at the equator, consistent with the results in Buijsman et al. (2017). The equator is also a "hotspot" in global maps of non-stationary internal tides made from altimeter observations in Zaron (2017). Zaron's maps of non-stationary internal tides are made from a method somewhat similar to the Savage et al. (2017a) method described above, except that Zaron employed wavenumber rather than frequency spectra. It is encouraging that different analysis methods applied to different outputs (altimetry vs. model output) yield qualitatively similar findings. A comprehensive comparison of non-stationarity in HYCOM vs. altimetry is currently underway (Nelson et al., paper in preparation).

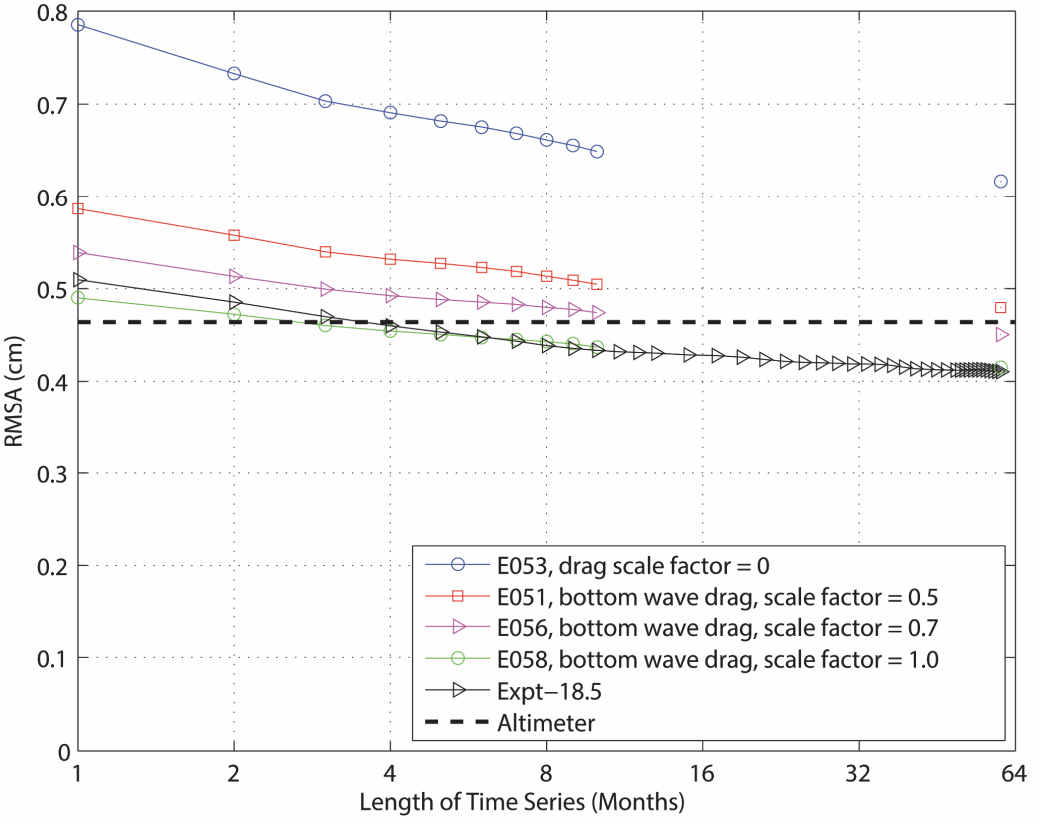

Figure 13.32. Globally averaged root-mean-square amplitude (RMSA) of stationary HYCOM baroclinic M_2 tidal elevations and along-track altimeter value. The HYCOM results are dependent on drag strength (see legend) as well as on the length of the time series used. The x-axis is a base 2 log scale. Expt-18.5 is an older HYCOM experiment about which several papers have been written (e.g., Shriver et al., 2012) and from which 5 year-long SSH output was stored. The 60-month amplitudes shown for the newer simulations are rough estimates based on the changes seen over 60 months in Expt-18.5 with record length. Reproduced from Figure 8 of Ansong et al. (2015), which can be consulted for more details of the E051-E059 simulations, ©American Geophysical Union, Wiley Online Library, used with permission.

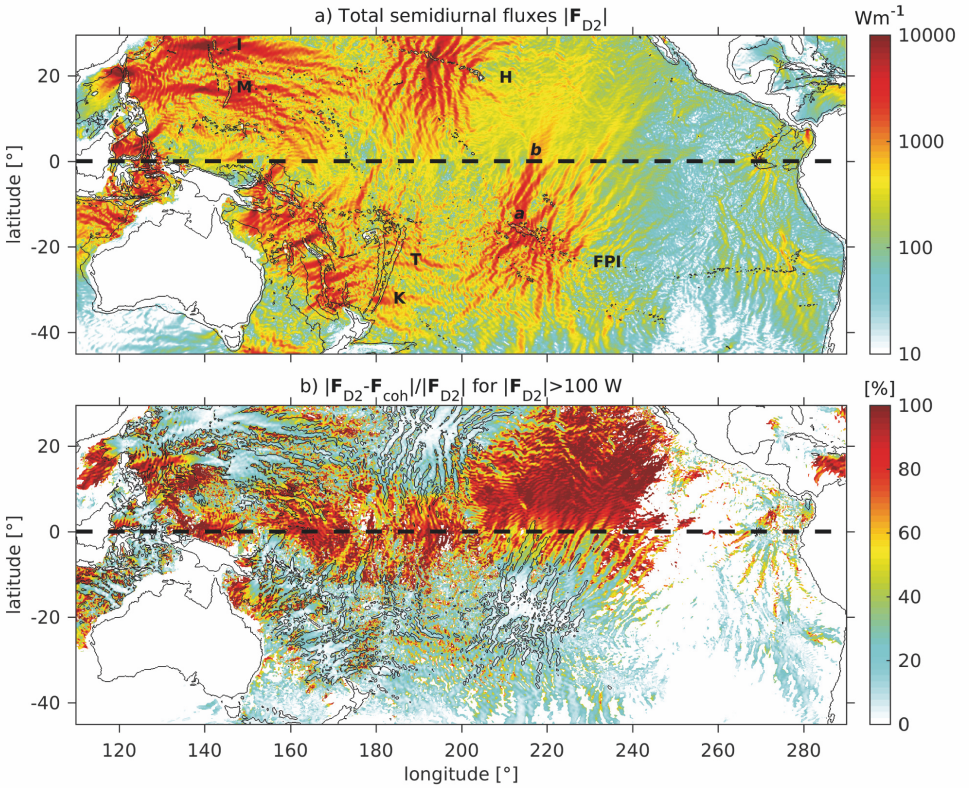

Figure 13.33. (a) The magnitude of the annual-mean semidiurnal band-passed energy fluxes $|F_{D2}|$ in the equatorial Pacific from HYCOM. Bathymetry is contoured at 0 and -2000 m. Hawai'i is abbreviated with H, the French Polynesian Islands with FPI, Tonga with T, the Kermadec Islands with K, the Izu Ogasawara Ridge with I, and the Mariana Islands with M. Spectral properties are computed in Buijsman et al. (2017) along the internal tide beam marked by a-b. (b) The percentage of the sum of the annual-mean incoherent (non-stationary) and cross-term fluxes to the band-passed fluxes. Values coinciding with $|F_{D2}| < 100$ W m^{-1} are not shown. The black contours mark 1000 W m^{-1} values in the band-passed fluxes. Bathymetry is contoured at 0 m. In both subplots, the equator is marked by the dashed black line. Reproduced from Figure 2 of Buijsman et al. (2017), ©American Geophysical Union, Wiley Online Library, used with permission.

Band	Frequencies (cpd)
Subtidal	(1/366)–0.86
Diurnal	0.87–1.05
Semidiurnal	1.86–2.05
Supertidal	2.06–12

Table 13.2. Definitions of frequency bands employed in Savage et al. (2017a).

Nonlinearities and the Internal Gravity Wave Continuum

In this section, we provide a first look at the role of nonlinearities in developing the IGW continuum. We employ a spectral kinetic energy transfer diagnostic in $K-\omega$ space, motivated by wavenumber-domain spectral transfers which have long been used to diagnose energy exchanges between length scales. For example, Scott and Wang (2005), Scott and Arbic (2007), Arbic et al. (2013), and references therein, can be consulted for discussions on using wavenumber-domain spectral transfers and fluxes (the latter being integrals of the transfers) to diagnose inverse and forward cascades of geostrophic flows in the wavenumber domain. Arbic et al. (2012b) and Arbic et al. (2014) describe extending the spectral kinetic energy transfer diagnostic to the frequency and frequency-wavenumber domains, respectively. All of the references mentioned above focus on geostrophic flows and on flows in the ocean. Shang and Hayashi (1990a,b) can be consulted for an earlier description of spectral kinetic energy transfers in frequency space, with application to flows in atmospheric models. Müller et al. (2015) applied a spectral transfer diagnostic in the wavenumber-frequency domain to total (geostrophic plus non-geostrophic) flows in the "wind plus tides" HYCOM simulations. The diagnostic is developed by multiplying Fourier transformed terms in the momentum equation by the Fourier transform of the velocity. If one writes the shallow-water momentum equation as

$$\frac{\partial \vec{u}}{\partial t} = -\vec{u} \bullet \nabla \vec{u} + OT, \tag{18}$$

where *OT* denotes "other terms", then multiplication by $\vec{u}\bullet$ results in a kinetic energy equation of the form

$$\frac{\partial \frac{1}{2}|\vec{u}|^2}{\partial t} = -\vec{u} \bullet [\vec{u} \bullet \nabla \vec{u}] + \vec{u} \bullet OT. \tag{19}$$

If we instead Fourier transform the terms in equation (18) and then multiply by the Fourier transform of u, we obtain

$$\frac{\partial \hat{KE}}{\partial t} = -\widehat{\vec{u}} \bullet \widehat{[\vec{u} \bullet \nabla \vec{u}]} + \widehat{\vec{u}} \bullet \widehat{OT}, \tag{20}$$

where *KE* denotes kinetic energy, $\hat{A}$ denotes the Fourier transform of A, and the spectral kinetic energy transfer T_{KE} due to nonlinear advection is given by

$$T_{KE} = -\widehat{\vec{u}} \bullet \widehat{[\vec{u} \bullet \nabla \vec{u}]}. \tag{21}$$

The Fourier transform can be in the wavenumber, frequency, or wavenumber-frequency domains. Fig. 13.35 displays the results of this diagnostic applied in the wavenumber-frequency domain to the 1/12.5° and 1/25° HYCOM "wind plus tides" simulations in Müller et al. (2015). Fig. 13.36 displays the spectral kinetic energy transfers in 1/25° HYCOM as replotted in Savage et al. (2017a) with a nonlinear color bar, which makes some key features easier to see. The transfers shown in Figs. 13.35 and 13.36 reveal extraction of kinetic energy (blue colors; negative values of transfer) from near-inertial flows and semidiurnal tides, and deposition of energy (red colors; positive values of transfer) along the vertical mode-1 IGW continuum, all consistent with the

classical paradigm of the formation of the IGW continuum spectrum. The spectral kinetic energy transfers become more vigorous when the model resolution increases from 1/12.5° to 1/25°, meaning that, as is also seen in the spectrum, the model has not yet achieved numerical convergence with respect to the IGW continuum. The "patchy" structure of spectra and spectral transfers was examined in Müller et al. (2015); see Figure 4 and related discussions in that paper.

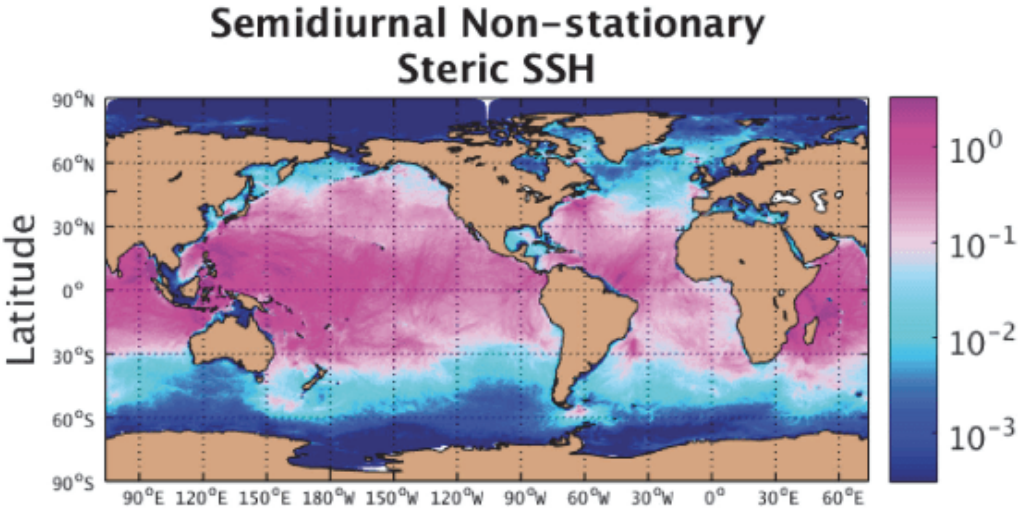

Figure 13.34. Global steric SSH variance (cm^2) from HYCOM25 in the semidiurnal band (frequencies 1.86–2.05 cpd) after stationary internal tides have been removed via harmonic analysis. Reproduced from Figure 15 of Savage et al. (2017a), ©American Geophysical Union, Wiley Online Library, used with permission.

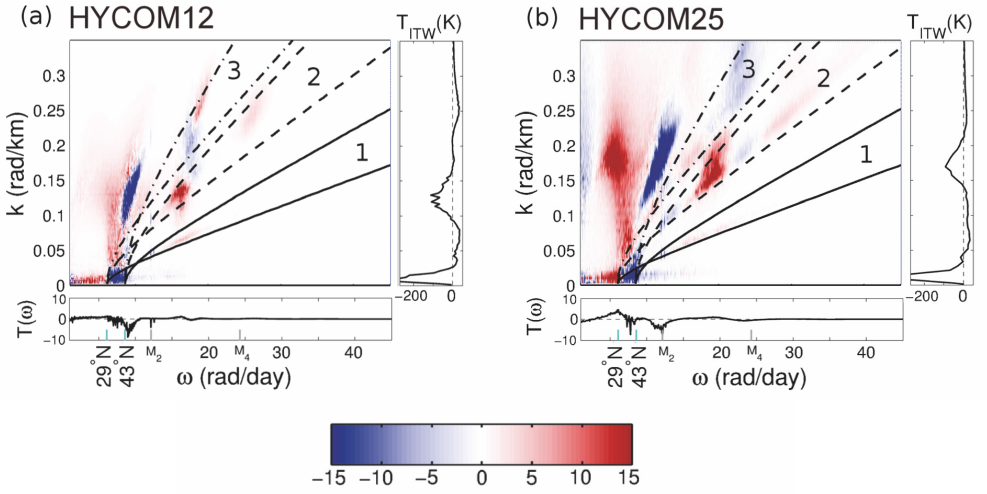

Figure 13.35. As in Fig. 13.27 but for nonlinear spectral kinetic energy transfer $T_{KE}(K, \omega)$, with units (10^{-9} W/kg)/[(rad/day)(rad/km)]. The colorbar is linear, and the dispersion curves and mode band numbers are shown in black. Energy is taken out of the blue regions (for instance, low-mode near-inertial and semidiurnal internal tidal motions) and added to the red regions (for instance, higher-frequency and higher-wave number internal waves). Reproduced from Figure 3 of Müller et al. (2015), ©American Geophysical Union, Wiley Online Library, used with permission.

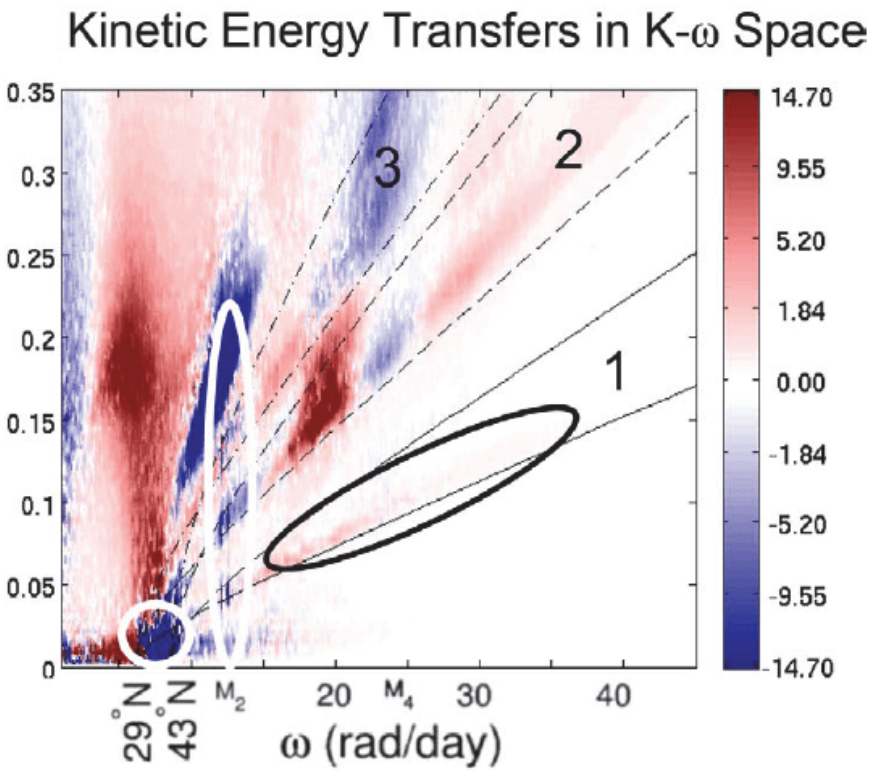

Figure 13.36. Nonlinear spectral kinetic energy transfer $T_{KE}(K, \omega)$, with units (10^{-9} W/kg)/[(rad/day)(rad/km)], computed in Müller et al. (2015) and replotted with a nonlinear color bar to emphasize some of the key features described in Fig. 13.35. Reproduced from Figure 1 of Savage et al. (2017a), ©American Geophysical Union, Wiley Online Library, used with permission.

Applications to Swath Satellite Altimetry

Next we explore more applications of global internal tide and IGW continuum models for swath satellite altimetry missions such as the SWOT mission. The SWOT swath altimeter will measure SSH in two dimensions. SWOT will measure the SSH signature of internal tides and the IGW continuum spectrum, albeit in a temporally aliased manner, and is expected to improve the mapping of these high-frequency motions. At the same time, such motions will have to be accurately subtracted out from SWOT data in order for other oceanic motions, such as mesoscale and submesoscale eddies, to be examined. Stationary internal tides, non-stationary internal tides, and the IGW continuum spectrum all contribute to SSH variance, and the latter two classes of motions will be especially challenging to predict. Savage et al. (2017a) developed global maps of the steric and non-steric SSH variance integrated over subtidal, diurnal, semidiurnal, and supertidal bands. The division of motions into steric and non-steric components, and into different frequency bands, helps to separate different dynamical regimes. For instance, the subtidal steric SSH variance is dominated by mesoscale currents and eddies. Fig. 13.37 shows the relative sizes of non-steric and steric components, and of total SSH variance, in the different frequency bands employed in Savage et al. (2017a). A few general tendencies are easily seen. The largest signals in the total and non-

steric SSH are the semidiurnal and diurnal tides, followed by subtidal motions. The largest signals in the steric SSH are subtidal signals, followed by semidiurnal and diurnal tides. The fraction of semidiurnal and diurnal SSH variance that is non-stationary is significantly larger for steric signals than for non-steric signals. The supertidal steric SSH variance, dominated by the IGW continuum spectrum, is greatly enhanced with increased resolution, meaning that numerical convergence for this class of motions has not yet been achieved. This in turn implies that the steric supertidal SSH variance seen in Fig. 13.37 is likely be a lower bound on the actual value.

Fig. 13.38 displays the global map of supertidal steric SSH variance in 1/25° HYCOM, as computed in Savage et al. (2017a). To our knowledge, this is the first global map made of the IGW SSH signal. The IGW SSH signal is generally larger in the tropics than in higher latitudes, with the mid-to-high latitude North Pacific being a notable exception, and is generally larger in the Pacific and Indian Oceans than in the Atlantic. Although the models are not yet accurate enough to operationally remove such signals, we believe that simply mapping the signals as we have done here represents an important first step in understanding the challenges and opportunities that internal tides and the IGW continuum present for the SWOT mission.

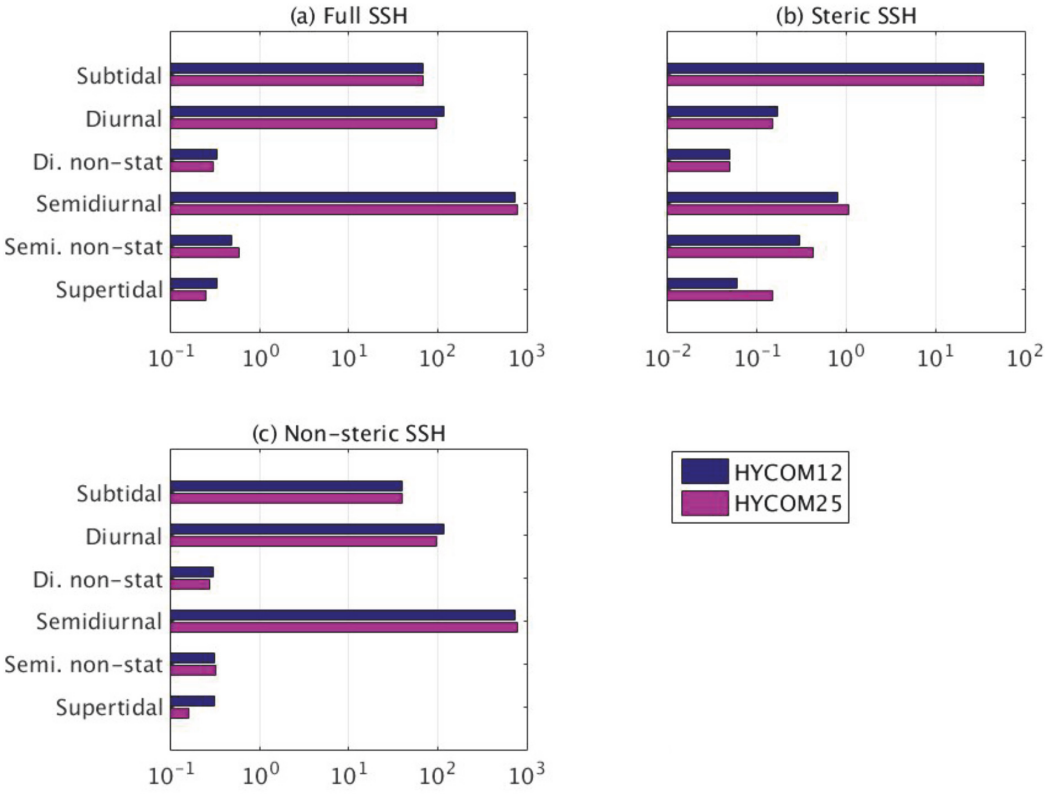

Figure 13.37. Bar graph of spatially averaged HYCOM12 and HYCOM25 variance in cm^2 in subtidal, diurnal, non-stationary diurnal, semidiurnal, non-stationary semidiurnal, and supertidal bands in (a) full, (b) steric, and (c) non-steric SSH. Variance was averaged over deep ocean grid points (seafloor depths greater than 1000 m). Axis limits differ between subplots. Reproduced from Figure 10 of Savage et al. (2017a), ©American Geophysical Union, Wiley Online Library, used with permission.

Of central interest for the SWOT mission is the SSH wavenumber spectrum. Indeed, the NASA mission requirements for SWOT are written in terms of the wavenumber spectrum (Fu et al., 2012). As discussed in Richman et al. (2012; see also references therein), the slopes of the SSH wavenumber spectrum differ according to the dominant underlying dynamics. The IGW continuum is expected to have a spectrum that falls off as K^{-2}, while "interior quasi-geostrophy" and "surface quasi-geostrophy" are expected to have spectra that are proportional to K^{-5} and $K^{-11/3}$, respectively. The slope of the SSH wavenumber spectrum therefore represents a test of whether the underlying dynamics are dominated by IGWs, "interior quasi-geostrophic" motions, or "surface quasi-geostrophic" motions. Fig. 13.39 displays the slope of the SSH wavenumber spectrum, over the 70-250 km wavelength mesoscale band defined by Xu and Fu (2012), from total and low-passed HYCOM SSH model output. The map made from total SSH, which includes high-frequency motions such as internal tides and the IGW continuum, shows flatter slopes in regions where strong IGWs can overwhelm the signals from lower-frequency motions such as mesoscale eddies.

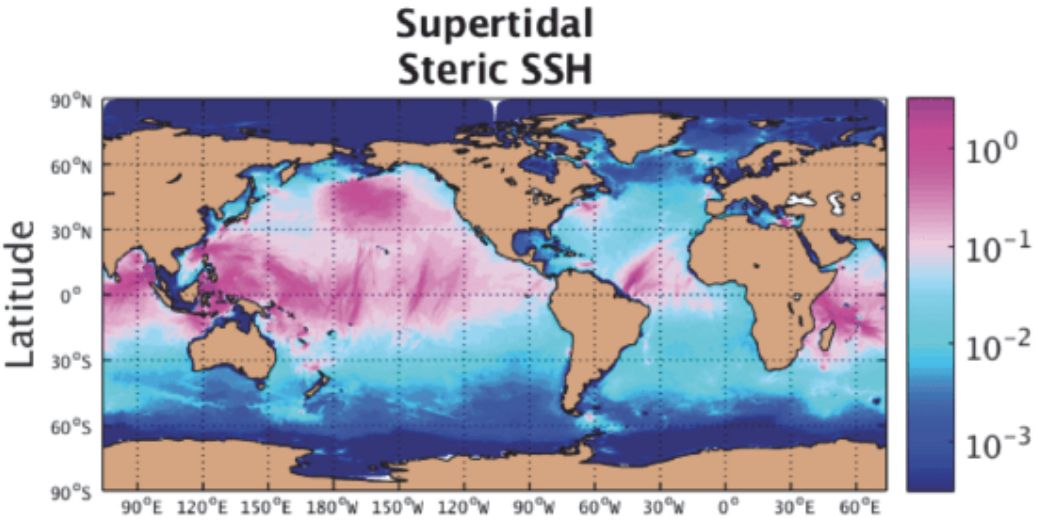

Figure 13.38. Global steric SSH variance (cm^2) from HYCOM25 in the supertidal band (frequencies 2.06–12 cpd). Reproduced from Figure 16 of Savage et al. (2017a), ©American Geophysical Union, Wiley Online Library, used with permission.

The story laid out by Richman et al. (2012) has been further corroborated by others, for instance, Callies and Ferrari (2013), who focused on kinetic energy more than on SSH, and on along-track Acoustic Doppler Current Profiler (ADCP) data rather than model output. Rocha et al. (2016a) compared along-track wavenumber spectra in the MITgcm to spectra from ADCP data, in one Southern Ocean location. Qiu et al. (2017) also analyzed along-track ADCP data, and defined a transition length scale delineating length scales over which the wavenumber spectrum is dominated by geostrophic motions from length scales over which the wavenumber spectrum is dominated by IGWs. Rocha et al. (2016b) demonstrated that the relative strengths of low- and high-frequency motions in the MITgcm output have a seasonal cycle. Qiu et al. (2018) explored seasonal changes in the transition scale using the MITgcm simulations. Wang et al. (2018) used the MITgcm output to simulate a field campaign for in-situ calibration and validation of the SWOT SSH wavenumber

spectrum. Savage et al. (2017b) displayed SSH variance wavenumber spectra integrated over different frequency bands–subtidal, tidal, and supertidal. Fig. 13.40 shows the results from the MITgcm over several regions. The figure demonstrates that internal tides and the IGW continuum can dominate the spectra at high wavenumbers—the wavenumbers of interest for SWOT—at least in some regions. Because Richman et al. (2012) separated low- and high-frequency motions with a 2-day low-pass filter, rather than a frequency-wavenumber spectrum, and because we did not realize when writing Richman et al. (2012) that our models carried a partial IGW continuum spectrum, we attributed the high-frequency motions to internal tides only in that paper. The results in Fig. 13.40, and in Rocha et al. (2016a), make clear that the IGW continuum, as well as internal tides, contribute significantly to the wavenumber spectrum at higher wavenumbers.

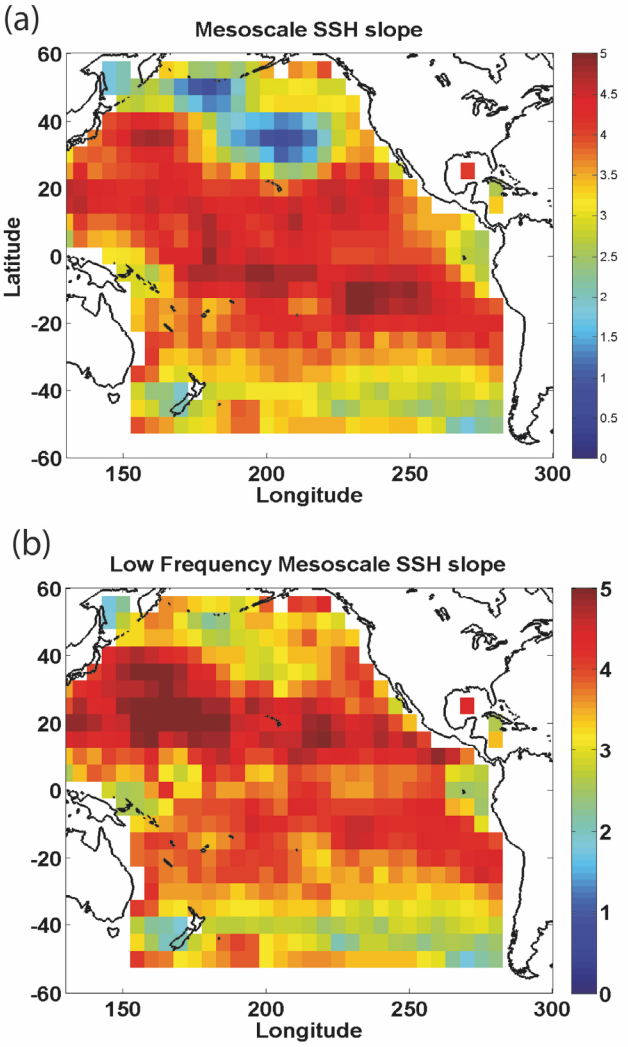

Figure 13.39. Least-squares estimate of the slope of the SSH wavenumber spectrum in the North Pacific, computed over the 70–250 km band, in HYCOM. Slopes are computed from spectra of (a) total SSH and (b) low-frequency SSH. All slopes are multiplied by -1 to make them positive. Reproduced from Figure 7 of Richman et al. (2012), ©American Geophysical Union, Wiley Online Library, used with permission.

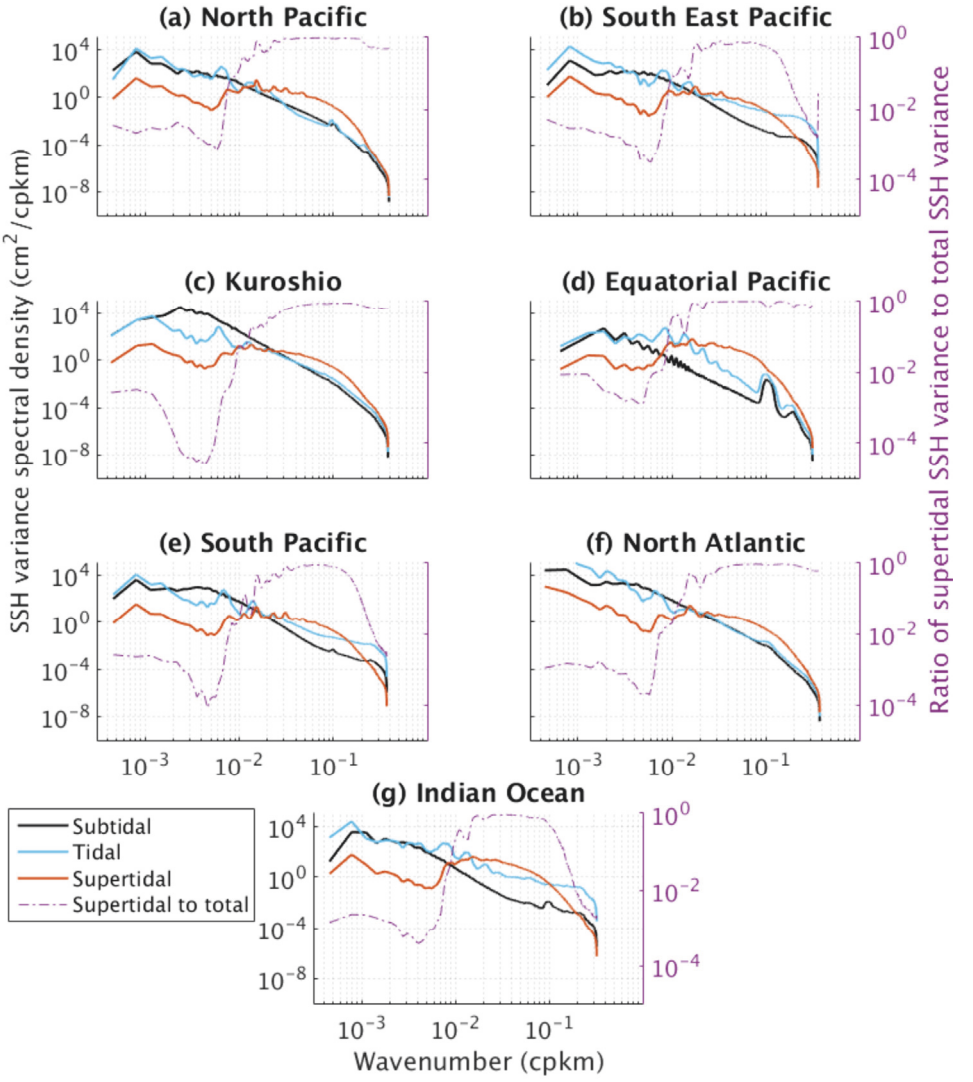

Figure 13.40. Horizontal wave number spectral density of SSH variance in seven regions in MITgcm48 [see Savage et al. (2017b) for precise locations] integrated over subtidal, tidal, and supertidal frequency bands [see Savage et al. (2017b) for definition of bands]. Right-hand axis shows ratio of supertidal to total SSH variance as a function of isotropic wave number. Reproduced from Figure 7 of Savage et al. (2017b), ©American Geophysical Union, Wiley Online Library, used with permission.

Improving Barotropic Tidal Accuracy

We continue to improve the accuracy of the barotropic tides in HYCOM. The discrepancies D of barotropic tidal elevations in the earlier HYCOM "wind plus tides" simulations are comparable to those in many other tuned forward models (e.g., Arbic et al., 2004; Egbert et al., 2004; Stammer et al., 2014; among others), but are still significantly larger than those in data-constrained tide models (e.g., Egbert et al., 1994; Ray, 1999; Lyard et al., 2006; Taguchi et al., 2014; Stammer et al., 2014; among others). Motivated by this, Ngodock et al. (2016) employed the Augmented State Ensemble

Kalman Filter (ASEnKF) technique to reduce the barotropic tidal elevation errors in HYCOM. An ensemble of perturbations to the tidal forcing was generated, with each ensemble member having horizontal length scales comparable to those in the open-ocean barotropic tides. HYCOM simulations are performed with each perturbation, and the ASEnKF machinery then selects a linear combination of the ensemble members that minimizes the barotropic tidal elevation misfits between HYCOM and TPXO. Fig. 13.41 shows the M_2 elevation errors in early HYCOM simulations, vs. HYCOM simulations with some improvements in Southern Ocean bathymetry and in iterating the SAL term, vs. HYCOM simulations that in addition employ the Ngodock et al. (2016) ASEnKF.

The ASEnKF reduces the errors throughout the globe, but large errors remain in some regions, especially in the North Atlantic. The HYCOM group is pursuing two paths for further improvements in the HYCOM barotropic tides, both based upon the fact that the North Atlantic houses three locations (the Hudson Strait, the Northwest European Shelf, and the Bay of Fundy) with large coastal tides, and the fact that such regions have been shown to have a significant back-effect upon open-ocean tides (Arbic et al., 2007, 2009; Arbic and Garrett, 2010). Because of the large back-effect, it is likely that improvement of coastal tides in key regions such as this will yield improvements in the modeled open-ocean tides. In one research path, we have developed two-way nesting in HYCOM, so that the coastal tides can be run with higher resolution, hence improving them at relatively low cost (Jeon et al., in review). In another path, we will use adjoint machinery applied to the dynamical core of TPXO to generate perturbations, for the ASEnKF machinery, that have maximum impact on the global tidal solutions. We expect that regions of large coastal tides will play a prominent role in such perturbations.

Summary of Completed Work, Ongoing Work, and Future Challenges

Completed work

To briefly summarize a large body of work, tides have been inserted into a small number of high-resolution ("eddying") global three-dimensional circulation models run by the international oceanography community, including the HYCOM simulations that are run operationally by the United States Navy, and some very-high-resolution MITgcm simulations run on NASA supercomputers. The tides in the HYCOM simulations have been compared to a number of in-situ and altimetric datasets, and a number of papers have been published. These papers have been summarized here, and the reader is referred to the original papers for more details. The HYCOM tidal simulations carry a realistic amount of internal tide nonstationarity, an important consideration for the SWOT swath altimeter mission, which will need to accurately remove both stationary and non-stationary internal tides before examination of non-tidal phenomena such as mesocale and submesoscale eddies can take place. The HYCOM simulations have also been shown to carry a partial IGW continuum spectrum, a first for global models (Müller et al., 2015). The IGW continuum spectrum is more fully developed in new simulations of the MITgcm carried out at

higher horizontal resolutions (up to 1/48°) and vertical resolutions (90 z-levels) than the 1/25°, 41-hybrid level HYCOM simulations. The HYCOM and MITgcm IGW continuum spectra have been compared to dynamic height variance spectra from McLane profilers (Savage et al., 2017b) and the MITgcm spectra have been compared to kinetic energy spectra from Acoustic Doppler Current Profilers (Rocha et al., 2016a). It seems inevitable to us that in the near future many high-resolution global ocean models will include tides, and that many researchers will be exploring the applications of such models to operational oceanography, understanding satellite altimeter observations, and achieving better understanding of mixing in the global ocean.

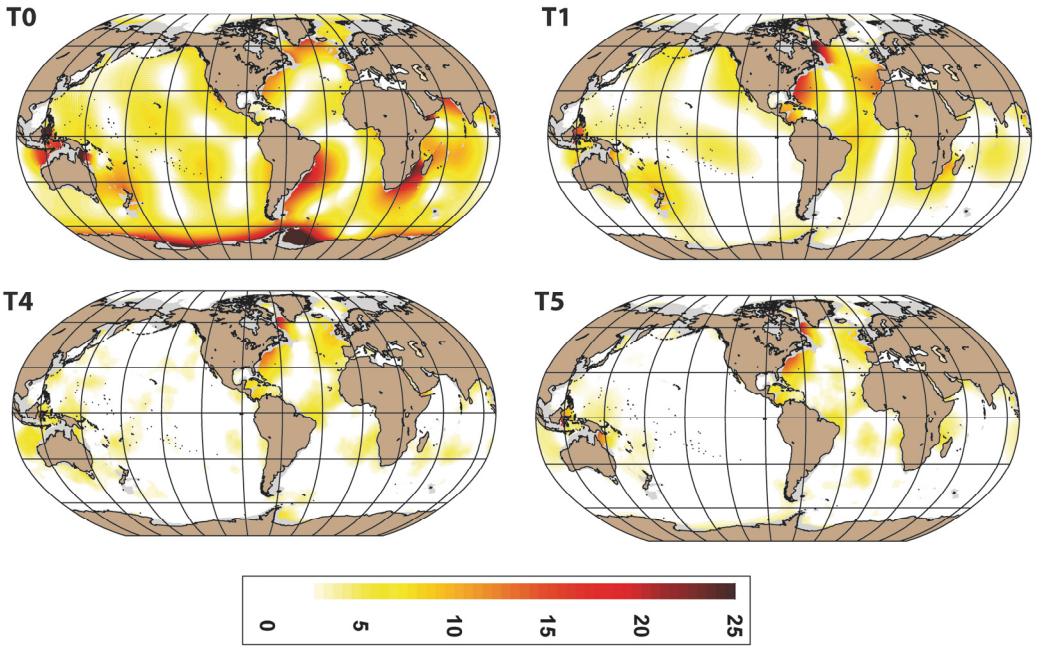

Figure 13.41. Maps of the M_2 RMS error (cm) between the HYCOM simulations and TPXO8: T0, early eight-constituent simulation with scalar SAL and Garner (2005) wave drag; T1, intermediate five-constituent simulation with bathymetry extended to include floating Antarctic ice shelves, tuned Jayne and St. Laurent (2001) wave drag, and iterated SAL; T4, ASEnKF predicted tide using a 0.5 mm constant global observation error; T5, blended ASEnKF predicted tide combining an Atlantic-only prediction with 1 cm observation error and T3 for the rest of the ocean. Reproduced from Figure 6 of Ngodock et al. (2016), which can be consulted for more details including details of the T3 simulation.

Ongoing work

In a partial list of ongoing work, we are examining tidal mixing fronts in shelves in global HYCOM (Timko et al., paper in revision), comparing non-stationary internal tides in HYCOM vs. altimetry (Nelson et al., paper in preparation), examining the IGW kinetic energy spectrum in MITgcm and HYCOM vs. McLane profilers (Ansong et al., paper in preparation), performing regional runs of the MITgcm, forced by global MITgcm at their boundaries, with even higher resolution, and comparing the vertical wavenumber spectrum of IGW kinetic energy and density variance from the regional simulations with spectra from McLane profilers (Arbic et al., paper in preparation),

computing the SSH horizontal wavenumber spectra from the same regional simulations, and comparing the IGW kinetic energy and temperature variance spectra from global HYCOM and MITgcm with spectra computed from ~3000 historical moored instruments (Luecke et al., paper in preparation).

Challenges for the future

There are many remaining challenges for global internal tide and IGW continuum models. One view of the applications of such models for satellite altimetry is that the global IGW field consists of near-inertial flows, which are an important source of energy for the IGW continuum but which do not have large SSH signals, and three different classes of IGWs that do have SSH signals. Stationary internal tides will be the easiest of these to predict, although even they represent a significant challenge for global internal tide and IGW models. Quantitative feature matching between different empirical internal tide models, and between empirical models and HYCOM, has just begun (Carrère et al., paper in preparation). Non-stationary internal tides will be more difficult to predict accurately, as such a prediction would require accurate modeling of mesoscale eddies in conjunction with accurate mapping of internal tides. Our HYCOM simulations contain an ASEnKF that improves the accuracy of modeled barotropic tides, which should improve the accuracy of the modeled internal tides, at the same time that they contain data assimilation acting on mesoscale eddies. It is possible that accurate internal tide modeling in conjunction with accurate placement of mesoscale eddies will allow prediction of non-stationary internal tides. It remains to be seen whether this challenge can be met in time for the SWOT mission. The technical challenges of assimilating eddies while accurately modeling internal tides are considerable, but we note that the United States Navy has as a goal to run such a system operationally by 2018. For now, we have mapped the amount of SSH variance in non-stationary vs. stationary internal tides, as well as in the IGW continuum, in HYCOM (Savage et al., 2017a).

There are many more technical challenges for models of this size and complexity. Hourly output is standard for tidal analysis, but this makes the storage requirements 24 times more burdensome than the storage requirements of models that store daily-averaged outputs. Yet the spectra shown in Fig. 13.28 indicate that even hourly model outputs are not frequent enough to avoid aliasing of the IGW continuum in the outputs of such models. Another technical problem is that near-inertial waves, a crucial source of energy for the IGW continuum, are generated by high-frequency winds, while ocean models are often forced by atmospheric models that only update their fields every 3-6 hours. One solution to this problem would be to run high-resolution coupled ocean-atmosphere models, in which the atmosphere updates every time step, rather than high-resolution "forced ocean" models. The SAL term presents another challenge and opportunity. As noted in Hendershott (1972), the SAL term acts on all barotropic motions, not just tides, and should therefore act on the entire mass (non-steric) signal in ocean models. The computational cost and complexity of inline computations involving spherical harmonics has prevented most researchers from incorporating a "full SAL" (not just one acting on tidal motions) into global ocean general circulation models. Vinogradova et al. (2015) represents a significant recent attempt to solve this problem. The SAL

term did not add greatly to the cost of running their model. However, they were running relatively coarse resolution simulations, and it is not clear whether their solution would work well in simulations with much higher horizontal resolution. We have been in frequent discussions with mathematicians who have techniques that could potentially incorporate SAL without greatly increasing the computational cost.

A technical challenge for HYCOM in particular is the presence of numerical instabilities in specific regions, noted by Buijsman et al. (2016) and others. Ongoing efforts are underway to implement the Adcroft et al. (2008) solution for this instability in HYCOM. Technical challenges for the MITgcm simulations presented here include deciding whether these simulations should continue to be developed, and implementing a plan for more extensive comparison of the simulations to observations, as has been done with the HYCOM simulations.

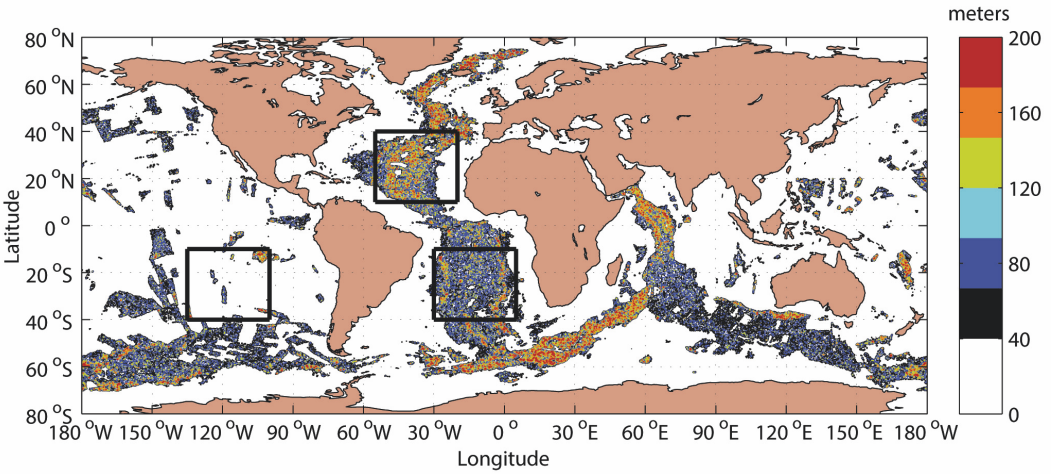

Figure 13.42. Area-weighted root mean square of the difference between model bathymetry with and without the statistical abyssal hill roughness of Goff and Arbic (2010) at 1/12.5°. The root mean square is calculated over a 1/4° × 1/4° sub-grid. Contours are drawn from 40 m to 200m at 40m intervals. The boxed regions shown in the South Pacific, North Atlantic and South Atlantic oceans are used in Timko et al. (2017) to estimate internal wave response to changes in bottom roughness. Reproduced from Figure 4 of Timko et al. (2017).

Another challenge relates to bathymetry. The Smith and Sandwell (1997) bathymetry dataset does not resolve topographic features with horizontal length scales less than about 10 km, except in limited regions where high-quality acoustic sounding data is available. As a result, abyssal hills, the most common landforms on Earth, are largely unresolved in global bathymetric datasets. It also means that the horizontal resolution of some global models, and many regional models, is quickly outstripping the actual feature resolution of the underlying topography—except, as noted above, in special regions where high-quality soundings are available throughout the domain. Goff and Arbic (2010) and Goff (2010) make note of this problem and offer, as a partial remedy, realizations, in both physical and spectral space, of topography that does include abyssal hills with the "correct" statistics. The spectral characterization of the Goff and Arbic (2010) and Goff (2010) products was used in offline computations of a parameterized topographic wave drag, that were then inserted inline into a global model of the eddying general circulation (Trossman et al., 2013, 2016). Both

the spectral and physical space realizations were used by Melet et al. (2013) in a linear analysis study of tidal conversion over abyssal hills.

In Timko et al. (2017), the statistical abyssal hill roughness was employed in HYCOM simulations of the internal tides, set up under the same simplified conditions used in Arbic et al. (2004) and Simmons et al. (2004b), to examine the extra explicitly resolved internal tide activity arising from the small-scale roughness missing in global bathymetric datasets. Timko et al. (2017) found that the roughness does indeed increase internal tide generation and energy levels, especially in the higher vertical modes that are generated by smaller-scale topography (St. Laurent and Garrett, 2002; Simmons et al., 2004b). Fig. 13.42 shows the small-scale roughness that we introduce through the Goff and Arbic (2010) and Goff (2010) work, as it appears once filtered down to 1/12.5° horizontal resolution. The method employed by Timko et al. (2017) to add statistical roughness to a global internal tide model could be adapted to researchers studying other phenomena, in other models, and with different grid resolutions. In fact, in regional models with higher resolutions than the 1/12.5° and 1/25° resolutions used in Timko et al. (2017)'s global models, the effects of the statistical roughness will be greater because as resolution increases the radius of the smoother that must be applied to put the raw statistical bathymetry onto a grid will decrease.

A persistent question, discussed at length amongst the co-authors of Arbic et al. (2004) and Simmons et al. (2004b), and again amongst the co-authors of Ansong et al. (2015), is whether a parameterized topographic internal wave drag, or some other damping mechanism, should be employed in global internal tide and IGW continuum models. One point of view is that parameterizing internal wave drag while at the same time partially resolving the spectrum constitutes double counting. A point of view argued in Arbic et al. (2004, 2010), Ansong et al. (2015), and Buijsman et al. (2016) is that such models do not resolve internal wave breaking and therefore still require some damping of low-mode internal tides to make up for this deficit. Ansong et al. (2015) shows that, at least for 1/12.5° HYCOM simulations, some damping is necessary for the internal tides to agree well with altimetry. We are currently planning to test damping mechanisms other than parameterized topographic internal wave drag, such as upper-ocean wave-wave interactions, in HYCOM. Of course, at some time in the future, models will reach the point where they are resolving much of the IGW spectrum and its cascade to small-scale dissipation, at which parameterized damping will indeed have to be abandoned.

Global internal tide and IGW continuum models appear to be resolving some of the nonlinear interactions needed to produce an IGW continuum spectrum; presumably, if they were not doing so, then they would not carry a partial continuum. An important question is what such models should do to "go the rest of the way" to the even smaller scales where internal wave breaking takes place. Driving regional models which have higher horizontal and vertical resolutions is one solution; letting eddy viscosities take care of the partial IGW cascade that has taken place is another. No doubt other ideas for handling this problem will arise as such models continue to advance.

Finally, it is likely that global internal tide and IGW continuum models will help us to understand better the processes leading to the IGW continuum. The classical paradigm is that the energy source for the IGW continuum is primarily near-inertial waves and internal tides, with

nonlinear interactions filling out the continuum. This view was supported by high-resolution two-dimensional (depth + one horizontal direction) numerical simulations in Sugiyama et al. (2009). However, Barkan et al. (2017) finds that a Garrett-Munk IGW continuum spectrum can develop in idealized models that contain only near-inertial waves and mesoscale eddies. Barkan's results suggest a role for mesoscale eddies in the formation of the IGW continuum spectrum. Whether there is a role for internal lee waves generated by mesoscale eddies flowing over topographic features in forming the IGW continuum, is another open question, discussed by the lead author with Stephanie Waterman and Bernard Barnier in September 2017. We conclude by stating that there are many interesting questions to explore with global internal tide and IGW continuum models.

Dedication

Brian Arbic dedicates his contributions to the work presented here to his beloved brother Joel Bernard Arbic, who passed away on December 2, 2017. Joel will forever be missed by his wife, two sons, parents, two brothers, in-laws, two nieces, and other relatives, as well as by his many friends.

Author contributions

BKA wrote this book chapter, with considerable organizational and editing help from ADN. JKA wrote the appendix. Several co-authors contributed to the editing and other presentation issues. All authors contributed to one or more of the following underpinnings of this book chapter: prior articles, comparison datasets, the development of the global oceanic internal tide and gravity wave simulations presented here, and numerous associated discussions. The first global internal tide simulations were performed at GFDL by BKA and HLS in collaboration with RWH and Stephen Garner. The first high-resolution, three-dimensional global simulations with simultaneous atmospheric and tidal forcing were performed in Naval Research Laboratory (NRL) HYCOM simulations by BKA, AJW, and EJM. Newer HYCOM simulations have been performed by JFS, JKA, and LZ, based upon coding legwork by AJW, and written about in papers by BKA, JKA, MCB, CAL, MM, HEN, JGR, ACS, JFS, and PGT. IS provided help with the Kalman filtering used in Ngodock et al. (2016). MHA, JTF, RBS, and ZZ provided observational datasets used in model-data comparisons, and helped with general interpretation of the results. The MITgcm simulations were configured and carried out by BCN, CEH, CNH, DM, and RBC. MM and RMP included the tidal forcing in the MITgcm simulations.

Acknowledgements

We thank many individuals, far too numerous to list here, for illuminating discussions on, and reviews of, our global internal tide and wave modeling research over the years. We thank Florent Lyard for a thorough review of this book chapter. We thank Richard Ray for very helpful comments on the first two sections of this chapter, and Stephen Garner and Eric Kunze for additional comments. BKA thanks Carl Wunsch for class notes on the IGW Sturm-Liouville problem, which helped greatly in formulating the appendix.

This book chapter stems from lectures at the 2017 GODAE school. BKA thanks the organizers of the GODAE school for their invitation to lecture there, and for putting together and editing a book based upon the lectures. BKA also thanks the four GODAE school students assigned to this chapter, Shaun Rigby, Alejandra Rodriguez, Pablo Rodriguez Ros, and Aurpita Saha, who provided helpful comments on early drafts. BKA participated in the GODAE school while on sabbatical. BKA thanks many French colleagues, especially Thierry Penduff, Rosemary Morrow, and Nadia Ayoub, for their help in procuring a sabbatical year in France.

The simulations in Arbic et al. (2004) and Simmons et al. (2004b) were performed on the high-performance computing cluster at the Geophysical Fluid Dynamics Laboratory (GFDL) of the National Oceanic and

Atmospheric Administration (NOAA). BKA thanks Stephen Garner, his postdoctoral advisor, for crucial collaborations on these early global internal tide papers.

Many of the papers underlying this review chapter were written by current and former members (JKA, CAL, ADN, ACS, and PGT) of BKA's research group at University of Michigan. BKA and his group members gratefully acknowledge financial support from US Naval Research Laboratory (NRL) contract N000173-06-2-C003, US Office of Naval Research (ONR) grants N00014-07-1-0392, N00014-09-1-1003, N00014-11-1-0487, N00014-15-1-2288, and N00014-17-1-2958, US National Science Foundation (NSF) grants OCE-0623159, OCE-0924481, OCE-0968783, OCE-0960820, and OCE-1351837, NASA grants NNX13AD95G, NNX16AH79G, and NNX17AH55G, a NASA Earth and Space Science Fellowship grant NNX16AO23H to ACS, and the University of Michigan Associate Professor Support Fund, derived from the Margaret and Herman Sokol Faculty Awards. Start-up and other funds, as well as local computer resources, from The University of Texas at Austin, Florida State University, and the University of Michigan are also acknowledged by BKA. MM collaborated with Arbic's group as a subcontractor and as such acknowledges support from a subcontract of ONR grant N00014-11-1-0487 to the University of Victoria. BKA's group acknowledges Michael Messina for substantial help in navigating computer resources at the University of Michigan.

Substantial analysis was also done at NRL, and most of the HYCOM simulations were performed there. All of the HYCOM simulations reported on here, except for those used in Timko et al. (2017), were supported by grants of computer time from the Department of Defense (DoD) High Performance Computing Modernization Program at the Navy DoD Supercomputing Resource Center. MCB, EJM, HEN, JGR, JFS, IS, AJW, and LZ acknowledge support from the ONR projects "Dynamics of the Indonesian Throughflow and its remote im impact", "Eddy resolving global ocean prediction including tides", "Global and remote littoral forcing in global ocean models", "Ageostrophic vorticity dynamics of the ocean", "NCOM-4DVAR, A multiscale approach for assessing predictability of ASW environment", "Extending predictability in coastal environments", "HYCOM global ocean forecast skill assessment", and the ONR and National Ocean Partnership Program (NOPP) sponsored project "Improving global surface and internal tides through two-way coupling with high resolution coastal models". MCB also acknowledges ONR grant N00014-15-1-2288.

RMP acknowledges the support of NSF grant OPP-1708308 and NASA grant NNX11AQ12G. HLS was supported by NSF (CPT) grant OCE-0968838 and ONR grant N00014-09-1-0399.

The MITgcm simulations were performed on the Pleiades supercomputer cluster at NASA Ames. We thank Ayan Chaudhuri for helping with inclusion of tidal forcing in MITgcm. PGT and BKA acknowledge the Texas Advanced Computing Center (TACC) at The University of Texas at Austin for providing HPC resources that have contributed to the research results reported in Timko et al. (2017). URL: http://www.tacc.utexas.edu. We thank the captains, crews, technical personnel and investigators who collected the in-situ observations used here over many cruises. Similarly, we thank the numerous engineers and scientists who made the satellite altimetry data used here possible.

This is NRL contribution NRL/BC/7320-18-3786 and has been approved for public release.

Appendices

A Linear internal gravity wave dispersion relation

A.1 Development of Sturm-Liouville problem

This appendix develops the linear IGW dispersion relation, and the related eigenfunctions for the horizontal velocities and vertical displacements of density surfaces, under the simplifying assumptions of a rigid lid at the ocean surface, and plane wave solutions. The more realistic case, of a free surface, can be found in, for instance, Nugroho (2017). The orthogonality of the eigenfunctions is affected by the nature of the boundary condition (rigid lid versus free surface).

The linearized governing equations for the conservation of mass, momentum, and density, under the Boussinesq/incompressible approximation, with total density $\rho = \bar{\rho} + \rho_0(z) + \rho'(x, y, z, t)$, are given by

$$\frac{\partial u}{\partial x} + \frac{\partial v}{\partial y} + \frac{\partial w}{\partial z} = 0, \tag{22}$$

$$\frac{\partial u}{\partial t} - fv = -\frac{1}{\bar{\rho}}\frac{\partial p'}{\partial x}, \tag{23}$$

$$\frac{\partial v}{\partial t} + fu = -\frac{1}{\bar{\rho}}\frac{\partial p'}{\partial y}, \tag{24}$$

$$\bar{\rho}\frac{\partial w}{\partial t} = -\frac{\partial p'}{\partial z} - \rho' g, \tag{25}$$

$$\frac{\partial \rho'}{\partial t} + w\frac{\mathrm{d}\rho_0}{\mathrm{d}z} = 0, \tag{26}$$

(see Gill, 1982; Wunsch and Stammer, 1997), where (u, v, w) are the velocities in the zonal, meridional, and vertical (x, y, z) directions respectively, f is the Coriolis frequency, p is pressure, g is acceleration due to gravity, $\bar{\rho}$ is a constant density, $\rho_0(z)$ is the background density variation and $\rho'(x, y, z, t)$ is the perturbation density due to internal gravity waves. Note the slight change in notation between the appendix and the remainder of the text; in earlier sections, ρ_0 was used to denote the constant average seawater density.

Combine equations (25) and (26) to get

$$\frac{\partial^2 w}{\partial t^2} - w\frac{g}{\bar{\rho}}\frac{\mathrm{d}\rho_0}{\mathrm{d}z} = -\frac{1}{\bar{\rho}}\frac{\partial^2 p'}{\partial z \partial t}. \tag{27}$$

The buoyancy frequency, N, is defined as

$$N^2 = -\frac{g}{\bar{\rho}}\frac{\mathrm{d}\rho_0}{\mathrm{d}z}, \tag{28}$$

such that (27) becomes

$$\frac{\partial^2 w}{\partial t^2} + N^2 w = -\frac{1}{\bar{\rho}}\frac{\partial^2 p'}{\partial z \partial t}. \tag{29}$$

Combine (22)-(24) to obtain

$$\begin{aligned} \left(\frac{\partial^2}{\partial t^2} + f^2\right)\frac{\partial w}{\partial z} &= \frac{1}{\bar{\rho}}\frac{\partial}{\partial t}\left(\frac{\partial^2 p'}{\partial x^2} + \frac{\partial^2 p'}{\partial y^2}\right), \\ \Longrightarrow \left(\frac{\partial^2}{\partial t^2} + f^2\right)\frac{\partial w}{\partial z} &= \frac{1}{\bar{\rho}}\frac{\partial}{\partial t}\nabla_h^2 p'. \end{aligned} \tag{30}$$

Introduce separation of variables (for separable solutions):

$$[u(x, y, z, t),\, v(x, y, z, t)] = [U(x, y, t),\, V(x, y, t)]F(z), \tag{31}$$

$$w(x, y, z, t) = \tilde{P}(x, y, t)G(z), \tag{32}$$

$$p'(x, y, z, t) = \bar{\rho}\tilde{P}(x, y, t)F(z). \tag{33}$$

Note that each of the equations (31)-(33) should actually be a summation over different vertical modes (e.g. Kundu, 1990, page 499); for example,

$$w(x, y, z, t) = \sum_{n=0}^{\infty} \tilde{P}_n(x, y, t)G_n(z),$$

where *n* is the vertical mode number. For simplicity we leave the equations as given. In addition, we set all dependent variables to be proportional to $e^{-i\sigma t}$, where σ is the wave frequency. Our goal is to determine the vertical structure functions *F (z)* and *G(z)*. Substitute (32)-(33) into (29) to get

$$\begin{aligned}
[(-i\sigma)^2 + N^2]\tilde{P} \cdot G(z) &= i\sigma\tilde{P} \cdot \frac{\mathrm{d}F}{\mathrm{d}z}, \\
\implies (N^2 - \sigma^2)G(z) &= i\sigma\frac{\mathrm{d}F}{\mathrm{d}z}, \\
\implies \boxed{G(z) = \frac{i\sigma}{N^2 - \sigma^2}\frac{\mathrm{d}F}{\mathrm{d}z}.}
\end{aligned} \tag{34}$$

Note that because $i\sigma$ is a constant, the z dependence of the vertical displacement function is given by an expression in Wunsch and Stammer (1997), viz.

$$\boxed{G_1(z) = \frac{G(z)}{i\sigma} = \frac{1}{N^2 - \sigma^2}\frac{\mathrm{d}F}{\mathrm{d}z}.} \tag{35}$$

Substituting (32)-(33) into (30) yields

$$(-i\sigma)^2\tilde{P}\frac{\mathrm{d}G}{\mathrm{d}z} + f^2\tilde{P}\frac{\mathrm{d}G}{\mathrm{d}z} = -(i\sigma)F(z)\nabla_h^2\tilde{P}, \tag{36}$$

$$\begin{aligned}
\implies (\sigma^2 - f^2)\tilde{P}\frac{\mathrm{d}G}{\mathrm{d}z} &= (i\sigma)F(z)\nabla_h^2\tilde{P}, \\
\implies \frac{(\sigma^2 - f^2)(\mathrm{d}G(z)/\mathrm{d}z)}{(i\sigma)F(z)} &= \frac{\nabla_h^2\tilde{P}}{\tilde{P}}.
\end{aligned} \tag{37}$$

Note that the left-hand-side of (37) is a function of only z and the right-hand-side is independent of z. Thus we can write

$$\frac{(\sigma^2 - f^2)(\mathrm{d}G(z)/\mathrm{d}z)}{(i\sigma)F(z)} = \frac{\nabla_h^2\tilde{P}}{\tilde{P}} = -\gamma^2 \tag{38}$$

$$\implies \boxed{(\sigma^2 - f^2)\frac{\mathrm{d}G(z)}{\mathrm{d}z} = -(i\sigma)\gamma^2 F(z)} \tag{39}$$

where γ^2 is a separation constant. From equations (34) and (39), we can determine equations for only the *F(z)* and *G(z)* functions. From these equations, we respectively obtain

$$\begin{aligned}
\frac{\mathrm{d}G}{\mathrm{d}z} &= \frac{\mathrm{d}}{\mathrm{d}z}\left(\frac{i\sigma}{N^2 - \sigma^2}\frac{\mathrm{d}F}{\mathrm{d}z}\right), \\
\frac{\mathrm{d}G}{\mathrm{d}z} &= -\frac{i\sigma}{\sigma^2 - f^2}\gamma^2 F(z).
\end{aligned}$$

Equating the above equations results in

$$\boxed{\frac{\mathrm{d}}{\mathrm{d}z}\left(\frac{\sigma^2 - f^2}{N^2 - \sigma^2}\frac{\mathrm{d}F}{\mathrm{d}z}\right) + \gamma^2 F(z) = 0.} \tag{40}$$

From (39) we see that

$$(\sigma^2 - f^2)\frac{\mathrm{d}^2G}{\mathrm{d}z^2} = -(i\sigma)\gamma^2\frac{\mathrm{d}F}{\mathrm{d}z}.$$

From equation (34), we have

$$\frac{\mathrm{d}F}{\mathrm{d}z} = \frac{N^2 - \sigma^2}{i\sigma}G(z). \tag{41}$$

Therefore, we have

$$(\sigma^2 - f^2)\frac{\mathrm{d}^2 G}{\mathrm{d}z^2} = -\gamma^2(N^2 - \sigma^2)G(z),$$
$$\Longrightarrow \boxed{\frac{\mathrm{d}^2 G}{\mathrm{d}z^2} + \frac{N^2 - \sigma^2}{\sigma^2 - f^2}\gamma^2 G(z) = 0.} \tag{42}$$

Thus the equation governing the vertical modal structure of velocity and pressure is (40) and that governing the vertical displacement is (42). The boundary conditions for these equations come from requiring that the vertical velocity vanish ($w = 0$) at the top ($z = 0$) and bottom ($z = -H$) of the domain. From equation (32), this implies that $G(z) = 0$ at $z = 0$ and $z = -H$. Equation (41) then implies that $\frac{\mathrm{d}F}{\mathrm{d}z} = 0$ at $z = 0$ and $z = -H$.

The main equations and their boundary conditions, with an assumed rigid lid, are rewritten below for convenience:

$$\frac{\mathrm{d}}{\mathrm{d}z}\left(\frac{\sigma^2 - f^2}{N^2 - \sigma^2}\frac{\mathrm{d}F}{\mathrm{d}z}\right) + \frac{1}{\lambda^2}F(z) = 0, \tag{43}$$

with boundary conditions

$$\frac{\mathrm{d}F}{\mathrm{d}z} = 0 \quad \text{at} \quad z = 0, -H, \tag{44}$$

where the condition at z=0 is the rigid lid assumption, and

$$\frac{\mathrm{d}^2 G}{\mathrm{d}z^2} + \left(\frac{N^2 - \sigma^2}{\sigma^2 - f^2}\right)\frac{1}{\lambda^2}G(z) = 0, \tag{45}$$

with boundary conditions

$$G(z) = 0 \quad \text{at} \quad z = 0, -H, \tag{46}$$

where H is the water depth and $1/\lambda^2 = \gamma^2$ represents the eigenvalues of the eigenfunctions $F(z)$ and $G(z)$. We denoted γ^2 as $1/\lambda^2$ here so that the equations resemble those solved in our MATLAB code (discussed below).

A.1.1 Dispersion relation & meaning of eigenvalues

Here we determine the meaning of the eigenvalues in the vertical mode equations, and we derive the dispersion relation for internal gravity waves. First we combine the governing equations (22)-(26) into a single equation for the vertical velocity, w. We perform $\nabla_h^2 \cdot(29) + \frac{\partial}{\partial z}(30)$ to eliminate p', and obtain, after some steps,

$$\frac{\partial^2}{\partial t^2}\left(\nabla_h^2 + \frac{\partial^2}{\partial z^2}\right)w + N^2\nabla_h^2 w + f^2\frac{\partial^2 w}{\partial z^2} = 0. \tag{47}$$

We now assume a plane-wave solution:

$$w = G(z)e^{i(kx+ly-\sigma t)}. \tag{48}$$

Note that the plane-wave assumption does not impact vertical structure; however, in the actual ocean, the horizontal structure is not always well-represented by plane waves. Substituting (48) into (47) results in

$$(-i\sigma)^2\left[G(z)(ik)^2 + G(z)(il)^2 + \frac{\mathrm{d}^2 G}{\mathrm{d}z^2}\right] + N^2[G(z)(ik)^2 + G(z)(il)^2] + f^2\frac{\mathrm{d}^2 G}{\mathrm{d}z^2} = 0,$$
$$\Longrightarrow \sigma^2(k^2 + l^2)G(z) - \sigma^2\frac{\mathrm{d}^2 G}{\mathrm{d}z^2} - N^2(k^2 + l^2) + f^2\frac{\mathrm{d}^2 G}{\mathrm{d}z^2} = 0,$$
$$\Longrightarrow (k^2 + l^2)(\sigma^2 - N^2)G(z) + (f^2 - \sigma^2)\frac{\mathrm{d}^2 G}{\mathrm{d}z^2} = 0,$$
$$\Longrightarrow (k^2 + l^2)(N^2 - \sigma^2)G(z) + (\sigma^2 - f^2)\frac{\mathrm{d}^2 G}{\mathrm{d}z^2} = 0.$$

Thus,

$$\frac{\mathrm{d}^2 G}{\mathrm{d}z^2} + \left(\frac{N^2 - \sigma^2}{\sigma^2 - f^2}\right)(k^2 + l^2)G(z) = 0. \tag{49}$$

Comparison of equations (49) and (45) demonstrates that the eigenvalues, λ, are related to the horizontal wavenumber:

$$\boxed{\lambda^2 = \frac{1}{k^2 + l^2}}. \tag{50}$$

An alternative (and simpler) way to derive (50) is to employ equation (38):

$$\frac{\nabla_h^2 \tilde{P}}{\tilde{P}} = -\gamma^2 = -\frac{1}{\lambda^2}, \tag{51}$$

and assume

$$\tilde{P} = P_0 e^{i(kx + ly - \sigma t)}. \tag{52}$$

Substituting (52) into (51) gives

$$\frac{\nabla_h^2 \tilde{P}}{\tilde{P}} = -(k^2 + l^2) = -\frac{1}{\lambda^2},$$

$$\Longrightarrow \lambda^2 = \frac{1}{k^2 + l^2}.$$

We rewrite equation (45) as

$$\frac{1}{N^2 - \sigma^2}\frac{\mathrm{d}^2 G}{\mathrm{d}z^2} + \frac{1}{(\sigma^2 - f^2)\lambda^2}G(z) = 0, \tag{53}$$

and define the eigenspeed, c_e, as

$$\frac{1}{c_e^2} = \frac{1}{(\sigma^2 - f^2)\lambda^2}, \tag{54}$$

such that

$$\boxed{c_e^2 = \frac{(\sigma^2 - f^2)}{k^2 + l^2}}, \tag{55}$$

or

$$\boxed{\sigma^2 = f^2 + c_e^2(k^2 + l^2).} \tag{56}$$

Equation (56) is the **dispersion relation** of internal gravity waves for a general $N^2(z)$. It is analogous to the dispersion relation for Poincare waves (surface gravity waves in the absence of horizontal boundaries), with the surface gravity wave speed $\sqrt{gH}$ replaced by the eigenspeed c_e for IGWs. Equation (53) may now be written as

$$\frac{1}{N^2 - \sigma^2}\frac{\mathrm{d}^2 G}{\mathrm{d}z^2} + \frac{1}{c_e^2}G(z) = 0. \tag{57}$$

To see that the eigenspeed, c_e, is the speed of propagation of waves, we present two arguments: a comparison to the surface gravity wave dispersion relation, and a scaling analysis.

1) We note that equation (56) is identical to the dispersion relation for surface (external) gravity waves if c_e^2 is identified with gH. This argument is similar to that presented in Kundu (1990; page 501).
2) Since $z \sim H$, the left-hand term of (53) scales as (assuming $N \gg \sigma$) $\frac{1}{N^2 H^2}G(z) = \frac{1}{c_e^2}G(z)$. Therefore, we have $c_e \approx N H$.

To derive the dispersion relation for a constant $N(z)$, we employ equation (57) and assume $G \propto e^{imz}$, such that $\frac{\mathrm{d}^2}{\mathrm{d}z^2} \sim -m^2$. Thus (57) becomes

$$\begin{aligned} \frac{-m^2}{N^2-\sigma^2} &= -\frac{1}{c_e^2}, \\ \implies c_e^2 &= \frac{N^2-\sigma^2}{m^2}. \end{aligned} \tag{58}$$

Substituting (58) into the dispersion relation (56) gives

$$\begin{aligned} \sigma^2 &= f^2 + \frac{N^2-\sigma^2}{m^2}(k^2+l^2), \\ \implies \sigma^2 m^2 &= f^2 m^2 + (N^2-\sigma^2)(k^2+l^2), \\ \implies \sigma^2(m^2+k^2+l^2) &= f^2 m^2 + N^2(k^2+l^2), \\ \boxed{\implies \sigma^2 &= \frac{f^2 m^2 + N^2(k^2+l^2)}{m^2+k^2+l^2}.} \end{aligned} \tag{59}$$

We see immediately from (59) that the frequency of IGWs is bounded by *f* and *N*, as discussed previously.

A.2 Orthogonality & Orthonormality of eigenfunctions

As mentioned above, the eigenfunctions of the Sturm-Liouville equation are known to be orthogonal [see the book by Heinbockel (2003) for additional details]. We show this in the following section. Experts, or those uninterested in the details of the proof of the orthogonality of the Sturm-Liouville system, may wish to skip this section and proceed to the next section. Note once again that when the rigid lid assumption employed here is replaced by a more realistic free surface boundary condition, the orthogonality of the displacement functions becomes more involved (Nugroho, 2017). Using vertical modes computed using a rigid lid assumption to perform an energy budget in shelf regions can be problematic (Nugroho, 2017; Florent Lyard, personal communication, 2018).

A.2.1 General Orthogonal Functions

The inner product of two real functions $f(z)$ and $g(z)$ with respect to a weighting function W(z) (which is never negative) over the interval $a \le z \le b$ is defined by

$$(f,g) = \int_a^b W(z) f(z) g(z) \mathrm{d}z. \tag{60}$$

The inner product of the function with itself is equal to the square of the norm and is written as

$$(f,f) = ||f||^2 = \int_a^b W(z) f(z)^2 \mathrm{d}z. \tag{61}$$

A set of functions $\{f_1(z), f_2(z), \cdots, f_n(z), \cdots, f_m(z), \cdots\}$ is said to be orthogonal over an interval $a \le z \le b$ with respect to a weight function $W(z) > 0$ if for all integer values of n and m, with $n \neq m$, the inner product of f_m with f_n satisfies

$$(f_m, f_n) = \int_a^b W(z) f_m(z) f_n(z) \mathrm{d}z = 0, \quad m \neq n. \tag{62}$$

If the sequence of functions $\{f_n(z)\}$, $n = 0, 1, 2, \cdots$ is an **orthogonal** sequence we can write for integers m and n that the inner product satisfies the relation [combining (61) and (62)]

$$(f_m, f_n) = ||f_n||^2 \delta_{mn} = \begin{cases} 0, & m \neq n \\ ||f_n||^2, & m = n \end{cases} \tag{63}$$

where δ_{mn} is the Kronecker delta. In the special case where $||f_n||^2 = 1$, for all values of n, the sequence of functions is said to be orthonormal over the interval $a \le z \le b$.

If a sequence $\{g_n(z)\}$ is orthogonal with respect to the weight function $W(z)$, then we can construct a new orthonormal sequence $f_n(z)$, defined by

$$f_n(z) = \frac{g_n(z)}{||g_n(z)||}. \tag{64}$$

We show below that equation (64) is orthogonal. Multiply (64) by $W(z)f_m(z)$ and integrate to get

$$\begin{aligned} I &= \int W(z) f_n(z) f_m(z) \mathrm{d}z = \frac{1}{||g_n(z)||} \int W(z) g_n(z) f_m(z) \mathrm{d}z, \\ &= \frac{1}{||g_n(z)||} \int W(z) g_n(z) \frac{g_m(z)}{||g_m(z)||} \mathrm{d}z, \\ &= \frac{1}{||g_n(z)||||g_m(z)||} \int W(z) g_n(z) g_m(z) \mathrm{d}z, \\ &= 0, \quad \text{for} \quad n \neq m, \end{aligned} \tag{65}$$

because the sequence $\{g_n(z)\}$ is orthogonal. Moreover, from (64)

$$\begin{aligned} ||f_n(z)|| = \frac{||g_n(z)||}{||g_n(z)||} = 1, \\ \implies ||f_n(z)||^2 = 1, \end{aligned} \tag{66}$$

and therefore, the sequence $\{f_n(z)\}$ is orthonormal.

The proof above shows that the most important property is orthogonality. Once an orthogonal sequence is obtained, we can easily construct an orthonormal sequence by dividing by the norm of the functions.

A.2.2 Orthogonality of eigenfunctions

Consider the Sturm-Liouville equation

$$\frac{\mathrm{d}}{\mathrm{d}z}\left(Q(z)\frac{\mathrm{d}F}{\mathrm{d}z}\right) + W(z)\lambda F(z) = 0, \tag{67}$$

with general boundary condition

$$\alpha F(z) + \beta \frac{\mathrm{d}F(z)}{\mathrm{d}z} = 0 \quad \text{at} \quad z = a, b, \tag{68}$$

where α and β are constants. We remark that, one could go through the following derivations using the more general boundary condition above, as is done in Nugroho (2017). However, here we use simplified boundary conditions, either

$$F(z) = 0 \quad \text{at} \quad z = a, b, \tag{69}$$

or

$$\frac{\mathrm{d}F(z)}{\mathrm{d}z} = 0 \quad \text{at} \quad z = a, b. \tag{70}$$

To determine orthogonality, we consider equation (67) with two different values of λ such that

$$\frac{\mathrm{d}}{\mathrm{d}z}\left(Q(z)\frac{\mathrm{d}F_n}{\mathrm{d}z}\right) + W(z)\lambda_n F_n(z) = 0, \tag{71}$$

$$\frac{\mathrm{d}}{\mathrm{d}z}\left(Q(z)\frac{\mathrm{d}F_m}{\mathrm{d}z}\right) + W(z)\lambda_m F_m(z) = 0. \tag{72}$$

Perform [(72)×F_n]-[(71)×F_m] to obtain

$$F_n \frac{\mathrm{d}}{\mathrm{d}z}\left(Q(z)\frac{\mathrm{d}F_m}{\mathrm{d}z}\right) - F_m \frac{\mathrm{d}}{\mathrm{d}z}\left(Q(z)\frac{\mathrm{d}F_n}{\mathrm{d}z}\right) + (\lambda_m - \lambda_n) W(z) F_m F_n = 0. \tag{73}$$

Before returning to (73), we note that

$$\frac{\mathrm{d}}{\mathrm{d}z}\left(F_nQ(z)\frac{\mathrm{d}F_m}{\mathrm{d}z}\right) = F_n\frac{\mathrm{d}}{\mathrm{d}z}\left(Q(z)\frac{\mathrm{d}F_m}{\mathrm{d}z}\right) + Q(z)\frac{\mathrm{d}F_m}{\mathrm{d}z}\frac{\mathrm{d}F_n}{\mathrm{d}z}, \tag{74}$$

$$\frac{\mathrm{d}}{\mathrm{d}z}\left(F_mQ(z)\frac{\mathrm{d}F_n}{\mathrm{d}z}\right) = F_m\frac{\mathrm{d}}{\mathrm{d}z}\left(Q(z)\frac{\mathrm{d}F_n}{\mathrm{d}z}\right) + Q(z)\frac{\mathrm{d}F_m}{\mathrm{d}z}\frac{\mathrm{d}F_n}{\mathrm{d}z}, \tag{75}$$

so that (74)-(75) gives

$$F_n\frac{\mathrm{d}}{\mathrm{d}z}\left(Q(z)\frac{\mathrm{d}F_m}{\mathrm{d}z}\right) - F_m\frac{\mathrm{d}}{\mathrm{d}z}\left(Q(z)\frac{\mathrm{d}F_n}{\mathrm{d}z}\right) = \frac{\mathrm{d}}{\mathrm{d}z}\left(F_nQ(z)\frac{\mathrm{d}F_m}{\mathrm{d}z}\right) - \frac{\mathrm{d}}{\mathrm{d}z}\left(F_mQ(z)\frac{\mathrm{d}F_n}{\mathrm{d}z}\right). \tag{76}$$

Substituting (76) into (73) yields

$$\frac{\mathrm{d}}{\mathrm{d}z}\left(F_nQ(z)\frac{\mathrm{d}F_m}{\mathrm{d}z}\right) - \frac{\mathrm{d}}{\mathrm{d}z}\left(F_mQ(z)\frac{\mathrm{d}F_n}{\mathrm{d}z}\right) + (\lambda_m - \lambda_n)W(z)F_mF_n = 0. \tag{77}$$

Integrating equation (77) from $z = a$ to $z = b$ results in

$$\left[F_nQ(z)\frac{\mathrm{d}F_m}{\mathrm{d}z}\right]_a^b - \left[F_mQ(z)\frac{\mathrm{d}F_n}{\mathrm{d}z}\right]_a^b + (\lambda_m - \lambda_n)\int_a^b W(z)F_mF_n\mathrm{d}z = 0.$$

The first two terms vanish due to the boundary condition (69) or (70):

$$\frac{\mathrm{d}F_m(z)}{\mathrm{d}z} = 0 = \frac{\mathrm{d}F_n(z)}{\mathrm{d}z}\,\mathrm{at}\quad z = a,\, b. \tag{78}$$

Therefore, we obtain

$$\begin{aligned}(\lambda_m - \lambda_n)\int_a^b W(z)F_mF_n\mathrm{d}z = 0, \quad n \neq m,\\ \Longrightarrow \int_a^b W(z)F_mF_n\mathrm{d}z = 0, \quad n \neq m,\end{aligned} \tag{79}$$

proving the **orthogonality** of the $F(z)$ eigenfunctions.

Note that when $m = n$, the vanishing of the left-hand side does not give us any additional information but the resulting integral is expected to be nonzero (Heinbockel, 2003). As shown above, by having an orthogonal sequence $\{F_n(z)\}$, we can construct an orthonormal sequence by dividing by the norm.

Comparing (67) to (43) shows that the weight function $W(z) = 1$ so that the sequence $\{F_n(z)\}$ may be othonormalized as

$$\frac{1}{||F_n(z)||||F_m(z)||}\int_{-H}^0 F_n(z)F_m(z)\mathrm{d}z = \delta_{mn}. \tag{80}$$

On the other hand, comparing (67) to (45) shows that

$$W(z) = \left(\frac{N^2 - \sigma^2}{\sigma^2 - f^2}\right),$$

so that we can orthonormalize $\{G_n(z)\}$ by

$$\frac{1}{||G_n(z)||G_m(z)||}\int_{-H}^0 \left(\frac{N^2 - \sigma^2}{\sigma^2 - f^2}\right)G_n(z)G_m(z)\mathrm{d}z = \delta_{mn}, \tag{81}$$

such that

$$||G_n(z)||^2 = \int_{-H}^0 \left(\frac{N^2 - \sigma^2}{\sigma^2 - f^2}\right)G_n^2(z)\mathrm{d}z.$$

A.3 Computation of expansion coefficients

The vertical structure of internal gravity waves in the ocean (or from a model) can be decomposed into a linear combination of dynamical modes (Wunsch, 1975) such that

$$\mathbf{u}(z,t) = \sum_{n=0}^{M} \mathbf{u}_n(t) F_n(z), \tag{82}$$

$$\eta(z,t) = \sum_{n=1}^{M} \eta_n(t) G_n(z), \tag{83}$$

where $\mathbf{u} = (u, v)$ is the horizontal velocity and η is the isopycnal displacement, n is an index of vertical mode number, z is vertical coordinate, t is time, M is the total number of vertical modes, and $F_n(z)$ and $G_n(z)$ are the fixed vertical structures of the nth baroclinic mode respectively.

In practice, $\mathbf{u}(z, t)$ and $\eta(z, t)$ are known from either observational measurements or from a model output, and $F_n(z)$ and $G_n(z)$ can be computed from a profile of buoyancy frequency, $N(z)$. Here we discuss how to compute the expansion coefficients $\mathbf{u}_n(t)$ and $\eta_n(t)$ in (82)-(83). We first discuss a theoretical approach, and later outline a second approach via the method of least squares.

A.3.1 Theoretical solution method

Suppose that $F_n(z)$ is an eigenfunction such that

$$\frac{1}{\mathcal{H}} \int_{-H}^{0} F_n(z) F_m(z) \mathrm{d}z = \delta_{mn}, \tag{84}$$

where $\mathcal{H} = ||F_n(z)||F_m(z)||$. The F's may also be orthonormalized in a depth-averaged sense by setting

$$\mathcal{H} = ||F_n(z)||^2 = H, \tag{85}$$

[e.g., see equation (2.3) in Flierl (1978)], and similarly for the displacement modal functions. If we expand the velocity u as (82):

$$u(z,t) = \sum u_n(t) F_n(z),$$

Then

$$\begin{aligned}
\frac{1}{\mathcal{H}} \int_{-H}^{0} F_n(z) u(z,t) \mathrm{d}z &= \frac{1}{\mathcal{H}} \int_{-H}^{0} F_n(z) \sum_m u_m(t) F_m(z) \mathrm{d}z \\
&= \sum_m u_m(t) \frac{1}{\mathcal{H}} \int_{-H}^{0} F_n(z) F_m(z) \mathrm{d}z \\
&= \sum_m u_m(t) \delta_{mn} \\
&= u_n(t).
\end{aligned}$$

Thus,

$$\boxed{u_n(t) = \frac{1}{\mathcal{H}} \int_{-H}^{0} F_n(z) u(z,t) \mathrm{d}z.} \tag{86}$$

Following an approach similar to the one above, we can determine the expansion coefficients for the vertical displacement. For an orthogonal sequence, $\{G_n(z)\}$, we have

$$\frac{1}{\mathcal{G}} \int_{-H}^{0} W(z) G_n(z) G_m(z) \mathrm{d}z = \delta_{mn}, \tag{87}$$

where $\mathcal{G} = ||G_n(z)||G_m(z)||$ and $W(z)$ is a weighting function. Using the expansion in (83), we get

$$\begin{aligned}\frac{1}{\mathcal{G}}\int_{-H}^{0} W(z)G_n(z)\eta(z,t)\mathrm{d}z &= \frac{1}{\mathcal{G}}\int_{-H}^{0} W(z)G_n(z)\sum_m \eta_m(t)G_m(z)\mathrm{d}z \\ &= \sum_m \eta_m(t)\frac{1}{\mathcal{G}}\int_{-H}^{0} W(z)G_n(z)G_m(z)\mathrm{d}z \\ &= \sum_m \eta_m(t)\delta_{mn} \\ &= \eta_n(t).\end{aligned}$$

Thus,

$$\boxed{\eta_n(t) = \frac{1}{\mathcal{G}}\int_{-H}^{0} W(z)G_n(z)\eta(z,t)\mathrm{d}z.} \tag{88}$$

A.3.2 Least-squares method

Another practical way to determine the expansion coefficients is by solving each of (82)-(83) as a least-squares problem (Dushaw et al., 1995; Nash et al., 2005). For instance, at each time, the u equation from (82) may be cast as a multivariate regression model (Emery and Thompson, 1997), such that

$$u_i = a_0F_{i0} + a_1F_{i1} + a_2F_{i2}\cdots + a_MF_{iM} + \varepsilon_i \tag{89}$$

where each i (= 1, $\cdots$, N) equation is for each depth and ε_i is the error to be minimized in the regression method. The set of equations in (89) can then be written as

$$\mathbf{U} = \mathbf{A}\cdot\mathbf{F} + \mathbf{E}, \tag{90}$$

where

$$\mathbf{U} = \begin{pmatrix} u_1 \\ u_2 \\ \cdots \\ \cdots \\ u_N \end{pmatrix}, \quad \mathbf{F} = \begin{pmatrix} F_{10} & F_{11} & \cdots & F_{1M} \\ F_{20} & F_{21} & \cdots & F_{2M} \\ \cdots & \cdots & \cdots & \cdots \\ \cdots & \cdots & \cdots & \cdots \\ F_{N0} & F_{N1} & \cdots & F_{NM} \end{pmatrix},$$

$$\mathbf{A} = \begin{pmatrix} a_0 \\ a_1 \\ \cdots \\ \cdots \\ a_M \end{pmatrix}, \quad \mathbf{E} = \begin{pmatrix} \varepsilon_1 \\ \varepsilon_2 \\ \cdots \\ \cdots \\ \varepsilon_N \end{pmatrix},$$

and the boldface letters indicate matrices. Solving (90) for **A**, we obtain

$$\mathbf{A} = (\mathbf{F}'\cdot\mathbf{F})^{-1}\mathbf{F}'\cdot\mathbf{U} \tag{91}$$

(see Emery and Thompson, 1997, page 239-240, for more details). Note that MATLAB's *regress* and *plsregress* functions give solutions similar to (91).

A.4 Solutions to the modal equations

There are no known analytical solutions for general $N^2(z)$ (see e.g., Kundu, 1990; Gill, 1982). Equation (43) is a Sturm-Liouville type of equation for which the eigenfunctions are known to be orthogonal. Often, equation (43) with (44) is solved for $F(z)$ (sometimes the solution approach also gives dF/dz) and then equations (34)-(35) can be used to obtain $G(z)$. To be precise, the $i\sigma$ factor in (34) is a constant, and the entire function in (35) will be adjusted to be orthonormal, so we can ignore the $i\sigma$.

Also note that the λ's are unknown and must be solved for together with the eigenfunctions. Numerical solutions can be found via two main methods:

1) The matrix approach in which equation (43) is often discretized.

2) The **shooting method**, in which equation (43) is solved in two parts. This approach is described in this section and was used to compute linear IGW dispersion relations in Müller et al. (2015) and Savage et al. (2017b), based upon Matlab code that was originally developed by Glenn Flierl for solving the normal modes of the quasi-geostrophic equations (Glenn Flierl, personal communication, 1995; Flierl, 1978). See also Emery & Thomson (1997) for references to NAG Fortran shooting method routines.

   a) Integrating (43) gives

$$\left(\frac{\sigma^2 - f^2}{N^2 - \sigma^2}\frac{\mathrm{d}F}{\mathrm{d}z}\right) = -\frac{1}{\lambda^2}\int_{-H}^{0} F(z)\mathrm{d}z. \tag{92}$$

   Let

$$d = -\frac{1}{\lambda^2}\int_{-H}^{0} F(z)\mathrm{d}z, \tag{93}$$

$$\Longrightarrow \frac{\mathrm{d}d}{\mathrm{d}z} = -\frac{1}{\lambda^2}F(z). \tag{94}$$

   b) Note that (94) is a first order differential equation which can be solved using Euler's method, for example, for a given boundary condition at one end. Because $F(z = 0)$ is unknown, we set $F = 1$ at the top boundary (later we will normalize the function) and make an initial guess for λ. However, d (which is proportional to the derivative of $F(z)$) is known at the first boundary from the boundary conditions. Once we have d, we can then solve (92); given in the form

$$\frac{\mathrm{d}F}{\mathrm{d}z} = \left(\frac{N^2 - \sigma^2}{\sigma^2 - f^2}\right)d, \tag{95}$$

   to get $F(z)$. This gives the value of $F(z)$ at the next step, and the procedure is repeated until we get to the other boundary.

   c) We then check to see whether the solution from the step above satisfies the boundary condition at the other end, $\frac{\mathrm{d}F}{\mathrm{d}z}|_{z=-H} = 0$. If not, then we need to choose a different initial guess for λ.

   d) The approach used here is to provide the code with several initial guesses for λ and then determine several derivatives, $d(z)$ at $z = -H$. Because the boundary conditions require $d(z) = 0$ at $z = -H$, each pair of λ guesses that gives values of d with different signs at $z = -H$ can be used to narrow-in on the actual λ's that will give $d(-H) \approx 0$. [For example, if λ_1 results in $d = 20 > 0$ and λ_2 results in $d = -40 < 0$ at $z = -H$, then we know that the value lies between the two λ's. We may then narrow-in on the actual λ by choosing the mean of λ_1 and λ_2]. The *fzero* function in MATLAB can be used to find the zeros (i.e., the actual λ's).

   e) Now that we have the λ's that give us the correct boundary condition at the other end, we have our solution $F(z)$. The $F(z)$ functions are then normalized as described in section A.2.

   f) Determine the vertical displacement eigenfunctions $G(z)$ by dividing the d's by $\sigma^2 - f^2$ (see equation 35).

A.4.1 Example solution

Using the buoyancy frequency displayed in Fig. 13.43a, we computed the first three vertical normal modes for velocity (Fig. 13.43b) and vertical displacement (Fig. 13.43c). As is common in the ocean, the buoyancy frequency profile depicted in Fig. 13.43a is surface-intensified (i.e., has its largest values in the upper ocean). The three lowest horizontal velocity normal modes, $F(z)$, depicted in Fig. 13.43b also take on their largest values in the upper ocean. The mode-2 and mode-3 displacement normal modes, $G(z)$, take on their largest values in deeper parts of the water column. Figs. 13.43b and 13.43c demonstrate that, as is dictated by the mathematics of the Sturm-Liouville problem, the nth horizontal velocity mode has n zero crossings, while the nth displacement mode has n-1 zero crossings.

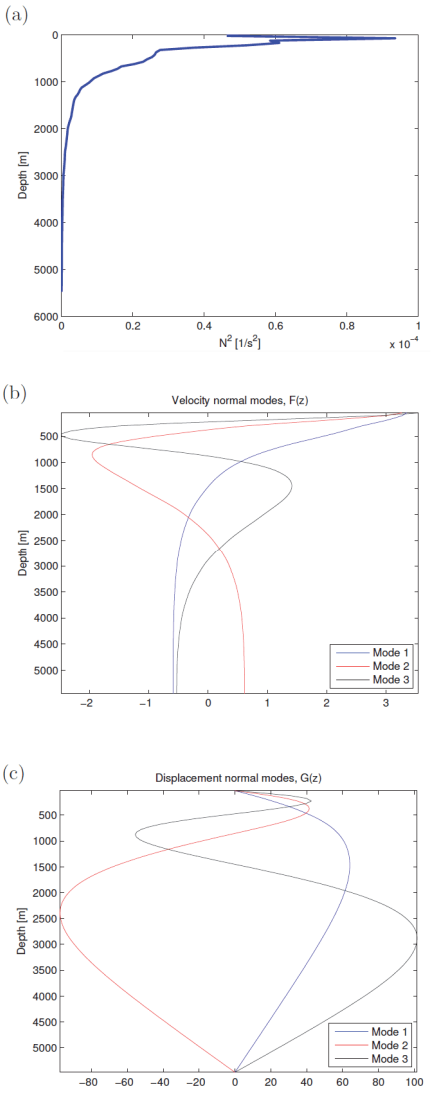

Figure 13.43. (a) Buoyancy frequency profile. Vertical mode structures for (b) horizontal velocity, and (c) vertical displacement. The modal structures are dimensionless, and satisfy orthogonality conditions as described in the text.

References

Accad, Y., and C.L. Pekeris (1978), Solution of the tidal equations for the M_2 and S_2 tides in the world oceans from a knowledge of the tidal potential alone. Philosophical Transactions of the Royal Society of London A290, 235-266, doi:10.1098/rsta.1978.0083.

Adcroft, A., R. Hallberg, and M. Harrison (2008), A finite volume discretization of the pressure gradient force using analytical integration. Ocean Modelling 22, 106-113, doi:10.1016/j.ocemod.2008.02.001.

Alford, M.H. (2003), Redistribution of energy available for ocean mixing by long-range propagation of internal waves. Nature 423, 159–162, doi:10.1038/nature01628.

Alford, M.H., J.A. McKinnon, Z. Zhao, R. Pinkel, J. Klymak, and T. Peacock (2007), Internal waves across the Pacific. Geophysical Research Letters 34, L24601, doi:10.1029/2007GL031566.

Ansong, J.K., B.K. Arbic, M.C. Buijsman, J.G. Richman, J.F. Shriver, and A.J. Wallcraft (2015), Indirect evidence for substantial damping of low-mode internal tides in the open ocean. Journal of Geophysical Research Oceans 120, 6057-6071, doi:10.1002/2015JC010998.

Ansong, J.K., B.K. Arbic, M.H. Alford, M.C. Buijsman, J.F. Shriver, Z. Zhao, J.G. Richman, H.L. Simmons, P.G. Timko, A.J. Wallcraft, and L. Zamudio (2017), Semidiurnal internal tide energy fluxes and their variability in a global ocean model and moored observations. Journal of Geophysical Research Oceans 122, 1882-1900, doi:10.1002/2016JC012184.

Arbic, B.K., S.T. Garner, R.W. Hallberg, and H.L. Simmons (2004), The accuracy of surface elevations in forward global barotropic and baroclinic tide models. Deep-Sea Research II 51, 3069-3101, doi:10.1016/j.dsr2.2004.09.014.

Arbic, B.K. (2005), Atmospheric forcing of the oceanic semidiurnal tide. Geophysical Research Letters 32, L02610, doi:10.1029/2004GL021668.

Arbic, B.K., P. St-Laurent, G. Sutherland, and C. Garrett (2007), On the resonance and influence of tides in Ungava Bay and Hudson Strait. Geophysical Research Letters 34, L17606, doi:10.1029/2007GL030845.

Arbic, B.K., R.H. Karsten, and C. Garrett (2009), On tidal resonance in the global ocean and the back-effect of coastal tides upon open-ocean tides. Atmosphere-Ocean 47, 239-266, doi:10.3137/OC311.2009.

Arbic, B.K. and C. Garrett (2010), A coupled oscillator model of shelf and ocean tides. Continental Shelf Research 30, 564-574, doi:10.1016:/j.csr.2009.07.008.

Arbic, B.K., A.J. Wallcraft, and E.J. Metzger (2010), Concurrent simulation of the eddying general circulation and tides in a global ocean model. Ocean Modelling 32, 175-187, doi:10.1016/j.ocemod.2010.01.007.

Arbic, B.K., J.G. Richman, J.F. Shriver, P.G. Timko, E.J. Metzger, and A.J. Wallcraft (2012a), Global modeling of internal tides within an eddying ocean general circulation model. Oceanography 25, doi:10.5670/oceanog.2012.38.

Arbic, B.K., R.B. Scott, G.R. Flierl, A.J. Morten, J.G. Richman, and J.F. Shriver (2012b), Nonlinear cascades of surface oceanic geostrophic kinetic energy in the frequency domain. Journal of Physical Oceanography 42, 1577-1600, doi:10.1175/JPO-D-11-0151.1.

Arbic, B.K., K.L. Polzin, R.B. Scott, J.G. Richman, and J.F. Shriver (2013), On eddy viscosity, energy cascades, and the horizontal resolution of gridded satellite altimeter products. Journal of Physical Oceanography 43, 283-300, doi:10.1175/JPO-D-11-0240.1.

Arbic, B.K., M. Müller, J.G. Richman, J.F. Shriver, A.J. Morten, R.B. Scott, G. Sérazin, and T. Penduff (2014), Geostrophic turbulence in the frequency-wavenumber domain: Eddy-driven low-frequency variability. Journal of Physical Oceanography 44, 2050- 2069, doi:10.1175/JPO-D-13-054.1.

Baines, P.G. (1982), On internal tide generation models. Deep- Sea Research 29, 307–338, doi:10.1016/0198-0149(82)90098-X.

Barkan, R., K.B. Winters, and J.C. McWilliams (2017), Stimulated imbalance and the enhancement of eddy kinetic energy dissipation by internal waves. Journal of Physical Oceanography 47, 181-198, doi:10.1175/JPO-D-16-01170-1.

Bell, T.H. (1975), Lee waves in stratified flows with simple harmonic time dependence. Journal of Fluid Mechanics 67, 705–722, doi:10.1017/S0022112075000560.

Bleck, R. (2002), An oceanic general circulation model framed in hybrid isopycnic-Cartesian coordinates. Ocean Modeling 4, 55-88, doi:10.1016/S1463-5003(01)00012-9.

Buijsman, M.C., B.K. Arbic, J.A.M. Green, R.W. Helber, J.G. Richman, J.F. Shriver, P.G. Timko, and A. Wallcraft (2015), Optimizing internal wave drag in a forward barotropic model with semidiurnal tides. Ocean Modelling 85, 42-55, doi:10.1016/j.ocemod.2014.11.003.

Buijsman, M.C., J.K. Ansong, B.K. Arbic, J.G. Richman, J.F. Shriver, P.G. Timko, A.J. Wallcraft, C.B. Whalen, and Z. Zhao (2016), Impact of internal wave drag on the semidiurnal energy balance in a global ocean circulation model. Journal of Physical Oceanography 46, 1399-1419, doi:10.1175/JPO-D-15-0074.1.

Buijsman, M.C., B.K. Arbic, J.G. Richman, J.F. Shriver, A.J. Wallcraft, and L. Zamudio (2017), Semidiurnal internal tide incoherence in the equatorial Pacific. Journal of Geophysical Research Oceans 122, 5286-5305, doi:10.1002/2016JC012590.

Cairns, J.L., and G.O. Williams (1976), Internal wave observations from a midwater float, 2. Journal of Geophysical Research 81(12), 1943–1950, doi:10.1029/ JC081i012p01943.

Callies, J., and R. Ferrari (2013), Interpreting energy and tracer spectra of upper-ocean turbulence in the submesoscale range (1–200 km). Journal of Physical Oceanography 43, 2456–2474, doi:10.1175/JPO-D-13-063.1.

Capet, X., J.C. McWilliams, M.J. Molemaker, and A.F. Shchepetkin (2008), Mesoscale to submesoscale transition in the California Current System. Part I: Flow structure, eddy flux, and observational tests. Journal of Physical Oceanography 38, 29-43, doi:10.1175/2007JPO3671.1.

Carrère and Lyard (2003), Modeling the barotropic response of the global ocean to atmospheric wind and pressure forcing: Comparisons with observations. Geophysical Research Letters 30, 1275, doi:10.1029/2002GL016473.

Carter, G.S., O.B. Fringer, and E.D. Zaron (2012), Regional models of internal tides. Oceanography 25, 56–65, doi:10.5670/oceanog.2012.42.

Cartwright, D.E. (1975), A subharmonic lunar tide in the seas off Western Europe. Nature 257, 277-280, doi:10.1038/257277a0.

Cartwright, D.E. (1999), Tides: A Scientific History. Cambridge University Press, Cambridge.

Cartwright, D.E., and R.D. Ray (1990), Oceanic tides from Geosat altimetry. Journal of Geophysical Research 95, 3069–3090, doi:10.1029/JC095iC03p03069.

Cartwright, D.E., and R.J. Tayler (1971), New computations of the tide-generating potential. Geophysical Journal of the Royal Astronomical Society 23, 45–74, doi:10.1111/j.1365-246X.1971.tb01803.x.

Chapman, S., and R.S. Lindzen (1970), Atmospheric Tides. D. Reidel Press, Dordrecht.

Charette, M.A., and W.H.F. Smith (2010), The volume of the earth's ocean. Oceanography 23, 112-114, doi:10.5670/oceanog.2010.51.

Chassignet, E.P., H.E. Hurlburt, E.J. Metzger, O.M. Smedstad, J.A. Cummings, G.R. Halliwell, R. Bleck, R. Baraille, A.J. Wallcraft, C. Lozano, H.L. Tolman, A. Srinivasan, S. Hankin, P. Cornillon, R. Weisberg, A. Barth, R. He, F. Werner, and J. Wilkin (2009), Global ocean prediction with the HYbrid Coordinate Ocean Model (HYCOM). Oceanography 22, 64–76, doi:10.5670/oceanog.2009.39.

Chassignet, E.P., and X. Xu (2017), Impact of horizontal resolution (1/12° to 1/50°) on Gulf Stream separation, penetration, and variability. Journal of Physical Oceanography 47, 1999-2021, doi:10.1175/JPO-D-17-0031.1.

Clarke, A.J. (1991), The dynamics of barotropic tides over the continental shelf and slope (review). In: Tidal Hydrodynamics. B.B. Parker (Ed.). John Wiley and Sons, pp. 79–108.

Csanady, G.T. (2001), Air-sea Interaction: Laws and Mechanisms. Cambridge University Press, Cambridge.

Cummins, P.F., and L.Y. Oey (1997), Simulation of barotropic and baroclinic tides off Northern British Columbia. Journal of Physical Oceanography 27, 762-781, doi:10.1175/1520-0485(1997)027<0762:SOBABT>2.0.CO;2.

Cummins, P.F., R.H. Karsten, and B.K. Arbic (2010), The semi-diurnal tide in Hudson Strait as a resonant channel oscillation. Atmosphere-Ocean 48, 163-176, doi:10.3137/OC307.2010.

D'Asaro, E.A. (1984), Wind forced internal waves in the North Pacific and Sargasso Sea. Journal of Physical Oceanography 14, 781–794, doi:10.1175/1520-0485(1984)014<0781:WFIWIT>2.0.CO.

D'Asaro, E.A. (1985), The energy flux from the wind to near-inertial motions in the surface mixed layer. Journal of Physical Oceanography 15, 1043–1059, doi:10.1175/1520-0485(1985)015<1043:TEFFTW>2.0.CO.

Doherty, K.W., D.E. Frye, S.P. Liberatore, and J.M. Toole (1999), A moored profiling instrument. Journal of Atmospheric and Oceanic Technology 16, 1816–1829, doi:10.1175/1520-0426(1999)016<1816:AMPI>2.0.CO;2.

Doodson, A.T. (1921), Harmonic development of the tide-generating potential. Proceedings of the Royal Society of London A100, 305-329, doi:10.1098/rspa.1921.0088.

Ducousso, N., J. Le Sommer, J.-M. Molines, and M. Bell (2017), Impact of the "Symmetric Instability of the Computational Kind" at mesoscale and submesoscale-permitting resolutions. Ocean Modelling 120, 18-26, doi:10.1016/j.ocemod.2017.10.006.

Dunphy, M., and K.G. Lamb (2014), Focusing and vertical mode scattering of the first mode internal tide by mesoscale eddy interaction. Journal of Geophysical Research 119, 523-536, doi:10.1002/2013JC009293.

Dushaw, B.D., B.D. Cornuelle, P.F. Worcester, B.M. Howe, and D.S. Luther (1995), Barotropic and baroclinic tides in the central North Pacific Ocean determined from long-range reciprocal acoustic transmissions. Journal of Physical Oceanography 25, 631–647, doi:10.1175/1520-0485(1995)025<0631:BABTIT>2.0.CO.

Egbert, G.D., A.F. Bennett, and M.G.G. Foreman (1994), Topex/Poseidon tides estimated using a global inverse model. Journal of Geophysical Research 99, 24821–24852, doi:10.1029/94JC01894.

Egbert, G.D., and S.Y. Erofeeva (2002), Efficient inverse modeling of barotropic ocean tides. Journal of Atmospheric and Oceanic Technology 19, 183-204, doi:10.1175/1520-0426(2002)019<0183:EIMOBO>2.0.CO.

Egbert, G.D., and R.D. Ray (2000), Significant dissipation of tidal energy in the deep ocean inferred from satellite altimeter data. Nature 405, 775–778, doi:10.1038/35015531.

Egbert, R.D., and R.D. Ray (2001), Estimates of M_2 tidal energy dissipation from TOPEX/Poseidon altimeter data. Journal of Geophysical Research 106, 22475–22502, doi:10.1029/2000JC000699.

Egbert, R.D., and R.D. Ray (2003), Semi-diurnal and diurnal tidal dissipation from TOPEX/Poseidon altimetry. Geophysical Research Letters 30, 1907, doi:10.1029/2003GL017676.

Egbert, G.D., R.D. Ray, and B.G. Bills (2004), Numerical modeling of the global semidiurnal tide in the present day and in the last glacial maximum. Journal of Geophysical Research 109, C03003, doi:10.1029/2003JC001973.

Egbert, G.D., and R.D. Ray (2017), Tidal prediction. In: The Sea: The Science of Ocean Prediction, printed as a special issue of Journal of Marine Research 75, 189-237, doi:10.1357/002224017821836761.

Emery, W.J., and R.E. Thompson (1997), Data Analysis Methods in Physical Oceanography. Pergamon Press.

Flierl, G.R. (1978), Models of vertical structure and the calibration of two-layer models. Dynamics of Atmospheres and Oceans 2, 341-381, doi:10.1016/0377-0265(78)90002-7.

Foreman, M.G.G. (1977), Manual for tidal heights analysis and prediction. Pacific Marine Science Report 77-10, Institute of Ocean Sciences, Sidney.

Foreman, M.G.G. (2004), Manual for tidal currents analysis and prediction, Pacific Marine Science Report 78-6, Institute of Ocean Sciences, Sidney.

Foreman, M.G.G., J.Y. Cherniawsky, and V.A. Ballantyne (2009), Versatile harmonic tidal analysis: Improvements and applications. Journal of Atmospheric and Oceanic Technology 26, 806-817, doi:10.1175/2008JTECHO615.1.

Fu, L.-L., D. Alsdorf, R. Morrow, E. Rodriguez, and N. Mognard (Eds.) (2012), SWOT: The Surface Water and Ocean Topography Mission: Wide-Swath Altimetric Measurement of Water Elevation on Earth, Jet Propulsion Laboratory, Pasadena, California.

Fu, L.-L., and A. Cazenave (Eds.) (2001), Satellite Altimetry and Earth Sciences: A Handbook of Techniques and Applications, Academic Press, San Diego.

Furiuchi, N., T. Hibiya, and Y. Niwa (2008), Model predicted distribution of wind-induced internal wave energy in the world's oceans. Journal of Geophysical Research 113, C09034, doi:10.1029/2008JC004768.

Garner, S.T. (2005), A topographic drag closure built on an analytical base flux. Journal of the Atmospheric Sciences 62, 2302-2315, doi:10.1175/JAS3496.1.

Garrett, C. (1972), Tidal resonance in the Bay of Fundy and Gulf of Maine. Nature 238, 441–443, doi:10.1038/238441a0.

Garrett, C.J.R., and W.H. Munk (1975), Space-time scales of internal waves. A progress report. Journal of Geophysical Research 80, 291–297, doi:10.1029/ JC080i003p00291.

Garrett, C. and D. Greenberg (1977), Predicting changes in tidal regime: The open boundary problem. Journal of Physical Oceanography 7, 171–181, doi:10.1175/1520-0485(1977)007<0171:PCITRT>2.0.CO.

Gill, A. E. (1982), Atmosphere-Ocean Dynamics. Academic Press, New York.

Gille, S.T., K. Speer, J.R. Ledwell, and A.C. Naveira Garabato (2007), Mixing and stirring in the Southern Ocean. Eos, Transactions American Geophysical Union 88(39), 382- 383, doi:10.1029/2007EO390002.

Goff, J.A. (2010), Global prediction of abyssal hill root-mean-square heights from small-scale altimetric gravity variability. Journal of Geophysical Research 115, B12104, doi:10.1029/2010JB007867.

Goff, J.A., and B.K. Arbic (2010), Global prediction of abyssal hill roughness statistics for use in ocean models from digital maps of paleo-spreading rate, paleo-ridge orientation, and sediment thickness. Ocean Modelling 32, 36-43, doi:10.1016/j.ocemod.2009.10.001.

Gordeev, R.G., B.A. Kagan, and E.V. Polyakov (1977), The effects of loading and self-attraction on global ocean tides: The model and the results of a numerical experiment. Journal of Physical Oceanography 7, 161–170, doi:10.1175/1520-0485(1977)007<0161:TEOLAS>2.0.CO.

Gregg, M.C. (1989), Scaling turbulent dissipation in the thermocline. Journal of Geophysical Research 94, 9686-9898, doi:10.1029/JC094iC07p09686.

Griffies, S.M. (2005), Fundamentals of ocean climate models. Princeton University Press, Princeton.

Griffies, S.M., C. Böning, F.O. Bryan, E.P. Chassignet, R. Gerdes, H. Hasumi, A. Hirst, A.-M. Treguier, and D. Webb (2000), Developments in ocean climate modeling. Ocean Modelling 2, 123-192, doi:10.1016/S1463-5003(00)00014-7.

Hallberg, R. (2005), A thermobaric instability of Lagrangian vertical coordinate ocean models. Ocean Modelling 8, 279–300, doi:10.1016/j.ocemod.2004.01.001.

Heath, R.A. (1981), Estimates of the resonant period and Q in the semi-diurnal tidal band in the North Atlantic and Pacific Oceans. Deep Sea Research Part A 2, 481–493, doi:10.1016/0198-0149(81)90139-4.

Hecht, M. W., and H. Hasumi, Eds. (2008), Ocean Modeling in an Eddying Regime. Geophysical Monographs 177, American Geophysical Union.

Heinbockel, J.H. (2003), Mathematical Methods for Partial Differential Equations. Trafford Publishing, Victoria.

Hendershott, M.C. (1972), The effects of solid earth deformation on global ocean tides. Geophysical Journal of the Royal Astronomical Society 29, 389–402, doi:10.1111/j.1365-246X.1972.tb06167.x.

Hogan, T.F., M. Liu, J.A. Ridout, M.S. Peng, T.R. Whitcomb, B.C. Ruston, C.A. Reynolds, S.D. Eckermann, J.R. Moskaitis, N.L. Baker, J.P. McCormack, K.C. Viner, J.G. McLay, M.K. Flatau, L. Xu, C. Chen, and S.W. Chang (2014), The Navy Global Environmental Model. Oceanography 27, 116-125, doi:10.5670/oceanog.2014.73.

Holloway, P.E. (1996), A numerical model of internal tides with application to the Australia North West Shelf. Journal of Physical Oceanography 26, 21–37, doi:10.1175/1520-0485(1996)026<0021:ANMOIT>2.0.CO.

Jayne, S.R., and L.C. St. Laurent (2001), Parameterizing tidal dissipation over rough topography. Geophysical Research Letters 28, 811-814, doi:10.1029/2000GL012044.

Josey, S.A., S. Gulev, and L. Yu (2013), Exchanges through the ocean surface. In: Ocean Circulation and Climate, A 21st century perspective, second edition. G. Siedler, S. Griffies, J. Gould, and J. Church (Eds.) 103, Academic Press, 115-140, doi:10.1016/B978-0-12-391851-2.00005-2.

Kang, S.K., M.G.G. Foreman, W.R. Crawford, and J.Y. Cherniawsky (2000), Numerical modeling of internal tide generation along the Hawaiian Ridge. Journal of Physical Oceanography 30, 1083–1098, doi:10.1175/1520-0485(2000)030<1083:NMOITG>2.0.CO.

Kelly, S.M., N.L. Jones, J.D. Nash, and A.F. Waterhouse (2013), The geography of semidiurnal mode-1 internal tide energy loss. Geophysical Research Letters 40, 4689-4693, doi:10.1002/grl.50872.

Klymak, J.M., R. Pinkel, and L. Rainville (2008), Direct breaking of the internal tide near topography: Kaena Ridge, Hawaii. Journal of Physical Oceanography 38, 380-399, doi:10.1175/2007JPO3728.1.

Kuhlmann, J., H. Dobslaw, and M. Thomas (2011), Improved modeling of sea level patterns by incorporating self-attraction and loading. Journal of Geophysical Research 116, C11036, doi:10.1029/2011JC007399.

Kundu, P.K. (1990), Fluid Mechanics, Academic Press, New York.

Kunze, E. (2017a), Internal-wave-driven mixing: Global geography and budgets. Journal of Physical Oceanography 47, 1325-1345, doi:10.1175/JPO-D-16-0141.1.

Kunze, E. (2017b), The internal-wave-driven meridional overturning circulation. Journal of Physical Oceanography 47, 2673-2689, doi:10.1175/JPO-D-16-0142.1.

LaCasce, J.H. (2000), Floats and f/H. Journal of Marine Research 58, 61–95, doi:10.1357/002224000321511205.

Laplace, P.S. (1775), Recherches sur plusieurs points du système du monde. Mémoires de l'Académie Royale des Sciences Paris 88, 75-182. [Reprinted in Oeuvres Complètes de Laplace, Gauthier-Villars, Paris, 9 (1893)].

Laplace, P.S. (1776), Recherches sur plusieurs points du système du monde. Mémoires de l'Académie Royale des Sciences Paris 89, 177-264. [Reprinted in Oeuvres Complètes de Laplace, Gauthier-Villars, Paris, 9 (1893)].

Large, W.G., and S.G. Yeager (2004), Diurnal and decadal global forcing for ocean and sea-ice models: The data sets and climatologies. Technical Note tN-460+ST, NCAR, Boulder, Colorado, doi:10.5065/D6KK98Q6.

Le Provost, C., M.L. Genco, F. Lyard, P. Vincent, and P. Canceil (1994), Spectroscopy of the world ocean tides from a finite element hydrodynamic model. Journal of Geophysical Research 99(C12), 24,777–24,797, doi:10.1029/94JC01381.

Luecke, C.A., B.K. Arbic, S.L. Bassette, J.G. Richman, J.F. Shriver, M.H. Alford, O.M. Smedstad, P.G. Timko, D.S. Trossman, and A.J. Wallcraft (2017), The global mesoscale eddy available potential energy

field in models and observations. Journal of Geophysical Research Oceans 122, 9126-9143, doi:10.1002/2017JC013136.

Lyard, F., F. Lefevre, T. Letellier, and O. Francis (2006), Modelling the global ocean tides: Modern insights from FES2004. Ocean Dynamics 56, 394–415, doi:10.1007/s10236-006-0086-x.

MacKinnon, J.A., Z. Zhao, C.B. Whalen, A.F. Waterhouse, D.S. Trossman, O.M. Sun, L.C. St. Laurent, H.L. Simmons, K. Polzin, R. Pinkel, A. Pickering, N.J. Norton, J.D. Nash, R. Musgrave, L.M. Merchant, A.V. Melet, B. Mater, S. Legg, W.G. Large, E. Kunze, J.M. Klymak, M. Jochum, S.R. Jayne, R.W. Hallberg, S.M. Griffies, S. Diggs, G. Danabasoglu, E.P. Chassignet, M.C. Buijsman, F.O. Bryan, B.P. Briegleb, A. Barna, B.K. Arbic, J.K. Ansong, and M.H. Alford (2017), Climate process team on internal-wave driven ocean mixing. Bulletin of the American Meteorological Society 98, 2429-2454, doi:10.1175/BAMS-D-16-0030.1.

Maltrud, M.E., and J.L. McClean (2005), An eddy resolving global 1/10° ocean simulation. Ocean Modelling 8, 31-54, doi:10.1016/j.ocemod.2003.12.001.

Marshall, J., A. Adcroft, C. Hill, L. Perelman, and C. Heisey (1997), A finite-volume, incompressible Navier Stokes model for studies of the ocean on parallel computers. Journal of Geophysical Research 102, 5753-5766, doi:10.1029/96JC02775.

McComas, C.H., and F.P. Bretherton (1977), Resonant interactions of oceanic internal waves. Journal of Physical Oceanography 82, 1397-1412, doi:10.1029/JC082i009p01397.

Melet, A., M. Nikurashin, C. Muller, S. Falahat, J. Nycander, P.G. Timko, B.K. Arbic, and J.A. Goff (2013), Internal tide generation by abyssal hills using analytical theory. Journal of Geophysical Research Oceans 118, 6303-6318, doi:10.1002/2013JC009212.

Merrifield, M.A., P.E. Holloway, and T.M. Shaun Johnston (2001), The generation of internal tides at the Hawaiian Ridge. Geophysical Research Letters 28, 559–562, doi:10.1029/2000GL011749.

Moum, J.N., D.M. Farmer, W.D. Smyth, L. Armi, and S. Vagle (2003), Structure and generation of turbulence at interfaces strained by internal solitary waves propagating shoreward over the continental shelf. Journal of Physical Oceanography 33, 2093-2112, doi:10.1175/1520-0485(2003)033<2093:SAGOTA>2.0.CO;2.

Müller, M. (2007), The free oscillations of the world ocean in the period range 8 to 165 hours including the full loading effect. Geophysical Research Letters 34, L05606, doi:10.1029/2006GL028870.

Müller, M., H. Haak, J. H. Jungclaus, J. Sündermann and M. Thomas (2010), The impact of ocean tides on a climate model simulation. Ocean Modelling 35, 304-313, doi:/10.1016/j.ocemod.2010.09.001.

Müller, M., J. Cherniawsky, M. Foreman, and J.-S. von Storch (2012), Global map of M_2 internal tide and its seasonal variability from high resolution ocean circulation and tide modelling. Geophysical Research Letters 39, L19607, doi:10.1029/2012GL053320.

Müller, M., B.K. Arbic, J.G. Richman, J.F. Shriver, E.L. Kunze, R.B. Scott, A.J. Wallcraft, and L. Zamudio (2015), Toward an internal gravity wave spectrum in global ocean models. Geophysical Research Letters 42, 3474-3481, doi:10.1002/2015GL063365.

Müller, P., G. Holloway, F. Henyey, and N. Pomphrey (1986), Nonlinear interactions among internal gravity waves. Reviews of Geophysics 24(3), 493–536, doi:10.1029/RG024i003p00493.

Munk, W.H., and G.J.F. MacDonald (1960), The rotation of the earth. Cambridge University Press, London.

Munk, W.H., and C. Wunsch (1998), Abyssal recipes II: energetics of tidal and wind mixing. Deep Sea Research I 45, 1977–2010, doi:10.1016/S0967-0637(98)00070-3.

Nash, J.D., M.H. Alford, and E. Kunze (2005), Estimating internal wave energy fluxes in the ocean. Journal of Atmospheric and Oceanic Technology 22, 1551-1570, doi:10.1175/JTECH1784.1.

Nash, J.D., E.L. Shroyer, S.M. Kelly, M.E. Inall, T.F. Duda, M.D. Levine, N.L. Jones, and R.C. Musgrave (2012), Are any coastal internal tides predictable? Oceanography 25(2), 80–95, doi:10.5670/oceanog.2012.44.

Newton, I. (1687), Philosophiae Naturalis Principia Mathematica.

Ngodock, H.E., I. Souopgui, A.J. Wallcraft, J.G. Richman, J.F. Shriver, and B.K. Arbic (2016), On improving the accuracy of the M_2 barotropic tides embedded in a high-resolution global ocean circulation model. Ocean Modelling 97, 16-26, doi:10.1016/j.ocemod.2015.10.011.

Nikurashin, M., and R. Ferrari (2011), Global energy conversion rate from geostrophic flows into internal lee waves in the deep ocean. Geophysical Research Letters 38, L08610, doi: 10.1029/2011GL046576.

Niwa, Y., and T. Hibiya (2001), Numerical study of the spatial distribution of the M_2 internal tide in the Pacific Ocean. Journal of Geophysical Research 106, 22229–22441, doi:10.1029/2000JC000770.

Nugroho, D. (2017), The tide in a general circulation pattern in the Indonesian Seas. PhD dissertation. Université de Toulouse.

Nugroho, D., A. Koch-Larrouy, P.Gaspar, F. Lyard, G. Reffray, and B. Tranchant (2017), Modelling explicit tides in the Indonesian Seas: An important process for sea water properties. Marine Pollution Bulletin 131, Part B, 7-18, doi:10.1016/j.marpol-bul.2017.06.033.

Nycander, J. (2005), Generation of internal waves in the deep ocean by tides. Journal of Geophysical Research 110, C10028, doi:10.1029/2004JC002487.

Paiva, A.M., J.T. Hargrove, E.P. Chassignet, and R. Bleck (1999), Turbulent behavior of a fine-mesh (1/12 degree) numerical simulation of the North Atlantic. Journal of Marine Systems 21, 307-320, doi:10.1016/S0924-7963(99)00020-2.

Parke, M.E., and M.C. Hendershott (1980), M_2, S_2, K_1 models of the global ocean tide on an elastic earth. Marine Geodesy 3, 379–408, doi:10.1080/01490418009388005.

Pawlowicz, R., B. Beardsley, S. Lentz (2002), Classical tidal harmonic analysis including error estimates in MATLAB using T-TIDE. Computers and Geosciences 28, 929–937, doi:10.1016/S0098-3004(02)00013-4.

Pedlosky, J. (1996), Ocean Circulation Theory. Springer-Verlag, Berlin.

Penduff, T., B. Barnier, J.-M. Molines, and G. Madec (2006), On the use of current meter data to assess the realism of ocean model simulations. Ocean Modelling 11, 399–416, doi:10.1016/j.ocemod.2005.02.001.

Platzman, G.W. (1991), Tidal evidence for ocean normal modes. In: Tidal Hydrodynamics. B.B.Parker (Ed.), John Wiley and Sons, pp. 13–26.

Platzman, G.W., G.A. Curtis, K.S. Hansen, and R.D. Slater (1981), Normal modes of the World Ocean. Part II: Description of modes in the period range 8 to 80 hours. Journal of Physical Oceanography 11, 579–603, doi:10.1175/1520-0485(1981)011<0579:NMOTWO>2.0.CO.

Pollard, R.T., and R.C. Millard, Jr. (1970), Comparison between observed and simulated wind-generated inertial oscillations. Deep-Sea Research 17, 813-821, doi:10.1016/0011-7471(70)90043-4.

Polzin, K. (2004), Heuristic description of internal wave dynamics. Journal of Physical Oceanography 34, 214–230, doi:10.1175/1520-0485(2004)034<0214:AHDOIW>2.0.CO.

Polzin, K.L., J.M. Toole, and R.W. Schmitt (1995), Finescale parameterization of turbulent dissipation. Journal of Physical Oceanography 25, 306-328, doi:10.1175/1520-0485(1995)025<0306:FPOTD>2.0.CO;2.

Polzin, K.L., J.M. Toole, J.R. Ledwell, and R.W. Schmitt (1997), Spatial variability of turbulent mixing in the abyssal ocean. Science 276, 93-96, doi:10.1126/science.276.5309.93.

Ponte, R. (1994), Understanding the relation between wind- and pressure-driven sea level variability. Journal of Geophysical Research 99, 8033-8039, doi:10.1029/94JC00217.

Ponte, A.L., and P. Klein (2015), Incoherent signature of internal tides on sea level in idealized numerical simulations. Geophysical Research Letters 42, 1520–1526, doi:10.1002/2014GL062583.

Price, J.F., and M. O'Neil Baringer (1994), Outflows and deep water production by marginal seas. Progress in Oceanography 33, 161-200, doi:10.1016/0079-6611(94)90027-2.

Pugh, D.T. (1987), Tides, Surges, and Mean Sea-level: A Handbook for Scientists and Engineers. Wiley, Chichester.

Qiu, B., T. Nakano, S. Chen, and P. Klein (2017), Submesoscale transition from geostrophic flows to internal waves in the northwestern Pacific upper ocean. Nature Communications 8, 14055, doi:10.1038/ncomms14055.

Qiu, B., S. Chen, P. Klein, J. Wang, H. Torres, L.-L. Fu, and D. Menemenlis (2018), Seasonality in transition scale from balanced to unbalanced motions in the world ocean. Journal of Physical Oceanography 48, 591-605, doi:10.1175/JPO-D-17-0169.1.

Ray, R.D. (1998), Ocean self-attraction and loading in numerical tidal models. Marine Geodesy 21, 181–192, doi:10.1080/01490419809388134.

Ray, R.D. (1999), A global ocean tide model from Topex/Poseidon altimetry: GOT99.2, NASA Technical Memorandum 209478, Goddard Space Flight Center, Greenbelt, MD.

Ray, R.D. (2013), Precise comparisons of bottom-pressure and altimetric ocean tides. Journal of Geophysical Research Oceans 118, 4570–4584, doi:10.1002/jgrc.20336.

Ray, R.D., and D.A. Byrne (2010), Bottom pressure tides along a line in the southeast Atlantic Ocean and comparisons with satellite altimetry. Ocean Dynamics 60, 1167–1176, doi:10.1007/s10236-010-0316-0.

Ray, R.D., and G.D. Egbert (2004), The global S_1 tide. Journal of Physical Oceanography 34, 1922-1935, doi:10.1175/1520-0485(2004)034<1922:TGST>2.0.CO.

Ray, R.D., and G.D. Egbert (2017), Tides and satellite altimetry. In: Satellite Altimetry over Oceans and Land Surfaces. D. Stammer, A. Cazenave (Eds.), Taylor and Francis, pp. 427-458.

Ray, R.D., and G.T. Mitchum (1996), Surface manifestation of internal tides generated near Hawaii. Geophysical Research Letters 23, 2101–2104, doi:10.1029/96GL02050.

Ray, R.D., and G.T. Mitchum (1997), Surface manifestation of internal tides in the deep ocean: Observations from altimetry and tide gauges. Progress in Oceanography 40, 135–162, doi:10.1016/S0079-6611(97)00025-6.

Ray, R.D., and R.M. Ponte (2003), Barometric tides from ECMWF operational analyses. Annales Geophysicae 21, 1897–1910, doi:10.5194/angeo-21-1897-2003.

Richman, J.G., B.K. Arbic, J.F. Shriver, E.J. Metzger, and A.J. Wallcraft (2012), Inferring dynamics from the wavenumber spectra of an eddying global ocean model with embedded tides. Journal of Geophysical Research 117, C12012, doi:10.1029/2012JC008364.

Rocha, C.B., T.K. Chereskin, S.T. Gille, and D. Menemenlis (2016a), Mesoscale to submesoscale wavenumber spectra in Drake Passage. Journal of Physical Oceanography 46, 601–620, doi:10.1175/JPO-D-15-0087.1.

Rocha, C.B., S.T. Gille, T.K. Chereskin, and D. Menemenlis (2016b), Seasonality of submesoscale dynamics in the Kuroshio Extension. Geophysical Research Letters 43, 11304–11311, doi:10.1002/2016GL071349.

Roosbeek, F. (1996), RATGP95: A harmonic development of the tide-generating potential using an analytical method. Geophysical Journal International 126, 197–204, doi:10.1111/j.1365-246X.1996.tb05278.x.

Rosmond, T.E., J. Teixeira, M. Peng, T.F. Hogan, and R. Pauley (2002), Navy Operational Global Atmospheric Prediction System (NOGAPS): Forcing for ocean models. Oceanography 15, 99-108, doi:10.5670/oceanog.2002.40.

Savage, A.C., B.K. Arbic, J.G. Richman, J.F. Shriver, M.H. Alford, M.C. Buijsman, J.T. Farrar, H. Sharma, G. Voet, A.J. Wallcraft, and L. Zamudio (2017a), Frequency content of sea surface height variability from internal gravity waves to mesoscale eddies. Journal of Geophysical Research Oceans 122, 2519-2538, doi:10.1002/2016JC012331.

Savage, A.C., B.K. Arbic, M.H. Alford, J.K. Ansong, J.T. Farrar, D. Menemenlis, A.K. O'Rourke, J.G. Richman, J.F. Shriver, G. Voet, A.J. Wallcraft, and L. Zamudio (2017b), Spectral decomposition of internal gravity wave sea surface height in global models. Journal of Geophysical Research Oceans 122, 7803-7821, doi:10.1002/2017JC013009.

Schiller, A., and R. Fiedler (2007), Explicit tidal forcing in an ocean general circulation model. Geophysical Research Letters 34, L03611, doi:10.1029/2006GL028363.

Schmitz, W.J., Jr. (1988), Exploration of the eddy field in the midlatitude North Pacific. Journal of Physical Oceanography 18, 459–468, doi:10.1175/1520-0485(1988)018<0459:EOTEFI>2.0.CO.

Schrama, E.J.O., and R.D. Ray (1994), A preliminary tidal analysis of TOPEX/POSEIDON altimetry. Journal of Geophysical Research 99(C12), 24799–24808, doi:10.1029/94JC01432.

Schwiderski, E.W. (1980), On charting global ocean tides. Reviews of Geophysics and Space Physics 18, 243-268, doi:10.1029/RG018i001p00243.

Scott, R.B., and B.K. Arbic (2007), Spectral energy fluxes in geostrophic turbulence: Implications for ocean energetics. Journal of Physical Oceanography 37, 673-688, doi:10.1175/JPO3027.1.

Scott, R.B., B.K. Arbic, C.L. Holland, A. Sen, and B. Qiu (2008), Zonal versus meridional velocity variance in satellite observations and realistic and idealized ocean circulation models. Ocean Modelling 23, 102–112, doi:10.1016/j.ocemod.2008.04.009.

Scott, R.B., B.K. Arbic, E.P. Chassignet, A.C. Coward, M. Maltrud, W.J. Merryfield, A. Srinivisan, and A. Varghese (2010), Total kinetic energy in four global eddying ocean circulation models and over 5000 current meter records. Ocean Modelling 32, 157-169, doi:10.1016/j.ocemod.2010.01.005.

Scott, R.B., J.A. Goff, A.C. Naveira-Garabato, and A.J.G. Nurser (2011), Global rate and spectral characteristics of internal gravity wave generation by geostrophic flow. Journal of Geophysical Research 116, C09029, doi:10.1029/2011JC007005.

Scott, R.B., and F. Wang (2005), Direct evidence of an oceanic inverse kinetic energy cascade from satellite altimetry. Journal of Physical Oceanography 35, 1650–1666, doi:10.1175/JPO2771.1.

Sheng, J., and Y. Hayashi (1990a), Observed and simulated energy cycles in the frequency domain. Journal of the Atmospheric Sciences 47, 1243–1254, doi:10.1175/1520-0469(1990)047<1243:OASECI>2.0.CO.

Sheng, J., and Y. Hayashi (1990b), Estimation of atmospheric energetics in the frequency domain during the FGGE year. Journal of the Atmospheric Sciences 47, 1255–1268, doi:10.1175/1520-0469(1990)047<1255:EOAEIT>2.0.CO.

Shriver, J.F., B.K. Arbic, J.G. Richman, R.D. Ray, E.J. Metzger, A.J. Wallcraft, and P.G. Timko (2012), An evaluation of the barotropic and internal tides in a high resolution global ocean circulation model. Journal of Geophysical Research 117, C10024, doi:10.1029/2012JC008170.

Shriver, J.F., J.G. Richman, and B.K. Arbic (2014), How stationary are the internal tides in a high resolution global ocean circulation model? Journal of Geophysical Research Oceans 119, 2769-2787, doi:10.1002/2013JC009423.

Shum, C. K., P.L. Woodworth, O.B. Andersen, G.D. Egbert, O. Francis, C. King, S.M. Klosko, C. Le Provost, X. Li, J.-M. Molines, M.E. Parke, R.D. Ray, M.G. Schlax, D. Stammer, C.C. Tierney, P. Vincent, and C.I. Wunsch (1997), Accuracy assessment of recent ocean tide models. Journal of Geophysical Research 102, 25173–25194, doi:10.1029/97JC00445.

Silverthorne, K.E., and J.M. Toole (2009), Seasonal kinetic energy variability of near-inertial motions. Journal of Physical Oceanography 39, 1035–1049, doi:10.1175/2008JPO3920.1.

Simmons, H.L., and M.H. Alford (2012), Simulating the long-range swell of internal waves generated by ocean storms. Oceanography 25, 30–41, doi:10.5670/oceanog.2012.39.

Simmons, H.L., S.R. Jayne, L.C. St. Laurent, and A.J. Weaver (2004a), Tidally driven mixing in a numerical model of the ocean general circulation. Ocean Modelling 6, 245-263, doi:10.1016/S1463-5003(03)00011-8.

Simmons, H.L., R.W. Hallberg, and B.K. Arbic (2004b), Internal wave generation in a global baroclinic tide model. Deep-Sea Research II 51, 3043-3068, doi:10.1016/j.dsr2.2004.09.015.

Skiba, A.W., L. Zeng, B.K. Arbic, M. Müller, and W.J. Godwin (2013), On the resonance and shelf/open-ocean coupling of the global diurnal tides. Journal of Physical Oceanography 43, 1301-1324, doi:10.1175/JPO-D-12-054.1.

Smith, R.D., M.E. Maltrud, F.O. Bryan, and M.W. Hecht (2000), Numerical simulation of the North Atlantic Ocean at 1/10°. Journal of Physical Oceanography 30, 1532-1561, doi:10.1175/1520-0485(2000)030<1532:NSOTNA>2.0.CO.

Smith, W.H.F., and D.T. Sandwell (1997), Global seafloor topography from satellite altimetry and ship depth soundings. Science 277, 1956-1962, doi:10.1126/science.277.5334.1956.

St. Laurent, L.C., and C. Garrett (2002), The role of internal tides in mixing the deep ocean. Journal of Physical Oceanography 32, 2882-2899, doi:10.1175/1520-0485(2002)032<2882:TROITI>2.0.CO.

St. Laurent, L.C., and H. Simmons (2006), Estimates of power consumed by mixing in the ocean interior. Journal of Climate 19, 4877-4890, doi:10.1175/JCLI3887.1.

St. Laurent, L.C, A.C. Naveira Garabato, J.R. Ledwell, A.M. Thurnherr, J.M. Toole, and A.J. Watson (2012), Turbulence and diapycnal mixing in Drake Passage. Journal of Physical Oceanography 42, 2143-2152, doi:10.1175/JPO-D-12-027.1.

Stammer, D., C. Wunsch, and R. Ponte (2000), De-aliasing of global high-frequency barotropic motions in altimeter observations. Geophysical Research Letters 27, 1175-1178, doi:10.1029/1999GL011263.

Stammer, D., R.D. Ray, O.B. Andersen, B.K. Arbic, W. Bosch, L. Carrère, Y. Cheng, D.S. Chinn, B.D. Dushaw, G.D. Egbert, S.Y. Erofeeva, H.S. Fok, J.A.M. Green, S. Griffiths, M.A. King, V. Lapin, F.G. Lemoine, S.B. Luthcke, F. Lyard, J. Morison, M. Müller, L. Padman, J.G. Richman, J.F. Shriver, C.K. Shum, E. Taguchi, and Y. Yi (2014), Accuracy assessment of global barotropic ocean tide models. Reviews of Geophysics 52, 243-282, doi:10.1002/2014RG000450.

Stepanov, V.N., and C.W. Hughes (2004), Parameterization of ocean self-attraction and loading in numerical models of the ocean circulation. Journal of Geophysical Research 109, C07004, doi:10.1029/2003JC002034.

Stewart, K.D., P. Spence, S. Waterman, J. Le Sommer, J.-M. Molines, and J.M. Lilly (2015), Anisotropy of eddy variability in the global ocean. Ocean Modelling 95, 53-65, doi:10.1016/j.ocemod.2015.09.005.

Sugiyama, Y., Y. Niwa, and T. Hibiya (2009), Numerically reproduced internal wave spectra in the deep ocean. Journal of Geophysical Research 36, L07601, doi:10.1029/2008GL036825.

Sun, S., R. Bleck, C. Rooth, J. Dukowicz, E. Chassignet, and P. Killworth (1999), Inclusion of thermobaricity in isopycnic-coordinate ocean models. Journal of Physical Oceanography 29, 2719–2729, doi:10.1175/1520-0485(1999)029<2719:IOTIIC>2.0.CO.

Taguchi, E., W. Zahel, and D. Stammer (2014), Inferring deep ocean tidal energy dissipation from the global high-resolution data-assimilative HAMTIDE model. Journal of Geophysical Research Oceans 119, 4573-4592, doi:10.1002/2013JC009766.

Taylor, G.I. (1919), Tidal friction in the Irish Sea. Philosophical Transactions of the Royal Society of London A220, 1-93, doi:10.1098/rspa.1919.0059.

Thomas, M., J. Sündermann, and E. Maier-Raimer (2001), Consideration of ocean tides in an OGCM and impacts on subseasonal to decadal polar motion excitation. Geophysical Research Letters, 28, 2457-2460, doi:10.1029/2000GL012234.

Thoppil, P.G., J.G. Richman, and P.J. Hogan (2011), Energetics of a global ocean circulation model compared to observations. Geophysical Research Letters, 38, L15607, doi:10.1029/2011GL048347.

Tierney, C., J. Wahr, F. Bryan, and V. Zlotnicki (2000a), Short-period oceanic circulation: Implications for satellite altimetry. Geophysical Research Letters 27, 1255-1258, doi:10.1029/1999GL010507.

Tierney, C.G., L.H. Kantha, and G.H. Born (2000b), Shallow and deep water global ocean tides from altimetry and numerical modeling. Journal of Geophysical Research 105, 11259-11277, doi:10.1029/1999JC900314.

Timko, P.G., B.K. Arbic, J.G. Richman, R.B. Scott, E.J. Metzger, and A.J. Wallcraft (2012), Skill tests of tidal currents in a three-dimensional ocean model: A look at the North Atlantic. Journal of Geophysical Research 117, C08014, doi:10.1029/2011JC007617.

Timko, P.G., B.K. Arbic, J.G. Richman, R.B. Scott, E.J. Metzger, and A.J. Wallcraft (2013), Skill testing a three-dimensional global tide model to historical current meter records. Journal of Geophysical Research Oceans 118, 6914-6933, doi:10.1002/2013JC009071.

Timko, P.G., B.K. Arbic, J.A. Goff, J.K. Ansong, W.H.F. Smith, A. Melet, and A.J. Wallcraft (2017), Impact of synthetic abyssal hill roughness on resolved motions in numerical global ocean tide models. Ocean Modelling 112, 1-16, doi:10.1016.j.ocemod.2017.02.005.

Trossman, D.S., B.K. Arbic, S.T. Garner, J.A. Goff, S.R. Jayne, E.J. Metzger, and A.J. Wallcraft (2013), Impact of parameterized lee wave drag on the energy budget of an eddying global ocean model. Ocean Modelling 72, 119-142, doi:10.1016/j.ocemod.2013.08.006.

Trossman, D.S., B.K. Arbic, J.G. Richman, S.T. Garner, S.R. Jayne, and A.J. Wallcraft (2016), Impact of topographic internal lee wave drag on an eddying global ocean model. Ocean Modelling 97, 109-128, doi:10.1016/j.ocemod.2015.10.013.

Vinogradova, N.T., R.M. Ponte, K.J. Quinn, M.E. Tamisiea, J.-M. Campin, and J.L. Davis (2015), Dynamic adjustment of the ocean circulation to self-attraction and loading effects. Journal of Physical Oceanography 45, 678-689, doi:10.1175/JPO-D-14-0150.1.

Wahr, J.M., and T. Sasao (1981), A diurnal resonance in the ocean tide and in the Earth's load response due to the resonant free "core nutation." Geophysical Journal of the Royal Astronomical Society 64, 747-765, doi:10.1111/j.1365-246X.1981.tb02693.x.

Wang, J., L.-L. Fu, B. Qiu, D. Menemenlis, J.T. Farrar, Y. Chao, A.F. Thompson, and M.M. Flexas (2018), An observing system simulation experiment for the calibration and validation of the surface water ocean topography sea surface height measurement using in situ platforms. Journal of Atmospheric and Oceanic Technology 35, 281-297, doi:10.1175/JTECH-D-717-0076.1.

Waterhouse, A.F., J.A. MacKinnon, J.D. Nash, M.A. Alford, E. Kunze, H.L. Simmons, K.L. Polzin, L.C. St. Laurent, O.M. Sun, R. Pinkel, L.D. Talley, C.B. Whalen, T.N. Huussen, G.S. Carter, I. Fer, S. Waterman, A. Naveira Garabato, T.B. Sanford, and C.M. Lee (2014), Global patterns of diapycnal mixing from measurements of the turbulent dissipation rate. Journal of Physical Oceanography 44, 1854–1872, doi:10.1175/ JPO-D-13-0104.1.

Weis, P., M. Thomas, and J. Sündermann (2008), Broad frequency tidal dynamics simulated by a high-resolution global ocean tide model forced by ephemerides. Journal of Geophysical Research 113, C10029, doi:10.1029/2007JC004556.

Wessel, P., and M.T. Chandler (2011), The spatial and temporal distribution of marine geophysical surveys. Acta Geophysica 59, 55-71, doi:10.2478/s-11600-010-0038-1.

Whalen, C.B., J.A. MacKinnon, L.D. Talley, and A.F. Waterhouse (2015), Estimating the mean diapycnal mixing using a finescale strain parameterization. Journal of Physical Oceanography 45, 1174-1188, doi:10.1175/JPO-D-14-0167.1.

Whalen, C.B., L.D. Talley, and J.A. MacKinnon (2012), Spatial and temporal variability of global ocean mixing inferred from Argo profiles. Geophysical Research Letters 39, L18612, doi:10.1029/2012GL053196.

Williams, J.G., and D.H. Boggs (2016), Secular tidal changes in lunar orbit and Earth rotation. Celestial Mechanics and Dynamical Astronomy 126, 89-129, doi:10.1007/s10569-016-9702-3.

Wright, C.J., R.B. Scott, P. Ailliot, and D. Furnival (2014), Lee wave generation rates in the deep ocean. Geophysical Research Letters 41, 2434-2440, doi:10.1002/2013GL059087.

Wunsch, C. (1972), Bermuda sea level in relation to tides, weather, and baroclinic fluctuations. Reviews of Geophysics 10, 1–49, doi:10.1029/RG010i001p00001.

Wunsch, C. (1975), Internal tides in the ocean. Reviews of Geophysics and Space Physics 13, 167-182, doi:10.1029/RG013i001p00167.

Wunsch, C., and D. Stammer (1997), Atmospheric loading and the oceanic "inverted barometer" effect. Reviews of Geophysics 35, 79-107, doi:10.1029/96RG03037.

Xu, Y., and L.-L. Fu (2012), The effects of altimeter instrument noise on the estimation of the wavenumber spectrum of sea surface height. Journal of Physical Oceanography 42, 2229-2233, doi:10.1175/JPO-D-12-0106.1.

Zahel, W., and M. Müller (2005), The computation of the free barotropic oscillations of a global ocean model including friction and loading effects. Ocean Dynamics 55, 137–161, doi:10.1007/s10236-005-0029-y.

Zaron, E.D. (2017), Mapping the non-stationary internal tide with satellite altimetry. Journal of Geophysical Research Oceans 122, 539–554, doi:10.1002/ 2016JC012487.

Zhao, Z., M.H. Alford, J.A. MacKinnon, and R. Pinkel (2010), Long-range propagation of the semi-diurnal internal tide from the Hawaiian ridge. Journal of Physical Oceanography 40, 713–736, doi:10.1175/2009JPO4207.1.